Light Ion Beam Fusion Target Development Facility Studies: Progress Report for the Period October 1, 1985 to October 31, 1986

B. Badger, H. Attaya, T.J. Bartel, D. Bruggink, R.L. Engelstad, D.L. Henderson, E.G. Lovell, G.A. Moses, R.R. Peterson, M.E. Sawan, J.J. Watrous

October 1986

UWFDM-713

FUSION TECHNOLOGY INSTITUTE

UNIVERSITY OF WISCONSIN

MADISON WISCONSIN

Light Ion Beam Fusion Target Development Facility Studies: Progress Report for the Period October 1, 1985 to October 31, 1986

B. Badger, H. Attaya, T.J. Bartel, D. Bruggink, R.L. Engelstad, D.L. Henderson, E.G. Lovell, G.A. Moses, R.R. Peterson, M.E. Sawan, J.J. Watrous

Fusion Technology Institute
University of Wisconsin
1500 Engineering Drive
Madison, WI 53706

http://fti.neep.wisc.edu

October 1986

UWFDM-713

LIGHT ION BEAM FUSION TARGET DEVELOPMENT FACILITY STUDIES: PROGRESS REPORT FOR THE PERIOD OCTOBER 1, 1985 TO OCTOBER 31, 1986

B. Badger, H. Attaya, T.J. Bartel, R.L. Engelstad,

D.L. Henderson, E.G. Lovell, G.A. Moses,

R.R. Peterson, M.E. Sawan, J.J. Watrous

Fusion Technology Institute
1500 Johnson Drive
University of Wisconsin-Madison
Madison, Wisconsin 53706

October 1986

UWFDM-713

TABLE OF CONTENTS

1. INTRODUCTION

1.1 Statement of Work and Summary of Results

During the period from October 1985 to October 1986 we have addressed three general technical areas associated with the design of the Light Ion Fusion Target Development Facility (TDF). These are: (1) mechanical analysis of the target chamber, (2) activation analysis of the target chamber and diodes, and (3) plasma channel formation and ion propagation. The specific statement of work is given in Table 1.1. The remainder of Chapter 1 is a summary of our results.

Chapter 2 contains a description of the activation analysis done for the ion diode and its surrounding structure. Two-dimensional discrete ordinate neutron transport calculations were done to determine the neutron flux for four different ion diode and plasma channel penetration options. Both a 1 cm and 10 cm radius penetration through the graphite neutron moderator were considered along with either a stainless steel or aluminum diode. Activation and dose calculations were performed to determine the dose received near the diode following the last shot. This temporal behavior is computed using a sequence of neutron pulses rather than a steady state source to more accurately model the TDF operation. The contribution to the dose level from different parts of the structure was determined to allow the definition of procedures for maintenance. These calculations represent our first attempt to model such a complex geometric configuration. Work will continue on improving the modeling.

Chapter 3 contains a description of current mechanical analysis and design of the reaction chamber. For the base case, a 3 m radius cylindrical vessel, preliminary recommendations are made for the heat shield and neutron moderator. The effects of the neutron moderator on modeling the response of

Table 1.1 Statement of Work

1. Neutron Transport and Activation Calculations

   a. Perform multidimensional Monte Carlo neutronics calculations for the TDF conceptual design. Details (as far as they are known) of the target chamber, ion diodes, target injector, and diagnostics equipment should be included in the calculations.
   b. Calculate activation and biological dose rates based upon the Monte Carlo neutronics calculations of item 1a. Activation of the ion diodes should be addressed in some detail. A multidimensional gamma transport calculation should be used in determining the dose rate.

2. TDF Target Chamber Design

   Design of a TDF target chamber with the activation reducing structures dictated by the work performed in items 1a and 1b. This design may include a thick graphite region that is either a woven fabric, a felt, or in some other form. This region must be able to withstand the thermal and shock loading of the target explosions.

3. TDF Plasma Channels

   Utilize the WINDOW, ZPINCH, and ION computer codes in a study of the constraints on transportable ion power in the TDF plasma channels.

   a. The WINDOW code should be modified to model the constraints on the propagation of 25 to 35 MV Li^{+3} beam ions in nonhydrogenic plasmas (e.g., N_2, NH_3, etc.). A detailed explanation of the physics included in this modification should be provided.

   b. The ZPINCH code should be used in an optimization study of TDF plasma channels. The dependencies of minimum channel radius, channel current profile, and maximum plasma current on the choice of background gas, laser profile, and electrode voltage should be emphasized.

   c. The effects of the angular momentum of the beam ions on their trajectories should be included in the ION code. Graphical descriptions of beam ion trajectories in plasma channels consistent with those modeled in tasks 3a and 3b should be provided.

4. Initiate the design of a disposable TDF target chamber of spherical shape and small radius (~ 1 m). This chamber would contain the target blast and activated debris and would be replaced frequently (after every 50 to 200 shots).

   a. Evaluate the overpressure and heat flux on the spherical vessel from the target x-rays and fireball.

Table 1.1 (continued)

b. Evaluate the thermal and mechanical response of the spherical shell to the blast and estimate its survivability.

c. Compute the activation of the chamber from target debris and target neutrons.

d. Estimate the cost of the spherical chamber.

the structural wall are discussed and corresponding results presented. Compact spherical chambers are also described, including stress histories determined directly from numeric pressure data. This procedure was necessitated by a change in the pressure pulse to a somewhat more complex form, a consequence of the size reduction. Results indicate that the compact spherical chamber is a legitimate possibility from a mechanical design perspective.

Chapter 4 is a discussion of TDF plasma channel modeling. The ZPINCH code was further developed to allow the solution of the external circuit equation along with the plasma MHD equations. This allows the user to define the external circuit parameters while the code then computes the voltage and current from this circuit as a function of time. The ZPINCH code was then used to investigate the creation of optimum plasma channels in nitrogen gas.

The ION code was further modified to include angular momentum in the ion beam. This will allow the propagation of hollow beams.

The WINDOW code was modified to include radiative cooling effects. Since the plasma channel temperature plays an important role in the instability threshold criteria, radiative cooling must be included to obtain a better estimate of the ion power limitations in high Z plasma channels such as nitrogen.

Chapter 5 is a description of the two TDF chamber designs currently under investigation. The first is a 6 meter diameter chamber with a 0.5 meter graphite moderator zone within it to reduce the activation of the aluminum vessel. The design goal is to allow hands-on maintenance at the outside of the first wall at one week after the last shot. The second design is a 2 meter diameter chamber with no graphite moderator region. The design goal for this chamber is to allow easy replacement of the chamber at frequent

intervals. Mechanical analysis indicates that this smaller chamber is feasible, because the maximum overpressure comes in an impulse form that has a much smaller effect on the wall than a steady state loading of the same magnitude.

1.2 Publications

Publications are one way of measuring the productivity of research projects such as this one. Table 1.2 is a list of publications supported by this research project. Three reviewed papers were published and 3 reviewed talks were given at technical meetings. One unreviewed talk was given at the APS Plasma Physics Meeting and 10 Fusion Technology Institute reports were prepared.

1.3 Graduating Students

John Watrous, supported in part by this contract, graduated during the past year. He is currently employed at the Naval Research Laboratory. In addition, Lichung Pong, a graduate from the previous contract period, accepted employment with Technadyne and works under contract for Sandia-Albuquerque in the area of fission reactor containment modeling for severe accident scenarios.

Table 1.2. Publications

Reviewed Papers

1. D.L. Henderson, G.A. Moses and R.R. Peterson, "Activation Studies of the Light Ion Fusion Target Development Facility," J. Nucl. Mat. 00, 0 (1986).

2. J.J. Watrous and R.E. Olson, "Ion Beam Trapping in Plasma Channels for Light Ion Inertial Confinement Fusion," Fusion Tech. 0, 0 (1986).

3. T.J. Bartel, R.R. Peterson and G.A. Moses, "Numerical Simulation of a Stratified Gas Cavity," Fusion Tech. 0, 0 (1986).

Reviewed Talks

1. D.L. Henderson, G.A. Moses and R.R. Peterson, "Activation Studies of the Light Ion Fusion Target Development Facility," 5th Int'l. Meeting on Fusion Materials, Chicago, IL, April 1986.

2. G.A. Moses, R.R. Peterson, R.L. Engelstad, D.L. Henderson, G.L. Kulcinski, E.G. Lovell, I.N. Sviatoslavsky, J.J. Watrous, R.E. Olson and D.L. Cook, "Preconceptual Design of the Light Ion Beam Fusion Target Development Facility," Proceedings of the 11th Symposium on Fusion Engineering, Austin, TX, November 1985.

3. R.L. Engelstad and E.G. Lovell, "Lifetime Analysis of the TDF Reaction Chamber," Proceedings of the 11th Symposium on Fusion Engineering, Austin, TX, November 1985.

Fusion Technology Institute Reports

1. D.L. Henderson, G.A. Moses and R.R. Peterson, "One-Dimensional Activation and Radiological Dose Calculations for the Light Ion Fusion Target Development Facility," University of Wisconsin Fusion Technology Institute Report UWFDM-636, October 1985.

2. G.A. Moses, R.R. Peterson, R.L. Engelstad, D.L. Henderson, G.L. Kulcinski, E.G. Lovell, I.N. Sviatoslavsky, J.J. Watrous, R.E. Olson and D.L. Cook, "Preconceptual Design of the Light Ion Beam Fusion Target Development Facility," University of Wisconsin Fusion Technology Institute Report UWFDM-664, November 1985.

3. R.L. Engelstad and E.G. Lovell, "Lifetime Analysis of the TDF Reaction Chamber," University of Wisconsin Fusion Technology Institute Report UWFDM-665, November 1985.

4. R.R. Peterson, G.A. Moses, J.J. Watrous, R.E. Olson, "Plasma Channels for Light Ion Beam Propagation in the Target Development Facility," University of Wisconsin Fusion Technology Institute Report UWFDM-666, November 1985.

5. R.R. Peterson, "CONRAD - A Coupled Radiation Hydrodynamics-Condensation Computer Code," University of Wisconsin Fusion Technology Institute Report UWFDM-670, January 1986.

6. D.L. Henderson, "DKR-1100: A UNIVAC 1100 Version of the DKR Radioactivity Code," University of Wisconsin Fusion Technology Institute Report UWFDM-671, February 1986.

7. D.L. Henderson, "DKRDOSE and DKRCONVERT: A Dose Rate Code and an Auxiliary Data Handling Code for the DKR and DKR-1100 Radioactivity Codes," University of Wisconsin Fusion Technology Institute Report UWFDM-672, February 1986.

8. T.J. Bartel, G.A. Moses and R.R. Peterson, "Microfireballs in Stratified Target Chamber Gases in the Light Ion Target Development Facility - Final Report for the Period September 9, 1983 to September 30, 1985," University of Wisconsin Fusion Technology Institute Report UWFDM-677, September 1985.

9. T.J. Bartel, R.R. Peterson and G.A. Moses, "Numerical Simulation of a Stratified Gas ICF Cavity," University of Wisconsin Fusion Technology Institute Report UWFDM-679, April 1986.

10. G.A. Moses, "ION - A Code to Compute Ion Trajectories in Z-Pinch Plasma Channels, University of Wisconsin Fusion Technology Institute Report UWFDM-712, June 1986.

2. RADIOLOGICAL DOSE CALCULATIONS

2.1 Introduction

Biological dose rate calculations have been performed for a point external to the diode vacuum casing of the Target Development Facility for times following an operational period of 1 month. A new computational model has been developed for the radioactivity calculations to account for the sequential pulsed operation mode of the facility. The primary diode material considered is SS 304LN with an alternative material being aluminum 6061-T6. For the new pulse sequence model, it is shown that for both the aluminum and stainless steel diodes the dose rates external to the diode vacuum casing are above 1 rem/hr after a 1 day shutdown period. After a 1 week shutdown period, the dose rates have dropped to 90 and 12 mrem/hr, respectively.

Previous steady state radioactivity and dose rate calculations for the bare Al-6061-T6 Target Development Facility chamber wall and for the Au or W target debris accumulating onto the inner surface of the chamber wall have shown that the biological doses at the inner and outer surfaces of the wall are still quite significant, being 1.29 rem/hr at 1 week after shutdown, even with periodic removal of the target debris.[1] An examination of the nuclear decay products which lead to this high dose level shows that the decay products are mainly the result of neutron transmutation reactions above threshold energies in the range of 2-12 MeV. This in turn led to the placement of a 1 m thick, 40% porosity graphite moderating structure within the target chamber for the purpose of reducing the large component of high energy neutrons to below the neutron reaction threshold values prior to their interaction with the chamber.[2] This is shown in Fig. 2.1. The dose rate at the aluminum

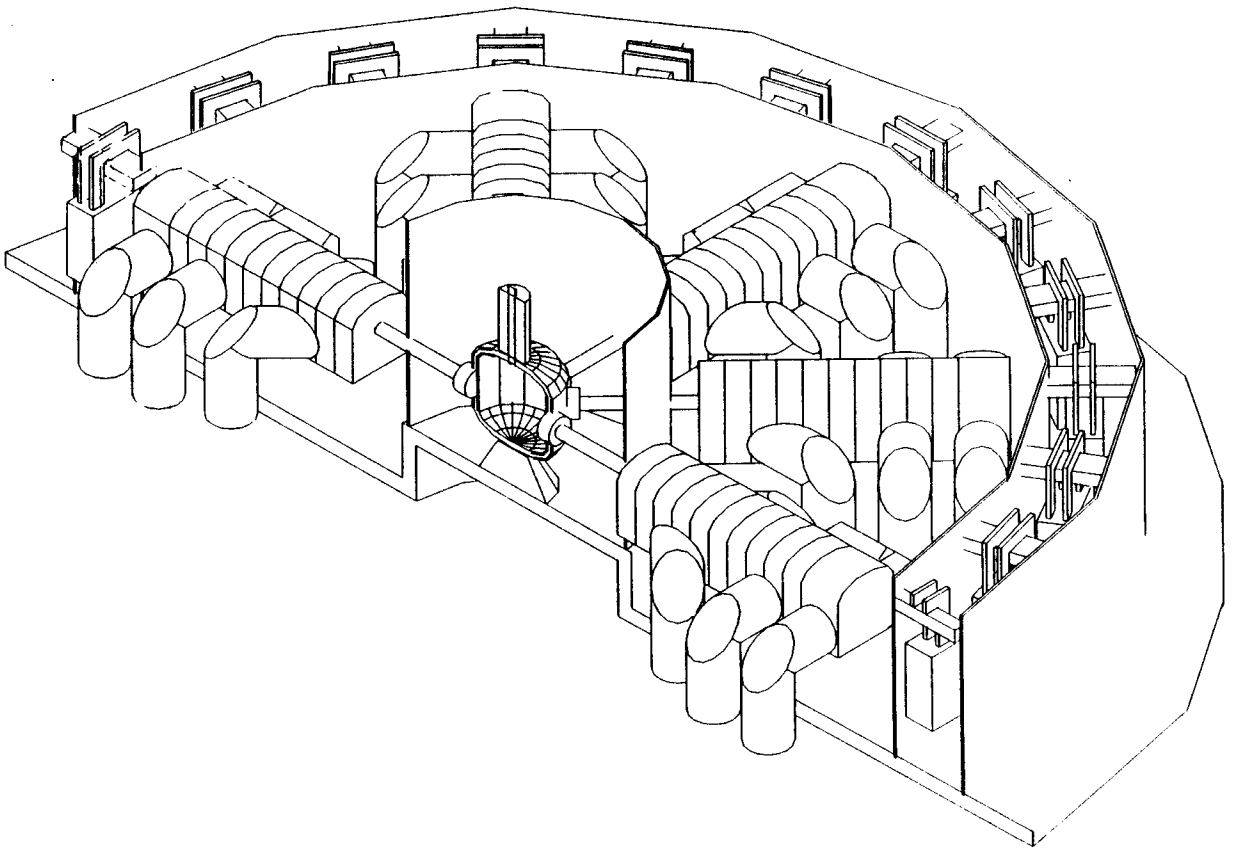

Fig. 2.1. Preliminary design of the Light Ion Fusion Target Development Facility.

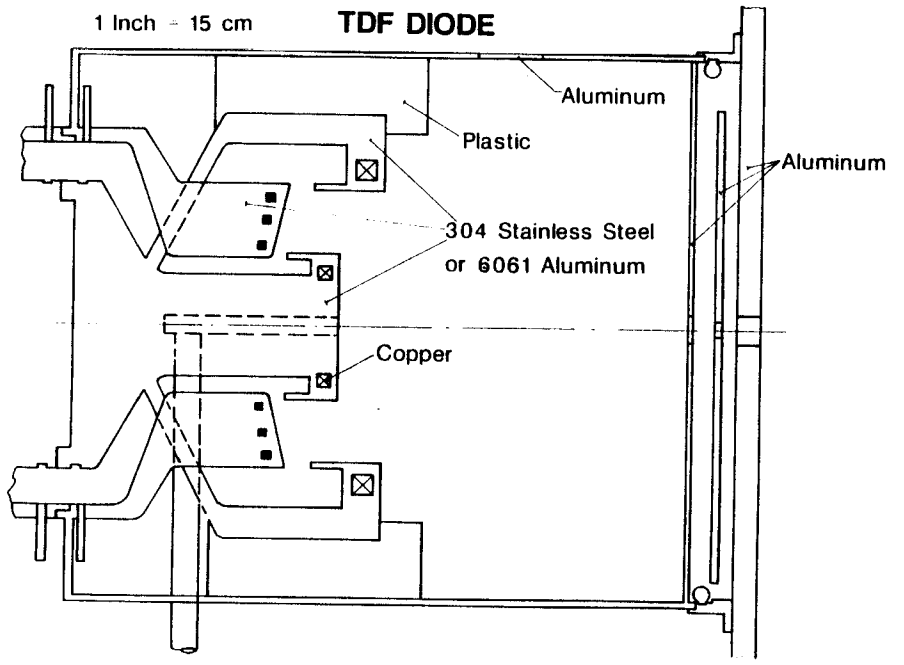

Fig. 2.2. Schematic of the high voltage ion diode used for the neutronic and dose rate calculations.

6061-T6 target chamber outer surface was thus reduced from 1.29 rem/hr to 13.1 mrem/hr after a 1 week shutdown period.

One of the critical areas of the facility is the design of the high voltage diodes which convert the electrical pulse into ion beams. Depending on the repetition rate and lifetime of the diodes, the time allowable for maintenance and/or for exchange of the diode may be limited by the biological dose rate in the immediate vicinity of the ion diodes. Because of this need to know the dose rate, radioactivity and biological dose rate calculations have been performed for a point near the surface of the diode casing for the ion diode depicted in Fig. 2.2. Two ion diode materials are considered, the standard material being stainless steel 304LN and the alternative material being aluminum 6061-T6. Penetrations through the graphite moderator of 1 cm and 10 cm for plasma channels have also been considered. Dose rates computed using a more realistic pulse sequence scheme to account for the actual pulsed operation of the facility are compared to the standard steady state assumption. These calculations represent an estimate of the biological dose near the vicinity of the ion diode. Details of this study can be found in Ref. 3.

2.2 Neutron Transport Calculations

The D-T fuel in ICF facilities is heated and compressed to extremely high densities ($\sim 10^{25}/cm^3$) before it ignites. A consistent neutronics analysis must, therefore, account for neutron target interactions which result in considerable spectrum softening of the fusion neutrons. The target DT load was assumed to be 1 mg and the fuel was assumed to be compressed to a density times radius product (ρR value) of 2 g/cm^2. The compressed target configuration used in the neutron transport calculations is shown in Fig. 2.3. A

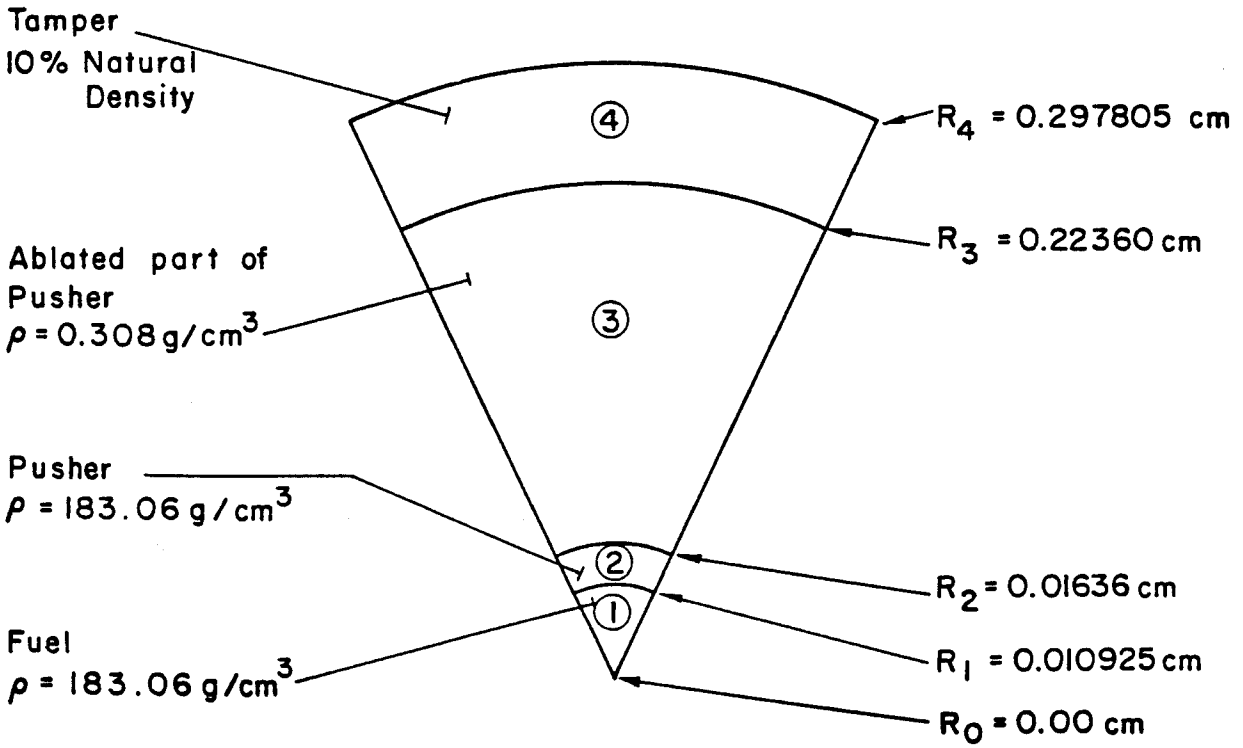

Fig. 2.3. The compressed target configuration used in the target neutronics calculations.

tamper density that is 10% of the natural density was used to account for the effect of heating by the impinging ion beams.

The spectrum of neutrons escaping from the target is given in Fig. 2.4. The results indicate that for each D-T fusion, 1.046 neutrons leak from the target mainly due to (n,2n) reactions in the dense D-T fuel. A fuel burnup fraction of 30% was assumed giving approximately 100 MJ of fusion energy released from the 1 mg fuel target used in the calculations. Since the TDF target is required to produce a yield of 200 MJ a D-T mass of 2 mg will be needed. For the same ignition ρR value, intrinsic quantities such as neutron spectrum are assumed not to change while absolute quantities such as neutron yield are scaled by a factor of 2. A 200 MJ target D-T yield corresponds to 7.09×10^{19} D-T fusions per shot and 7.42×10^{19} neutrons emanating from the target per shot. The neutron spectrum obtained from the target neutronics calculation was used to represent the source for the chamber neutronics.

The neutron flux in the diode is computed in two steps. First the cylindrically shaped target chamber is approximated by spherical geometry for a one-dimensional calculation. A schematic of the TDF target chamber model used in the one-dimensional calculation is given in Fig. 2.5. The source is considered to be a point isotropic source at the center of the cavity. The calculations were performed using the ONEDANT code with the P_3-S_8 approximation. The calculation uses 20 seconds of Cray-XMP time.

The one-dimensional cavity calculation discussed above is used to obtain the energy and angular distribution of neutrons and gamma photons incident on the graphite liner. These are used to represent a surface source in the second step of the calculation where the detailed geometrical configuration of the diode is modeled. Since the beam ports occupy only 0.5% of the liner

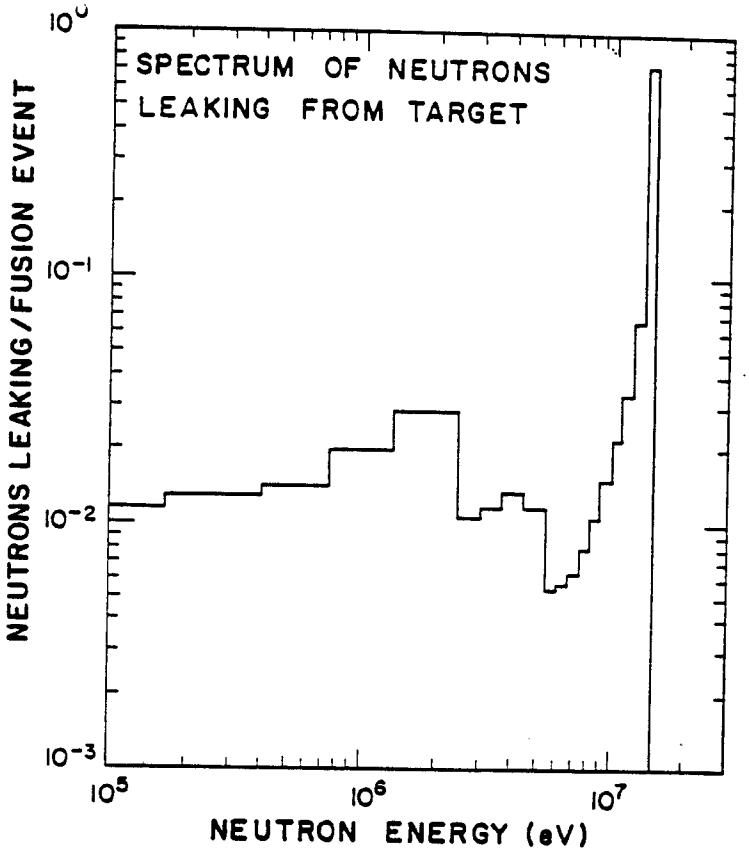

Fig. 2.4. Spectrum of neutrons emerging from the target.

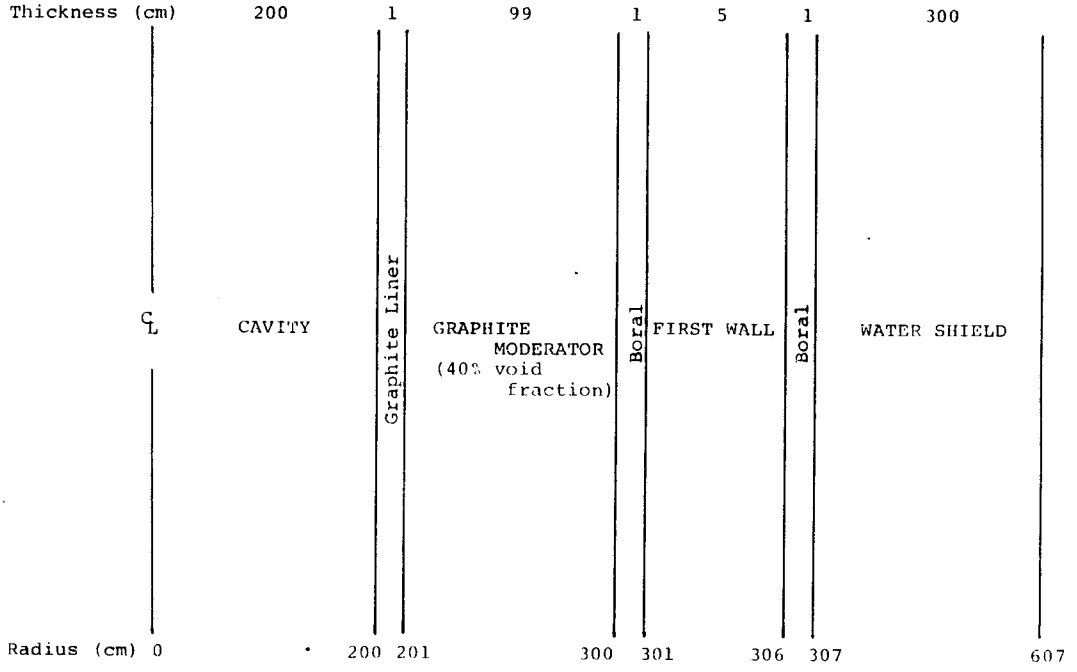

Fig. 2.5. Schematic of the TDF chamber used in the one-dimensional neutronics calculation.

inner surface area, the one-dimensional calculation in which the penetrations are not modeled gives a fairly accurate estimate of the nuclear radiation incident on the surface of the liner and the beam penetration opening. In addition, since the diodes are located in the facility midplane, using spherical geometry in the one-dimensional calculation yields reasonably accurate results for nuclear radiation incident on the area around the beam ports.

The energy spectra of neutrons and gamma photons incident on the inner surface of the graphite liner are shown in Figs. 2.6 and 2.7. For each D-T fusion in the target, 1.046 neutrons emanate from the target and impinge directly on the liner. Neutron scattering collisions in the graphite moderator result in reflecting some of these neutrons back into the cavity. These reflected neutrons will end up impinging on the liner with a fraction of them reflected again into the cavity. Our results indicate that for each D-T fusion, 5.712 neutrons end up reentering the cavity and a total of 6.758 neutrons will be incident on the liner. The neutrons coming directly from the target represent only 15% of the total impinging neutrons which explains the much softer neutron energy spectrum compared to that emerging from the target. Together with the reflection of gamma photons by the material surrounding the cavity, gamma generation in the surrounding material enhances the number of photons reentering the cavity. The gamma photons coming directly from the target represent only 3% of the 0.541 total number of photons incident on the liner per D-T fusion.

The diode geometry was modeled in two-dimensional r-z geometry as shown in Fig. 2.8. Calculations have been performed for two penetration radii of 10 and 1 cm. The option of using aluminum 6061-T6 for the cathode and anode instead of stainless steel 304LN was also considered. Hence, four two-

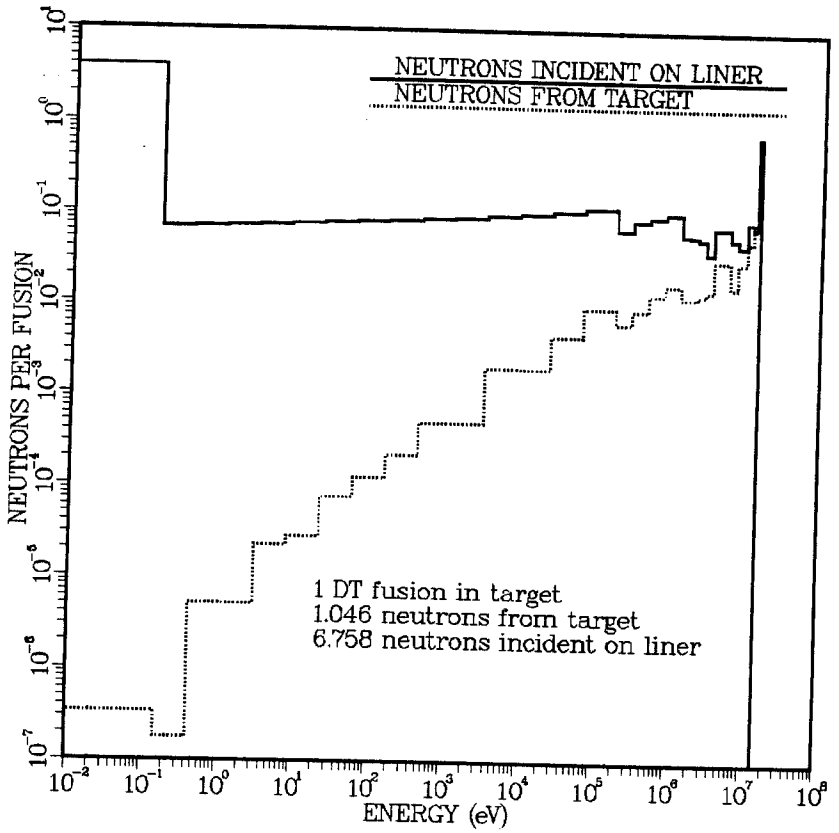

Fig. 2.6. Energy spectrum of neutrons incident on the graphite liner.

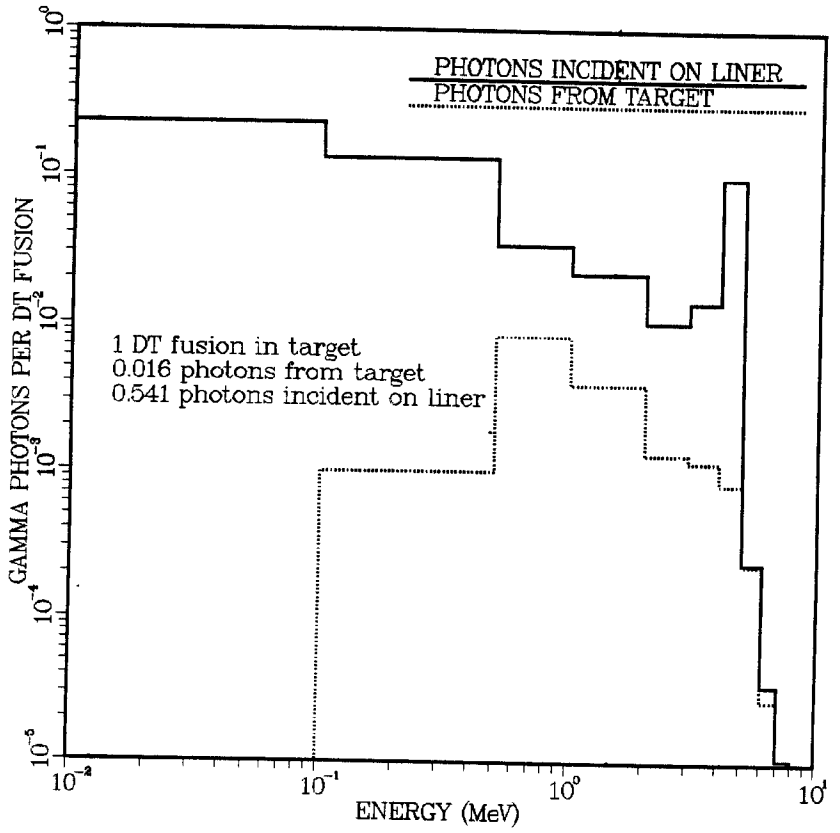

Fig. 2.7. Energy spectrum of gamma photons incident on the graphite liner.

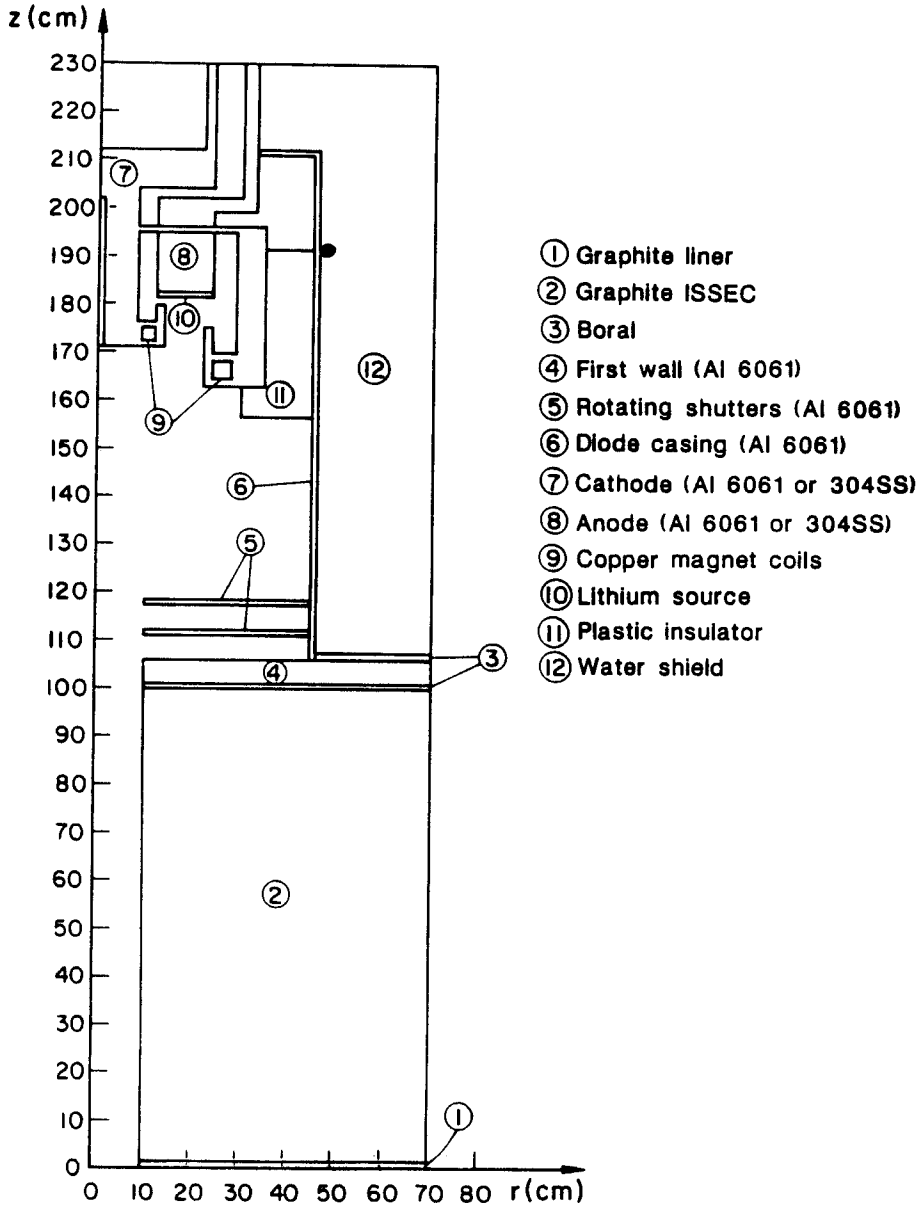

Fig. 2.8. The r-z geometrical model used in the two-dimensional neutronics and activation calculations.

dimensional neutronics calculations have been performed with the different penetration radii and diode materials.

The two-dimensional discrete ordinates code TWODANT was used in the calculations with the same 30 neutron-12 gamma multigroup cross section data based on the ENDF/B-V evaluation which was used in the one-dimensional calculation. A spatially uniform surface source was used at the bottom boundary represented by the energy dependent angular flux at the inner surface of the liner as obtained from the one-dimensional calculation. The source is given in the four discrete ordinates directions going into the graphite moderator. The source is assumed to be uniform in the azimuthal direction. A vacuum boundary condition is used at the bottom boundary since the contribution from neutrons reentering the cavity from the moderator is already taken into account in the surface source. A right reflecting boundary is used at a radius of 70 cm which is roughly half the distance between the centerlines of adjacent diodes. A vacuum boundary is used at the top. 32 radial and 77 axial fine mesh intervals were used leading to flux calculations at 2464 mesh points. Each calculation took 2 min of Cray-XMP CPU time.

In addition to the forward neutron transport calculations, adjoint gamma transport calculations were performed for the four cases considered here. In the adjoint calculations, an adjoint source was used on the outer surface of the diode casing at z = 190 cm with the energy spectrum given by the gamma flux-to-dose conversion factors. These calculations were used to determine the adjoint dose field distribution that is coupled with the decay gamma source to yield the dose at this position for various times after shutdown.

The two-dimensional calculational model used here has several shortcomings that introduce uncertainties in the results. In order to model the

detailed three-dimensional geometry for the deterministic two-dimensional discrete ordinates calculation several adaptations were made to yield the idealized geometrical model shown in Fig. 2.8. The actual planes of symmetry cannot be included in the two-dimensional geometrical model necessitating the use of a cylindrical reflecting boundary to account for the contribution from the surrounding regions. Since the diodes are located on the facility midplane, each diode is surrounded by two diodes on opposite sides. Even though the cylindrical reflecting boundary is located at half the distance between the centerlines of the two adjacent diodes, its use is equivalent to surrounding the modeled diode by diode penetrations at all azimuthal locations. This tends to overestimate the flux and dose in the diode area. Another geometrical problem stems from using a planar disc source at the bottom boundary of the r-z model. The model does not take into account the geometrical attenuation of the flux which can be significant particularly for the component coming directly from the target at the center of the cavity. The $1/R^2$ geometrical attenuation implies a geometrical attenuation factor of ~ 3 for the flux as one goes from the front of the graphite moderator to the front of the diode. It is clear, therefore, that the geometrical approximations introduced by the two-dimensional model tend to overestimate the flux and dose in the diode region. The only way to avoid these geometrical modeling deficiencies is to use the Monte Carlo method where the detailed three-dimensional geometry can be modeled. However, the Monte Carlo method is statistical in nature and is not capable of generating accurate estimates for differential quantities such as the neutron energy spectra in optically thin zones which are required for activation and dose calculations. Several tens of Cray hours might be needed to produce the energy and spatial distribution of the neutron flux to

the same level of detail as obtained from the deterministic two-dimensional discrete ordinates calculational procedure used in this work.

Another shortcoming of the model used here is an inherent problem in the discrete ordinates method referred to as the ray effect. It is related to the fact that the angular flux is given only in certain discrete directions. It is, therefore, not possible to exactly represent the component in the normal direction ($\mu = 1$). We calculate that 15% of the neutrons incident on the penetration opening come directly from the target in the normal direction. However, these neutrons are assumed to be in the direction $\mu = 0.962$ ($\theta = 15.8°$) and will end up impinging on the penetration wall rather than streaming directly to the diode. Since the contribution of the primary neutrons from the target decreases considerably for lower energy neutrons as shown from Fig. 2.6, the underestimation of the flux in the diode is more pronounced for high energy neutrons. Our calculations indicate that for the 14 MeV neutrons an order of magnitude attenuation occurs in the 1 m long penetration while two orders of magnitude attenuation occurs in the graphite moderator. If no attenuation takes place in the penetration, as should be expected in the actual case, we estimated that a factor of ~ 2.5 more 14 MeV neutrons will be entering the diode region. To quantify this effect we performed a calculation for the case of the steel diode and 10 cm radius penetration with the thickness of the moderator reduced to 30 cm and its density increased to preserve the optical thickness. In this calculation neutrons incident on the duct opening in the direction $\mu = 0.962$ are forced to stream into the diode. This tends to overestimate the flux in the diode for low energy neutrons where the contribution coming directly from the target is small. In addition, the streaming neutrons are forced to impinge on the outer part of

the diode leading to higher dose levels outside the diode casing. The results of this calculation will be used to indicate an upper bound for the biological dose level.

The neutron energy spectrum was determined at the 2464 mesh points used in the two-dimensional model and this flux distribution was used as the source for the activation calculations.

Figures 2.9 to 2.12 show the radial distribution of the neutron flux in energy groups 2 (13.5-15.0 MeV), 7 (3.68-6.07 MeV), 20 (1.235-3.35 keV), and 30 (thermal group), respectively for the 10 cm penetration radius and steel diode. The results are normalized to 1 D-T fusion/s and are shown for three axial locations: back of graphite moderator (z = 100 cm), front of diode (z = 170 cm), and back of diode (z = 210 cm). The results given by dashed lines represent the case where neutrons incident on the penetration opening in the direction $\mu = 0.962$ are forced to stream into the diode by using a 30 cm compressed moderator. It is clear that about an order of magnitude higher 14 MeV flux is obtained at the back of the 100 cm long penetration in the 30 cm compressed moderator case. The effect is less pronounced for the lower energy groups. The 14 MeV flux at the front of the diode has a pronounced off-axis peak at $r \simeq 20$ cm which is related to the discrete directions used. The peak is more pronounced for the 30 cm compressed moderator since neutrons in the direction $\mu = 0.962$ stream directly to the diode without being attenuated in the moderator as is the case for the 100 cm thick graphite moderator. This indicates that using the 30 cm compressed moderator will force the 14 MeV neutrons to impinge on the outer parts of the diode resulting in overestimating the dose outside the diode. This effect is less pronounced for energy group 7 due to the smaller contribution from the neutrons coming directly from

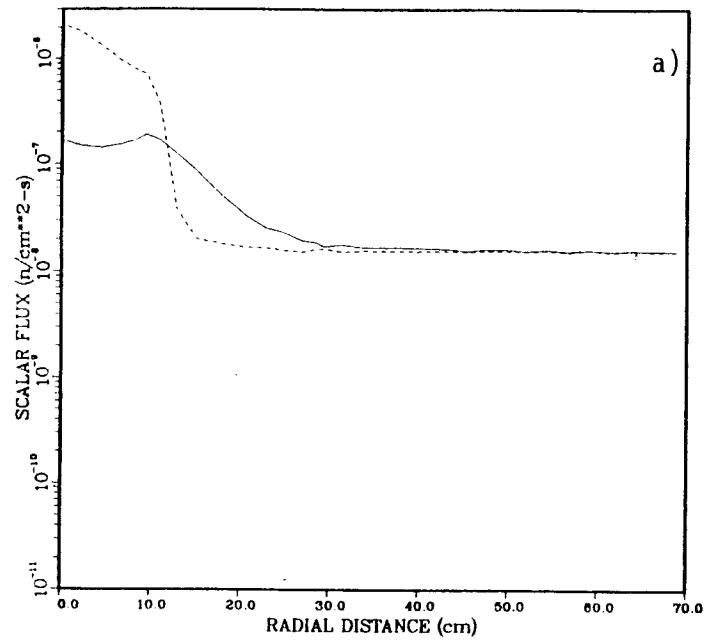

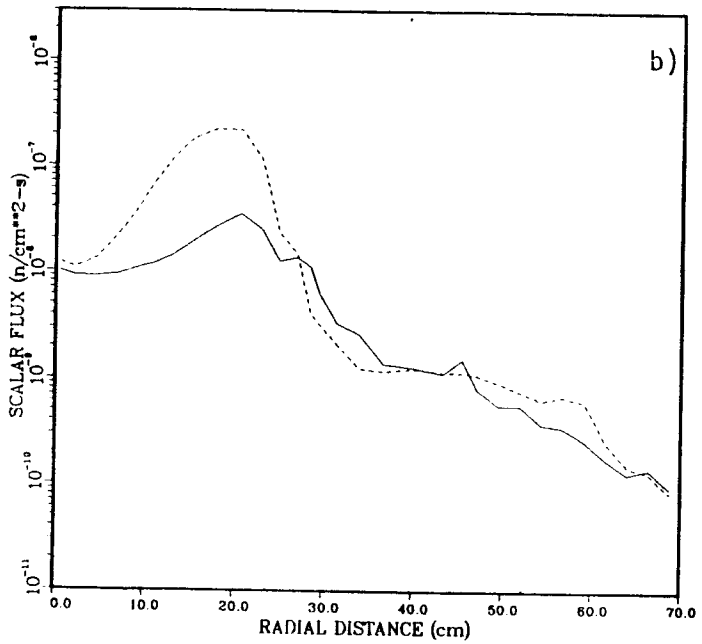

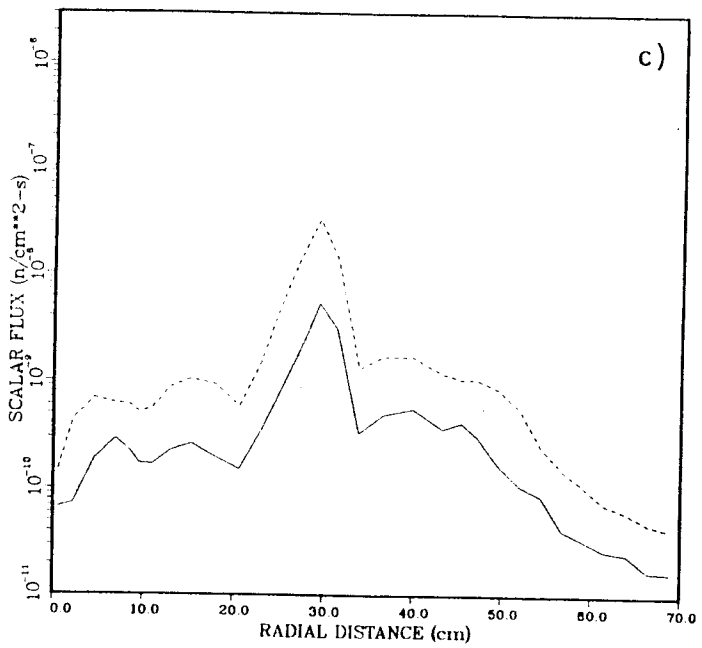

Fig. 2.9. Radial distribution of the neutron flux in group 2 for three axial positions; a) lack of graphite moderator (z = 100 cm), b) front of diode (z = 170 cm) and c) back of diode (z = 210 cm).

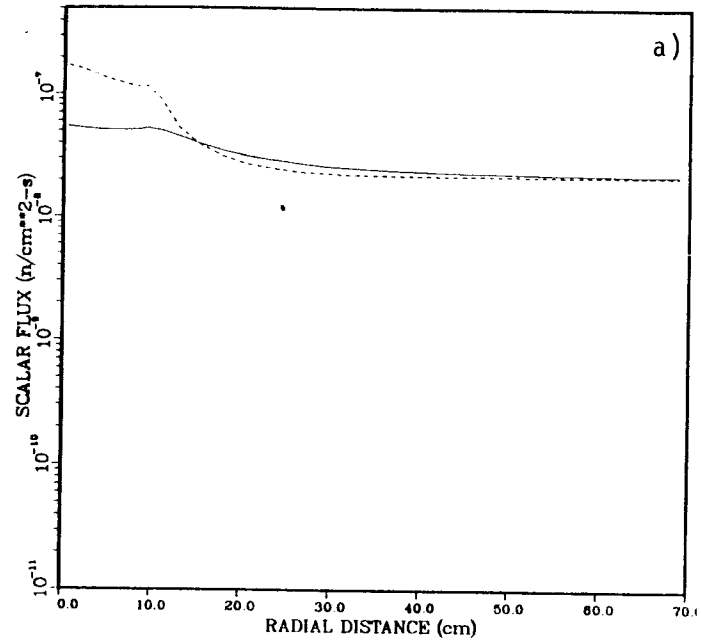

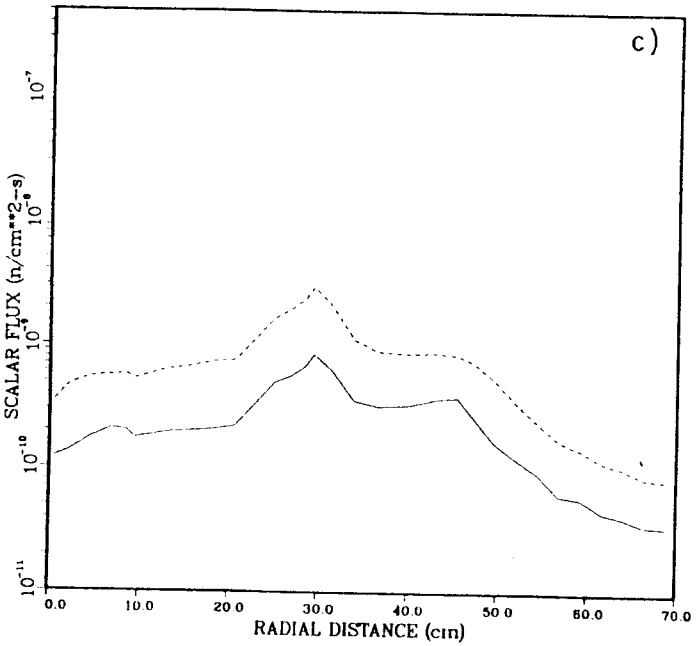

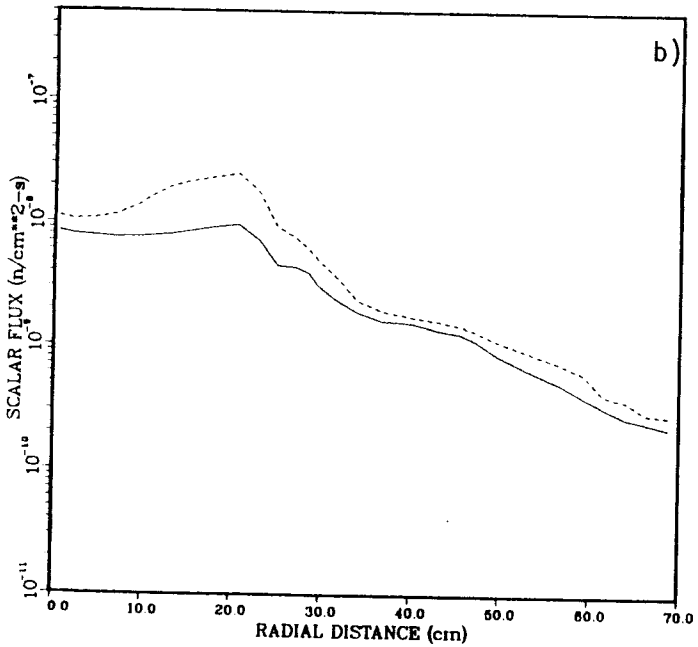

Fig. 2.10. Radial distribution of the neutron flux in group 7 for three axial positions; a) back of graphite moderator (z = 100 cm), b) front of diode (z = 170 cm), and c) back of diode (z = 210 cm).

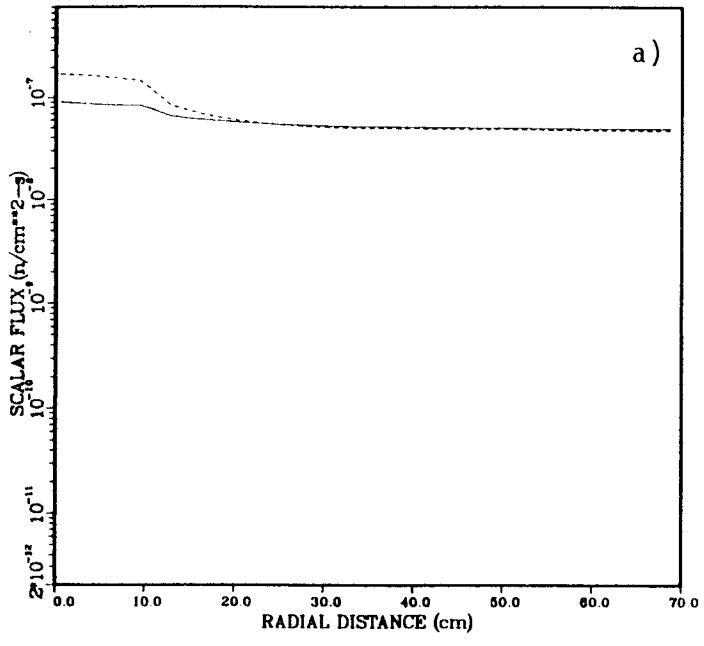

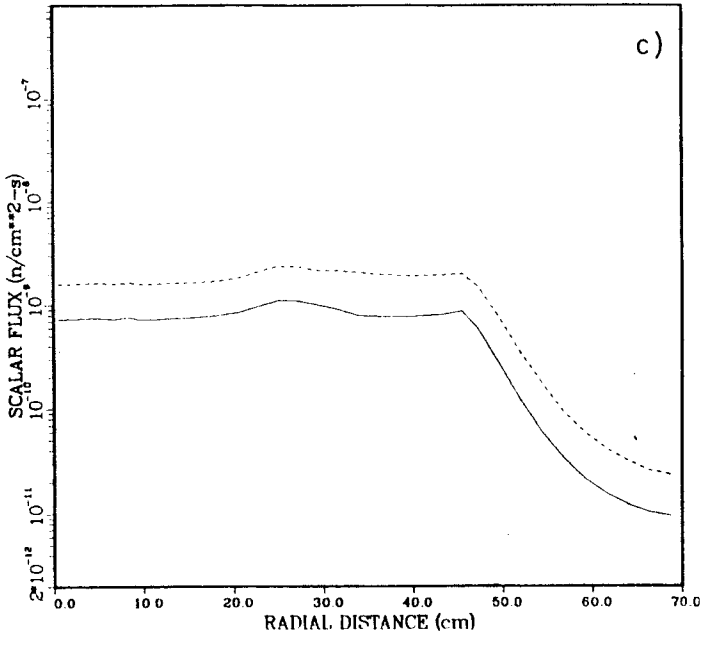

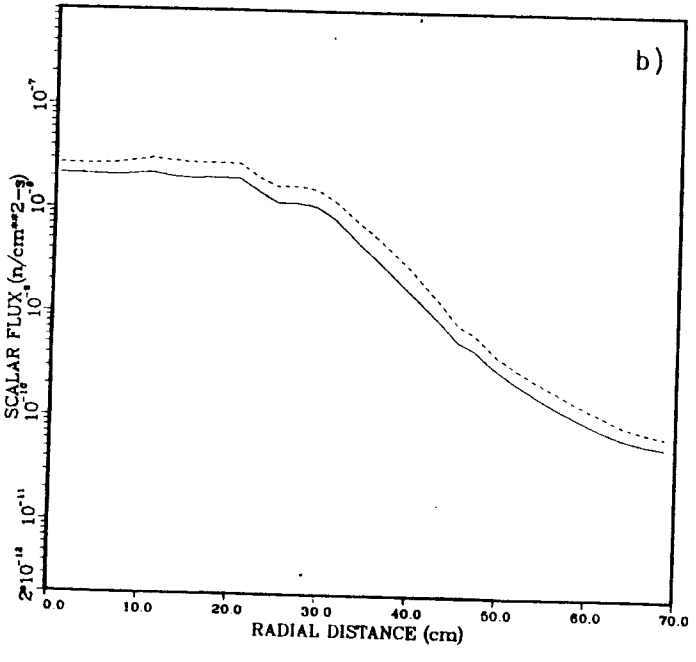

Fig. 2.11. Radial distribution of the neutron flux in group 20 for three axial positions; a) back of graphite moderator (z = 100 cm), b) front of diode (z = 170 cm), and c) back of diode (z = 210 cm).

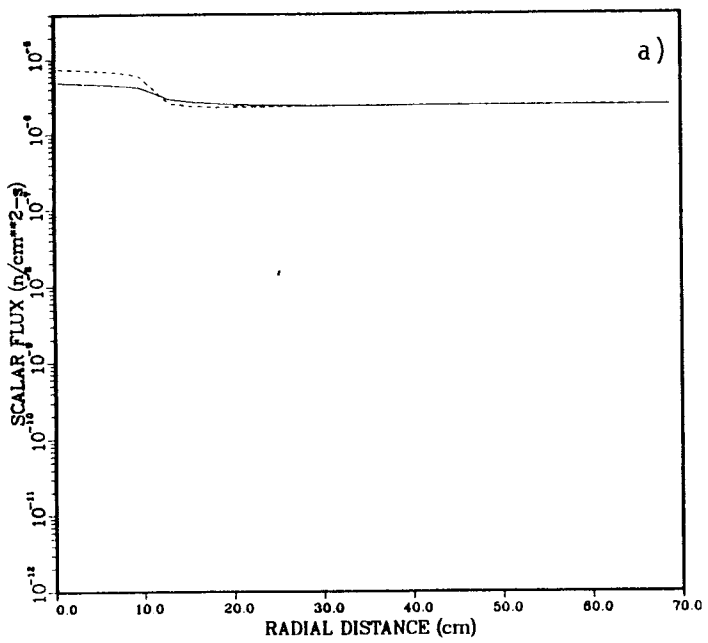

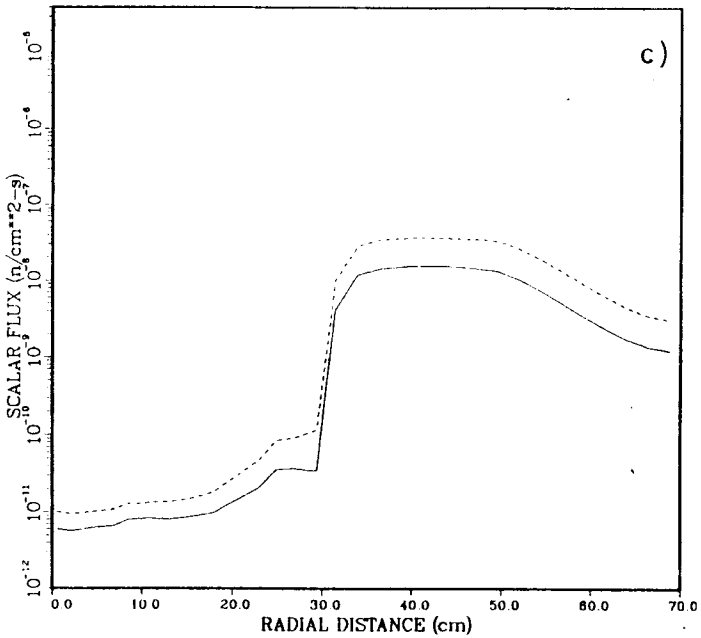

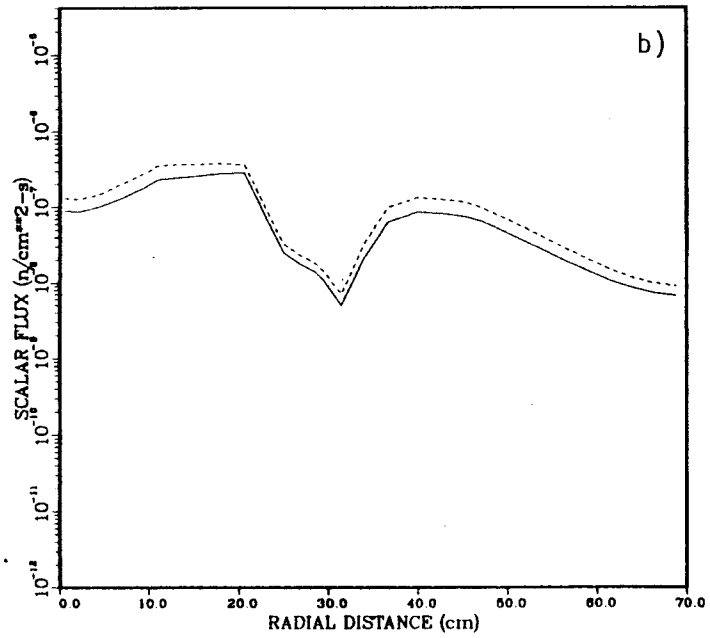

Fig. 2.12. Radial distribution of the neutron flux in group 30 for three axial positions; a) back of graphite moderator (z = 100 cm), b) front of diode (z = 170 cm), and c) back of diode (z = 210 cm).

the target and is negligible for lower energy groups. The structure in the radial distribution of thermal neutrons is due to the radial distribution of the material with the dip around r = 30 cm resulting from attenuation in the front parts of the cathode and Cu coil. It is clear also that the effect of compressing the moderator thickness to 30 cm on the flux at the front of the diode becomes less pronounced for lower energy groups. The structure in the radial distribution at the back of the diode can be related to the distribution of the materials in the diode. It is interesting to note that the radial distribution of flux at the back of the diode is the same for the two moderator thicknesses with the difference in absolute values decreasing for lower energy groups.

2.3 Dose Rate Calculation

The dose rate calculations were performed using the DKR-ICF[4] code package. The spatial model used for the diode calculations is identical to the model used for the TWODANT neutronic calculation and is given in Fig. 2.8. The large dot drawn next to the diode casing designates the point at which the dose rate is calculated. The dose rate calculations are dominated by the radioactivity computation which takes approximately 9-10 hours of Cray-XMP time per case.

A new computational model has been developed for the activation calculations to account for the sequential pulse operation mode of the Target Development Facility. Treating the pulsed problem as a time averaged steady state problem can lead to significant errors in the calculated activity and dose. These differences are illustrated here by comparing the analytic expressions for the radioactive nuclide density obtained using pulsed and

equivalent steady state irradiation for a simple radioactive decay chain with idealized pulse shape.

Consider a series of n square pulses that have a width δ seconds and are Δ seconds apart as illustrated in Fig. 2.13. In the analysis performed here, it is assumed that $\Delta >> \delta$. The equivalent steady state neutron flux ϕ_s is related to the flux ϕ_p during the pulse via

$$\phi_s = \frac{\delta}{\Delta} \phi_p \ . \tag{1}$$

It is assumed that neutrons interact with a nuclide of initial concentration $N_o(0)$ with a cross section σ to produce a radioactive nuclide which has a decay constant λ and that it decays into a stable nuclide. Also assumed is that the radioactive nuclide is not further transmuted by neutron capture. The concentration of the radioactive nuclide at time t during the operation at a flux level ϕ is given by

$$N(t) = \frac{N_o(0)\ \sigma\phi}{\lambda - \sigma\phi} \left(e^{-\sigma\phi t} - e^{-\lambda t}\right) \ . \tag{2}$$

Assuming $\delta << \frac{1}{\lambda}$ and $\frac{1}{\sigma\phi_p}$, N at the end of the first pulse is $N_o(0)\ \sigma\phi_p\delta$. At shutdown (the end of the n^{th} pulse) the contribution from the first pulse will be $N_o(0)\ \sigma\phi_p\delta e^{-(n-1)\lambda\Delta}$. Adding the contributions from the n pulses the concentration of the radioactive nuclide at shutdown is given by

$$N_p = N_o(0)\ \sigma\phi_p\delta e^{-(n-1)\sigma\phi_p\delta} \sum_{i=1}^{n} e^{-(n-1)(\lambda\Delta-\sigma\phi_p\delta)} \ . \tag{3}$$

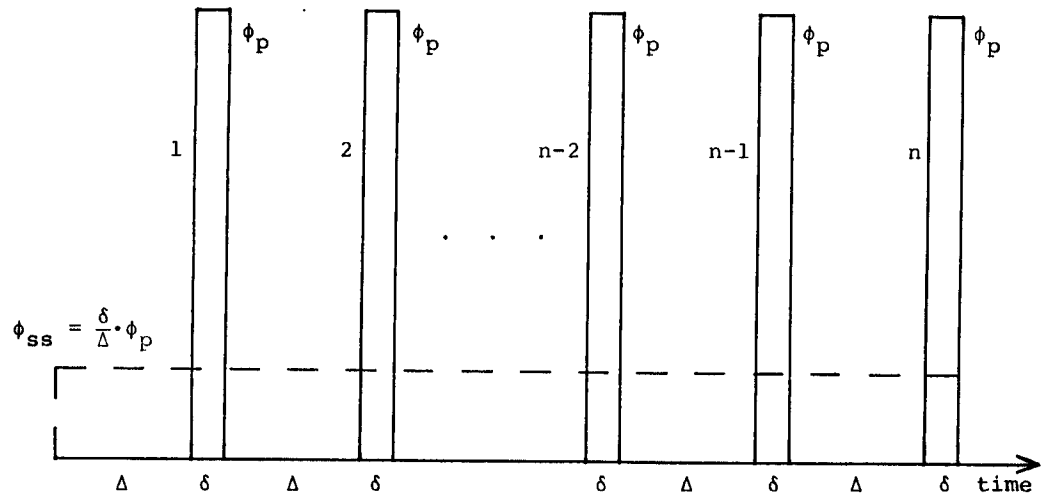

Fig. 2.13. Relation between the neutron flux during the pulse and the equivalent steady state flux.

The geometric progression in Eq. (3) reduces to a closed form and N_p is given by

$$N_p = N_o(0)\ \sigma\phi_p\delta\ \frac{\left[e^{-n\sigma\phi_p\delta} - e^{-n\lambda\Delta}\right]}{\left[e^{-\sigma\phi_p\delta} - e^{-\lambda\Delta}\right]} . \tag{4}$$

Using Eqs. (1) and (2), the corresponding expression for the equivalent steady state case is

$$N_s = \frac{N_o(0)\ \sigma\phi_p\delta}{\lambda\Delta - \sigma\phi_p\delta}\left[e^{-n\sigma\phi_p\delta} - e^{-n\lambda\Delta}\right] . \tag{5}$$

Equations (4) and (5) imply that

$$\frac{N_p}{N_s} = \frac{\lambda\Delta - \sigma\phi_p\delta}{\left[e^{-\sigma\phi_p\delta} - e^{-\lambda\Delta}\right]} . \tag{6}$$

This relation between N_p and N_s will hold at any time after shutdown.

For nuclides with very short half lives ($\lambda\Delta >> 1$) Eq. (6) reduces to

$$\frac{N_p}{N_s} = \lambda\Delta \ , \tag{7}$$

implying that the steady state calculation will underestimate the activity by a factor of $\lambda\Delta$. On the other hand for very long lived nuclides ($\lambda\Delta << 1$), Eq. (6) reduces to

$$\frac{N_p}{N_s} = 1 \ . \tag{8}$$

This implies that the equivalent steady state model gives results identical to the actual pulsed case only for very long lived isotopes. The relation between the pulsed and equivalent steady state results gets complicated for nonuniform pulsing schedules and when decay chains with more than one radioactive nuclide are considered.

The simple example discussed above is extended to determine the activity following a nonuniform pulse schedule as used for TDF. The temporal model as briefly outlined in Fig. 2.14 computes the production of the radioactive nuclides only during the pulse and allows for decay between pulses. In the example depicted in Fig. 2.14 the accumulation of the radionuclide for 12 shots per day is given by S_{12}^{D}. Following the operation of the facility for 5 days a week the radionuclide concentration is given by S_{5}^{W}. The yearly accumulation after 52 weeks is given by S_{52}^{Y}. $Q(\delta)$ denotes the production of the radionuclide during the pulse. The underlying assumptions of this model are that the pulse width, δ (time of irradiation), is much smaller than the time

DAILY PULSE SEQUENCE

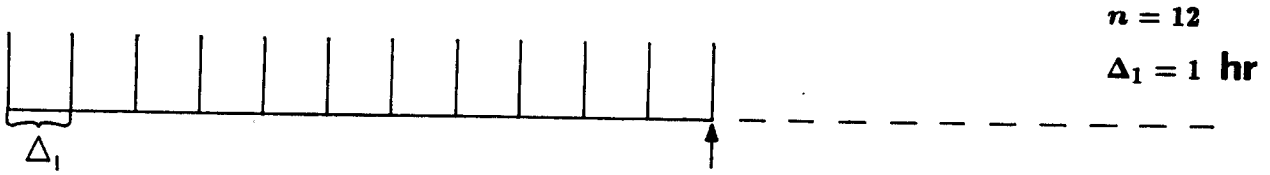

$$S_n^D = Q(\delta)[1 + e^{-\lambda\Delta_1} + e^{-\lambda 2\Delta_1} + e^{-\lambda 3\Delta_1} + e^{-\lambda 4\Delta_1} + e^{-\lambda 5\Delta_1} + \cdots + e^{-\lambda 11\Delta_1}]$$

$$S_n^D = \frac{Q(\delta)(1 - e^{-\lambda\Delta_1 n})}{(1 - e^{-\lambda\Delta_1})} \xrightarrow{n=12} \boxed{S_{12}^D = \frac{Q(\delta)(1-e^{-12\lambda\Delta_1})}{(1-e^{-\lambda\Delta_1})}}$$

WEEKLY PULSE SEQUENCE

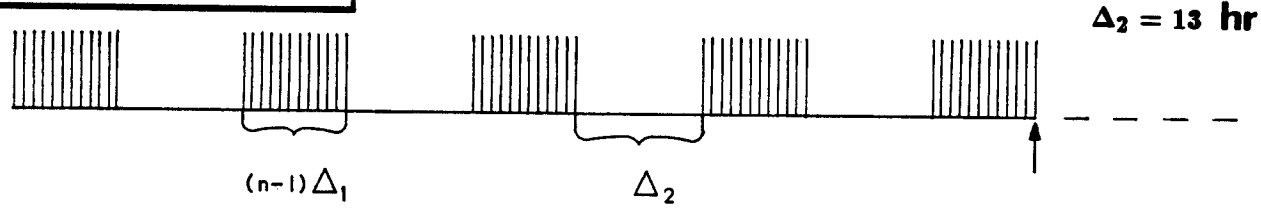

$$S_m^W = S_{12}^D[1 + e^{-\lambda(\Delta_2+(n-1)\Delta_1)} + e^{-\lambda 2(\Delta_2+(n-1)\Delta_1)} + e^{-\lambda 3(\Delta_2+(n-1)\Delta_1)} + e^{-\lambda 4(\Delta_2+(n-1)\Delta_1)}]$$

$$S_m^W = S_{12}^D \frac{(1 - e^{-\lambda m(\Delta_2+(n-1)\Delta_1)})}{(1 - e^{-\lambda(\Delta_2+(n-1)\Delta_1)})} \xrightarrow[m=5]{n=12} \boxed{S_5^W = S_{12}^D \frac{(1-e^{5\lambda(\Delta_2+11\Delta_1)})}{(1-e^{-\lambda(\Delta_2+11\Delta_1)})}}$$

YEARLY PULSE SEQUENCE

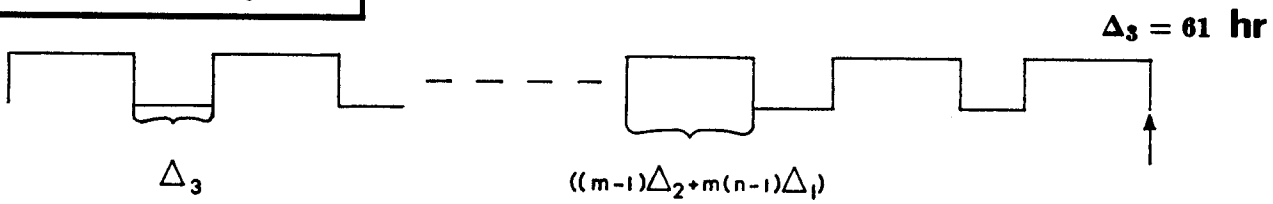

$$S_l^Y = S_5^W[1 + e^{-\lambda(\Delta_3+(m-1)\Delta_2+m(n-1)\Delta_1)} + e^{-\lambda 2(\Delta_3+(m-1)\Delta_2+m(n-1)\Delta_1)}$$
$$+ \cdots + e^{-\lambda 51(\Delta_3+(m-1)\Delta_2+m(n-1)\Delta_1)}]$$

$$S_l^Y = S_5^W \frac{(1 - e^{-\lambda l(\Delta_3+(m-1)\Delta_2+m(n-1)\Delta_1)})}{(1 - e^{-\lambda(\Delta_3+(m-1)\Delta_2+m(n-1)\Delta_1)})} \xrightarrow[m=5]{n=12} \boxed{S_{52}^Y = S_5^W \frac{1-e^{-52\lambda(\Delta_3+4\Delta_2+55\Delta_1)}}{(1-e^{-\lambda(\Delta_3+4\Delta_2+55\Delta_1)})}}$$

ASSUMPTIONS: **Time of irradiation << time between pulses**
Neglect burnup of initial and created nuclides

Fig. 2.14. Temporal model to account for the sequential pulse operation mode of the Target Development Facility.

between pulses, Δ (i.e., $\delta << \Delta$) and that the destruction of the initial and created isotopes is neglected.

The adjoint scheme shown in the flowchart diagram of Fig. 2.15 is used to compute the dose rates at the diode casing's outer surface. Four separate computational steps are required to obtain the dose rates. The first step is the determination of the steady state neutron flux throughout the graphite moderator, aluminum first wall, boral and diode regions using the TWODANT transport code. The flux throughout the different regions is used in the second step of the calculation which involves the use of the DKR code to compute material activation resulting from neutron transmutation reactions and the computation of the decay gamma sources. Step three is the determination of the adjoint dose field throughout the facility using the TWODANT transport code and the flux-to-dose rate conversion factors. The fourth and final step is the multiplication of the adjoint field by the gamma decay sources using the DOSE code to obtain the dose rate at the outer surface of the diode casing.

Due to the approximately 9-10 hours of Cray running time for the activation calculations, not all of the different diode material, penetration size and solution mode options could be calculated. Table 2.1 presents the different options and indicates the ones for which dose rates were computed.

The dose rate results are normalized to 200 MJ of target yield. The operational pulse sequence is assumed to be 12 shots per day for 5 days per week for 4 weeks corresponding to a steady state operation time of approximately 1 month. The dose contributions from all components other than from the graphite moderator (for which the contribution is small) are to be determined.

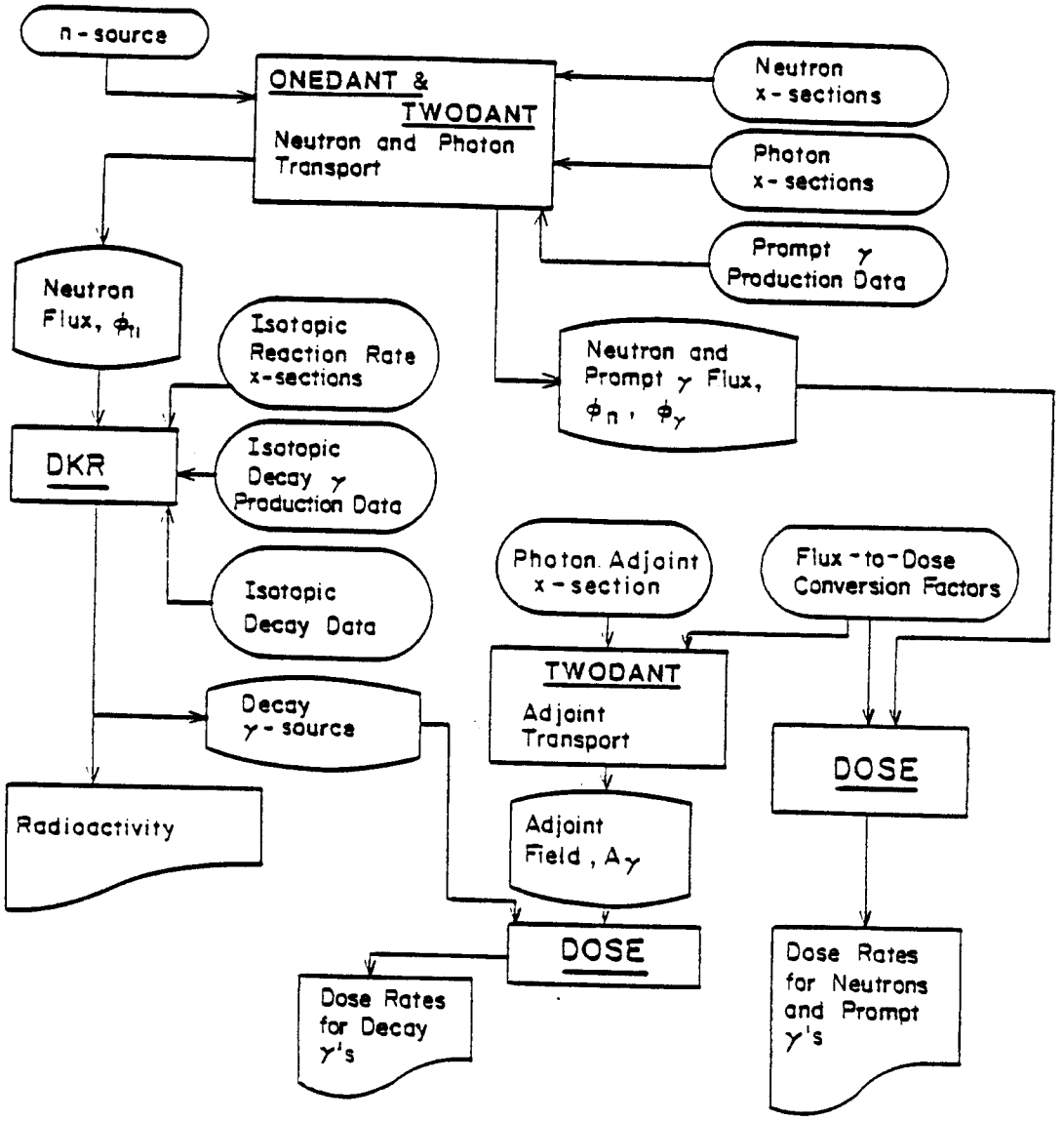

Fig. 2.15. Flowchart for the calculation of dose rates for the Target Development Facility using the adjoint scheme.

Table 2.1. Four Different Diode and Penetration Options

	Case 1	Case 2	Case 3	Case 4
Diode material	SS 304LN	Al-6061-T6	SS 304LN	Al-6061-T6
Radius of graphite moderator penetration	10 cm	10 cm	1 cm	1 cm
Pulsed dose calculation	yes	yes	no	no
Steady state dose calculation	yes	yes	yes	no

The pulse sequence mode dose rate results at the diode casing's outer surface for a 10 cm radius penetration and the different diode materials are shown in Fig. 2.16. For short times after shutdown (up to ~ 2 days) one clearly notes that the aluminum dose rates exceed the stainless steel dose rates. Since the surrounding structure and water shield are identical for both diode materials, the difference between the curves is solely due to transmutation and activation response of each diode material. The initial shape of both curves up to approximately 1 day after shutdown exhibits the same behavior and is determined by the decay of the short-lived isotopes, $^{28}_{13}Al$, $^{30}_{13}Al$, $^{27}_{12}Mg$, $^{26}_{11}Na$ and $^{24}_{11}Na$ produced in the aluminum components. The addition of the aluminum diode dose contribution to that of the surrounding aluminum components accounts for the difference in magnitude up to 1 day after shutdown. The large drop in the aluminum diode dose level from 7.04 rem/hr at 1 day to 12 mrem/hr at 1 week after shutdown is the result of the decay of $^{24}_{11}Na$ which has a half-life of 15 hours. $^{24}_{11}Na$ is produced by a (n,α) reaction on $^{27}_{13}Al$. During the same time interval the stainless steel diode dose

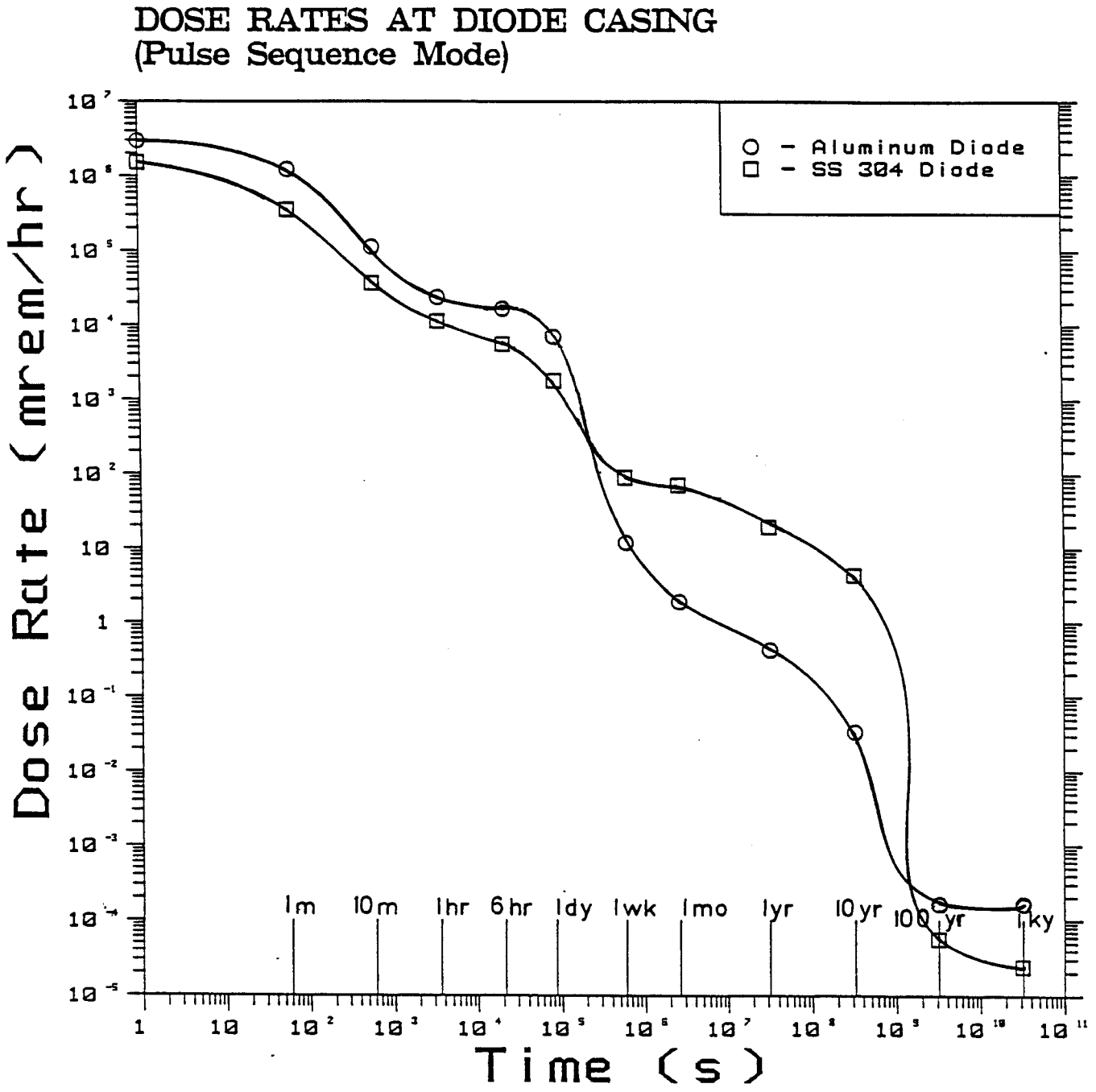

Fig. 2.16. A comparison of the aluminum diode and stainless steel (including surrounding structural material and water shield) dose rates at the diode casing's outer surface using the pulse sequence model.

level drops from 1.8 rem/hr to 90 mrem/hr. The decay of $^{24}_{11}Na$ is again the cause for this drop. The crossover point occurs approximately 2-3 days after shutdown with the stainless steel diode dose exceeding the aluminum diode dose level for nearly 70 years. One must wait approximately 3 days after shutdown for the aluminum case and 5 days after shutdown for the stainless steel case before the dose levels drop below 100 mrem/hr. Table 2.2 contains the radionuclides which produce approximately 90% of the gamma photons for various times after shutdown.

The various components that contribute to the total dose rate at the outer surface of the diode casing are the aluminum first wall, boral lining, plastic insulator, copper coils, aluminum casing (including rotating shutters), water shield and diode material. The dose rate contribution of these components is plotted in Fig. 2.17 for the stainless steel diode case. The $^{16}_{7}N$ with a half-life of 7.10 s is produced in the plastic and water shield and decays to negligible levels within 4-5 minutes after shutdown. As expected, the components containing a high weight percent of aluminum (boral, aluminum first wall and casing) follow the same decay behavior. The aluminum first wall and casing components have a nearly equivalent contribution to the total dose level except for slight differences at early times and in the range 1 day to 1 year after shutdown. This is related to the difference in the neutron energy spectrum in the different zones. The contribution of the boral layers is approximately one order of magnitude lower than the aluminum first wall contribution. Clearly noticeable is the point at which the stainless steel diode component begins to dominate the dose levels. One could imagine removing the diode by remote means at this point to take advantage of the significant drop in the dose contribution of the aluminum components between

Table 2.2. Important Gamma-Photon Producing Isotopes

Stainless Steel 304 Diode

Time 0	1 hr	1 day	1 week	1 month	1 yr
Al-28	Cr-51	Cr-51	Cr-51	Cr-51	Mn-54
V-52	Mn-56	Mn-54	Mn-54	Mn-54	Co-58
Mn-56		Co-58	Co-58	Co-58	Co-60
Al-30		Co-58	Co-57	Co-57	Co-57

Aluminum Diode

Time 0	1 hr	1 day	1 week	1 month	1 yr
Na-24	Na-24	Na-24	Na-24	Cr-51	Mn-54
Na-26	Mg-27	Cu-64	Cr-51	Mn-54	Zn-65
Mg-27	Mn-56		Mn-54	Zn-65	
Al-28	Cu-64		Zn-65		
Al-30					

Water Shield

Time 0	1 hr	1 day	1 week	1 month	1 yr
N-16	---	---	---	---	---

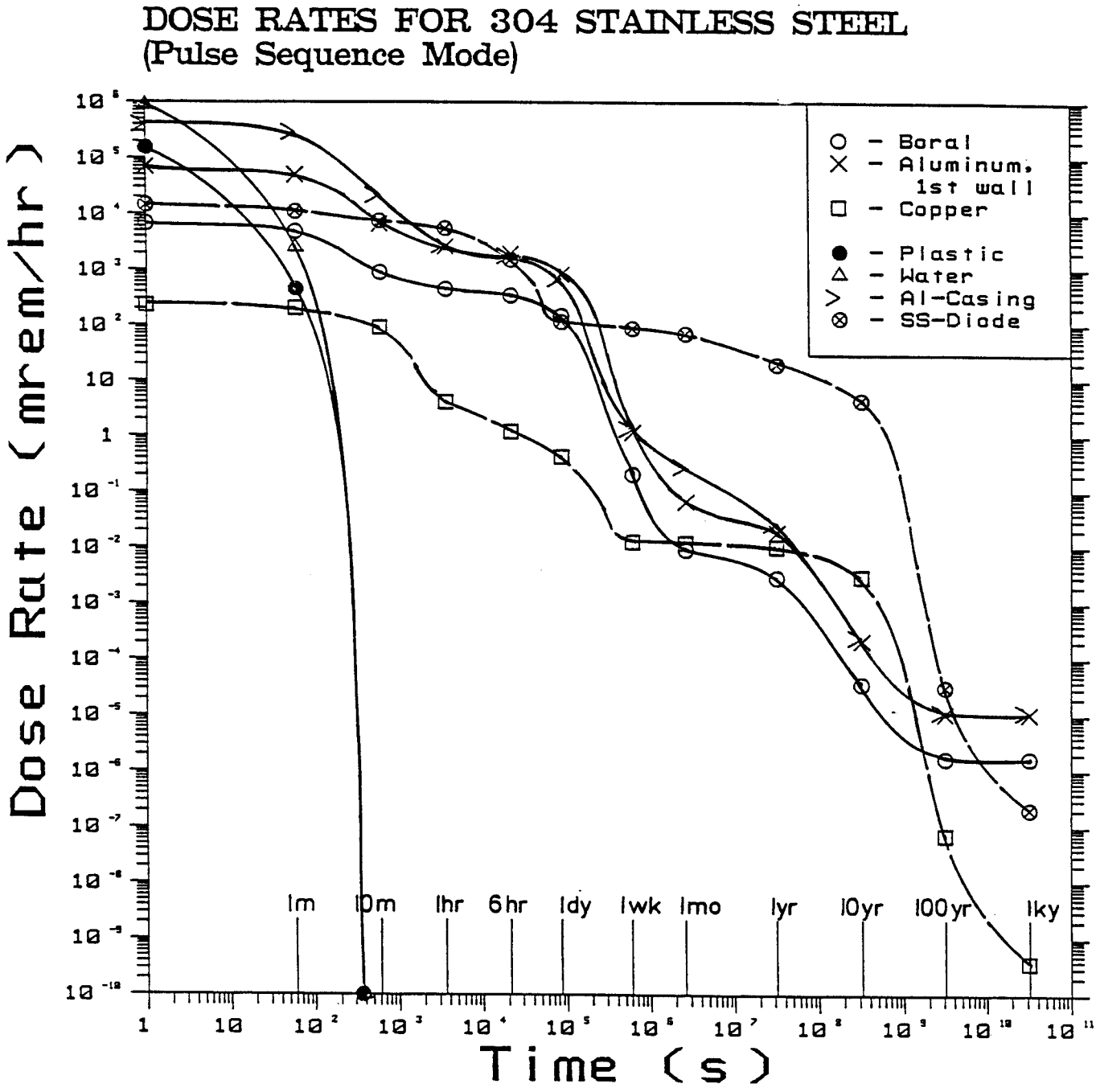

Fig. 2.17. The dose rate contribution of the various structural and shield materials to the total stainless steel dose rate using the pulse sequence model and a penetration radius of 10 cm.

1 day and 1 week after shutdown. The decay of $^{24}_{11}Na$ during this time interval would allow hands on maintenance at the casing's outer surface 1 week after shutdown. Remote handling of the stainless steel diode itself is still required as the dose level does not drop below 50 mrem/hr until 2 months after shutdown. The copper coil dose contribution is 2 to 3 orders of magnitude lower than for the stainless steel and thus its contribution to the total dose rate is small.

The dose level contributions of the various components compromising the aluminum case are shown in Fig. 2.18. Noticeable again is the decay of $^{16}_{7}N$ produced in the plastic and water shield. For the aluminum diode case, the contribution from the diode itself dominates the dose rate and is approximately one order of magnitude larger than the contribution from either the aluminum first wall or the aluminum casing. The contribution from the boral layers is as in the stainless steel, approximately one order of magnitude lower than that from the aluminum first wall. Since the dose level from the aluminum diode component drops considerably between 1 day and 1 week after shutdown, removal of the diode and the diode casing accessibility do not constitute a major hazard. Hands on maintenance of the diode and the diode casing's outer surface is possible 1 week after shutdown. The copper coil dose contribution is lower than the aluminum diode level except in the time interval ~ 2-70 years after shutdown.

Another point to note is the effect the diode material has on the embedded copper coil dose contribution. For the aluminum diode case the copper dose contribution is approximately one order of magnitude larger than for the stainless steel diode case. This is attributed to inelastic scattering in the

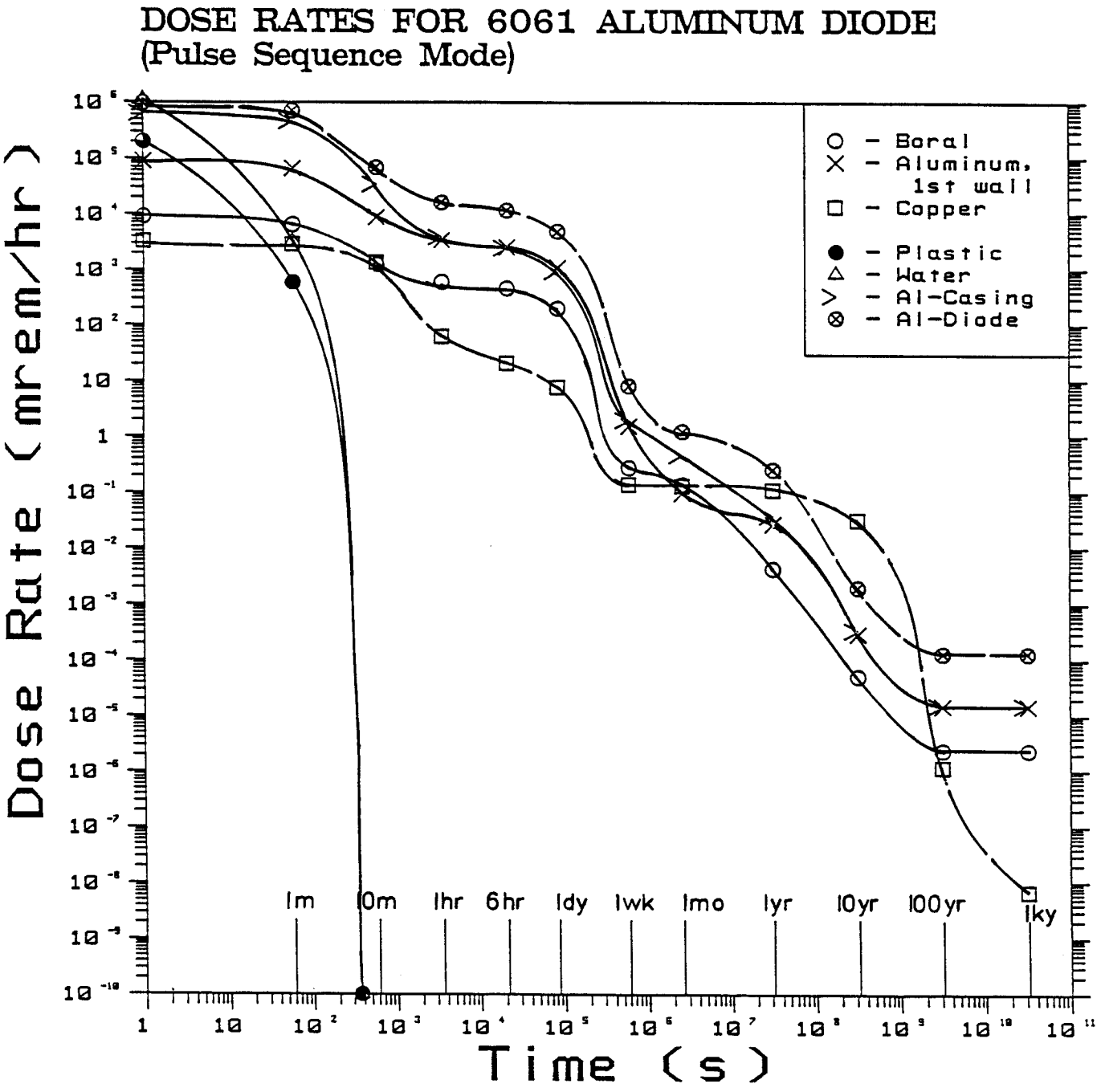

Fig. 2.18. The dose rate contribution of the various structural and shield materials to the total aluminum dose rate using the pulse sequence models and a penetration radius of 10 cm.

Fe contained in the stainless steel which depresses the high energy flux within the diode.

For both the aluminum and stainless steel cases that are examined the dose rates at the diode casing's outer surface are above 1 rem/hr at 1 day after shutdown. At approximately 3 days after shutdown for the aluminum case and 5 days after shutdown for the stainless steel case the dose level has dropped to 100 mrem/hr. Thereafter the dose level drops to 90 mrem/hr for the stainless steel case and 12 mrem/hr for the aluminum case at 1 week after shutdown. Thus, waiting longer than 1 week after shutdown to remove the stainless steel diode is not beneficial as the dose level does not drop below 50 mrem/hr until 2 months after shutdown. Here, remote removal and examination of the diode itself may be necessary with limited hands on maintenance being a possibility. Once the diode has been removed, access to the diode casing is possible after a 1 week shutdown period. For the aluminum diode case waiting until 1 week after shutdown is advantageous as the dose level is considerably reduced. There is a possibility for manual (hands on) removal and examination of the diode.

Note that the above analysis does not take into account increases in the dose level due to sky shining once the water has been removed or streaming of decay gammas down the beam lines once the diode has been removed. These cases should also be addressed at some point during the design.

In Figs. 2.19 and 2.20 a comparison of the results of the pulse sequence and steady state calculations for the stainless steel and aluminum cases are given. For the stainless steel case the curves coalesce at approximately 5 days after shutdown whereas for the aluminum case the curves coalesce at approximately 13-14 days after shutdown. Since the surrounding structural and

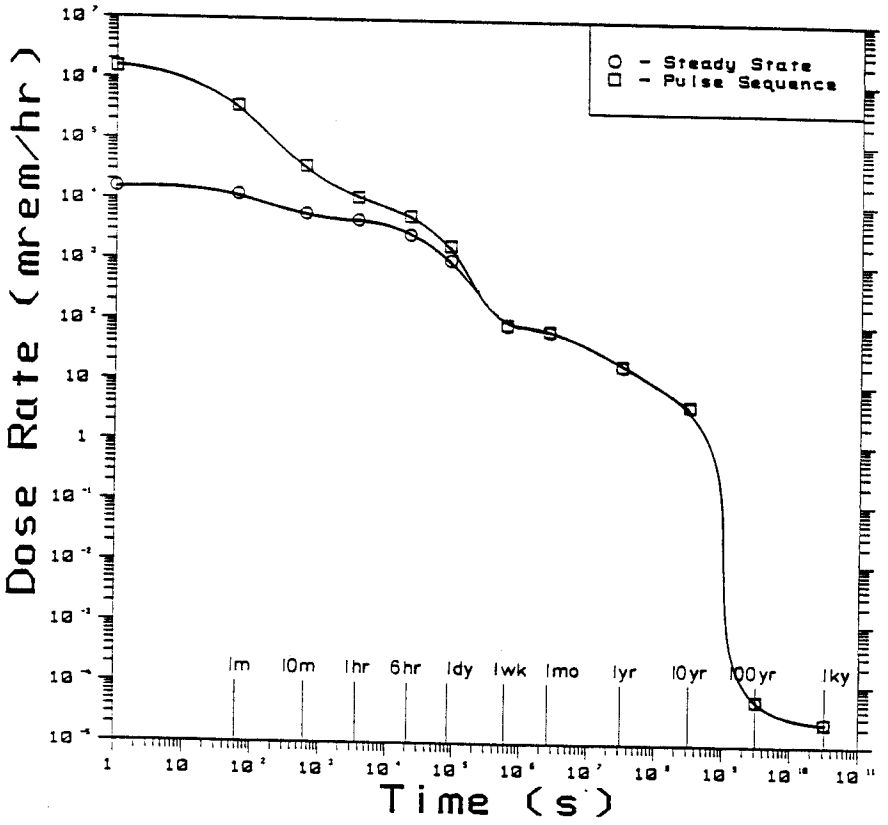

Fig. 2.19. A comparison of the pulse sequence and steady state calculational models for stainless steel using a penetration radius of 10 cm.

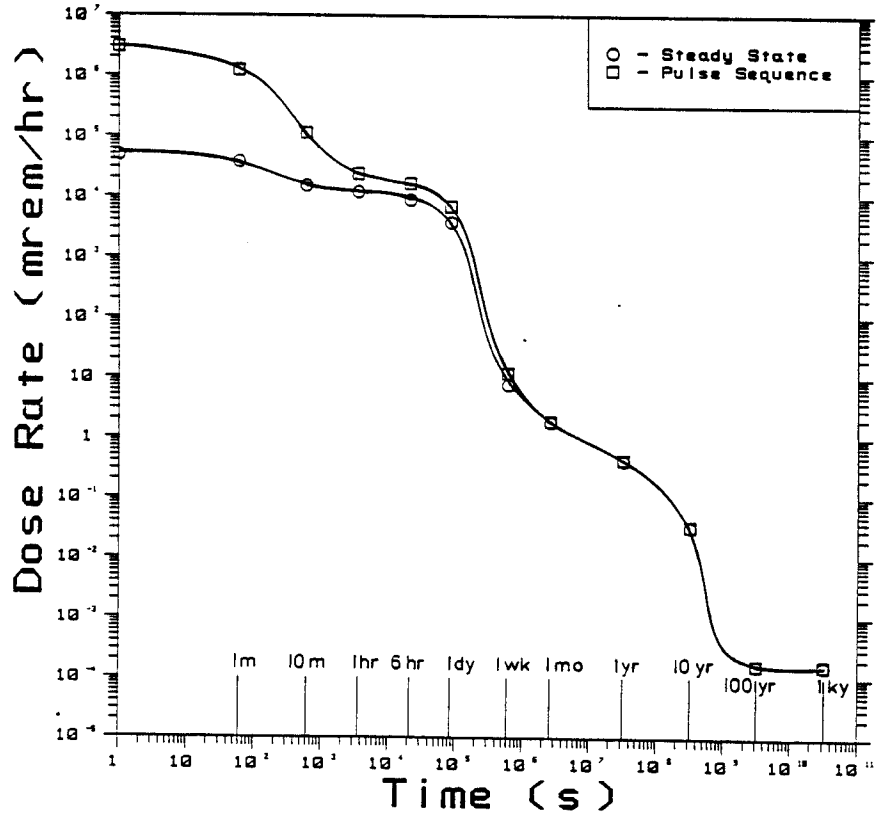

Fig. 2.20. A comparison of the pulse sequence and steady state calculational models for aluminum using a penetration radius of 10 cm.

water shield components are identical, the difference in the time at which the steady state and pulse sequence curves merge is the result of the difference in activation of the diode materials. Specifically, this is mainly the result of the production of $^{54}_{25}Mn$ and $^{51}_{24}Cr$ in both diode materials relative to the production of $^{24}_{11}Na$ in the aluminum diode and surrounding structural components. With the half-lives of $^{54}_{25}Mn$ and $^{51}_{24}Cr$ being 27.7 days and 312.5 days, respectively which are much larger than the largest spacing between pulses (61 hrs), their decay rates are not affected by the pulse sequence. On the other hand, the $^{24}_{11}Na$ which has a 15 hour half-life is affected by the 13 hour shutdown period between daily shot sequences. Hence, the curves begin to merge when $^{54}_{25}Mn$ and $^{51}_{24}Cr$ begin to dominate the total dose level. Since the stainless steel diode has a much larger content of Cr and Fe which are the main producers of $^{54}_{25}Mn$ and $^{51}_{24}Cr$, one would expect a larger production of these radionuclides in the stainless steel diode case than in the aluminum diode case. Thus the stainless steel diode results coalesce at an earlier time than the aluminum diode results. For the aluminum diode case, the curves begin to merge as the contribution of the $^{24}_{11}Na$ to the total dose level drops considerably and the longer lived radionuclides, $^{54}_{25}Mn$ and $^{51}_{24}Cr$, begin to dominate the dose level.

A shortcoming of the discrete ordinates method is the problem of ray effects for singular sources and particles streaming into void regions. Figure 2.21 shows a comparison of the 100 cm and the compressed 30 cm graphite moderator calculations using the stainless steel diode case and the steady state operation assumption. The difference is at most a factor of 2.

One notices that the difference is greater for times up to 1 day after shutdown than for times in the range 1 week-100 years after shutdown. Recall

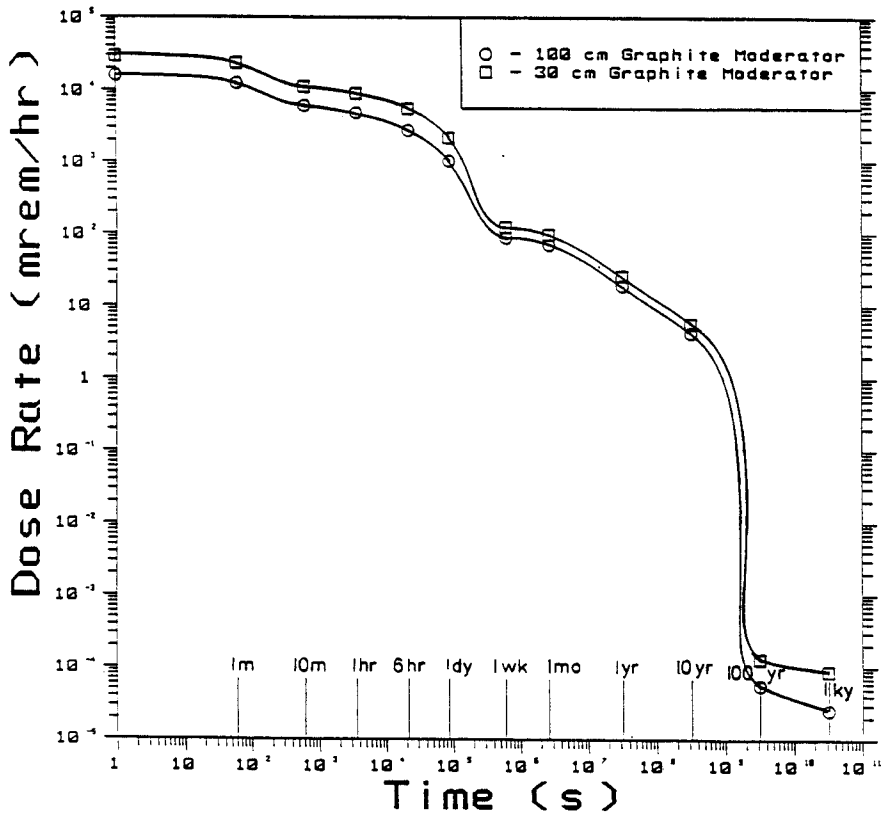

Fig. 2.21. A comparison of the 100 cm and 30 cm graphite moderator dose rate calculations using the steady state model and a penetration radius of 10 cm.

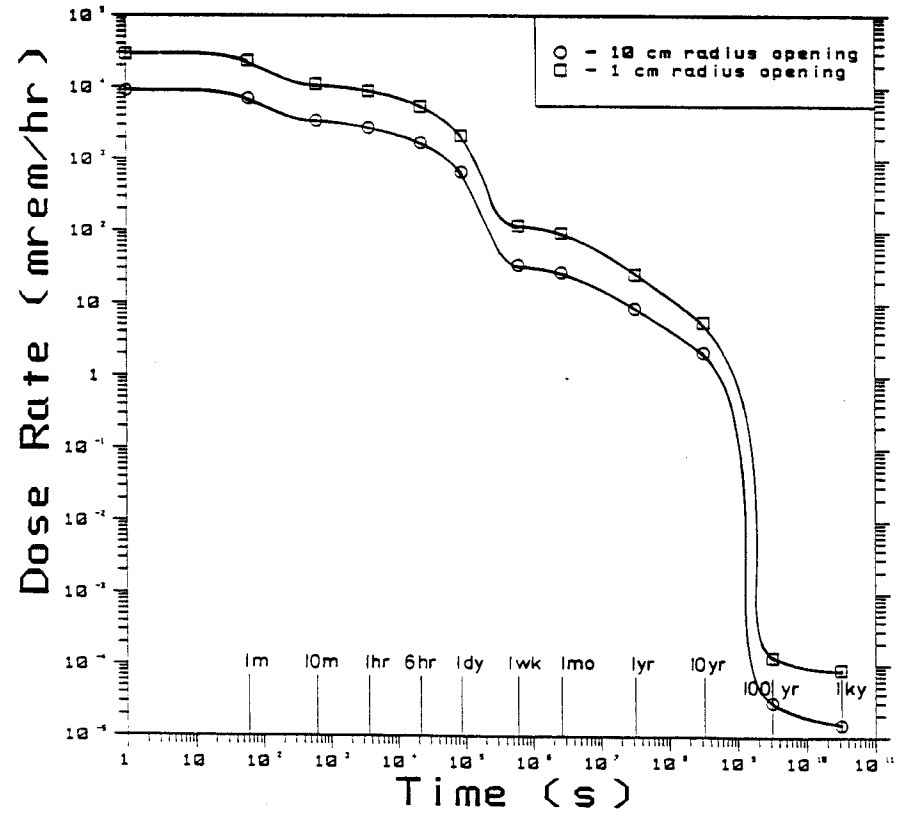

Fig. 2.22. A comparison of the 1 cm and 10 cm penetration radii using the steady state model and the stainless steel diode.

that the radionuclides contributing to the short term dose level are $^{28}_{13}Al$, $^{30}_{13}Al$, $^{27}_{12}Mg$, $^{26}_{11}Na$ and $^{24}_{11}Na$. The $^{27}_{12}Mg$, $^{28}_{13}Al$ and $^{24}_{11}Na$ are produced by the following transmutation reactions; $^{27}_{13}Al(n,p)\ ^{27}_{12}Mg$, $^{27}_{13}Al(n,\alpha)\ ^{24}_{11}Na$ and $^{28}_{14}Si(n,p)\ ^{28}_{13}Al$, respectively, which have reaction threshold energies of 1.9, 3.3 and 4.0 MeV, respectively. The dominating isotopes after 1 week are $^{51}_{84}Cr$ and $^{54}_{25}Mn$ which are produced by the transmutation reactions $^{52}_{24}Cr(n,2n)\ ^{51}_{24}Cr$ and $^{56}_{26}Fe(n,t)\ ^{54}_{25}Mn$. They have reaction threshold energies of 12.3 and 12.1 MeV, respectively. This indicates that the effect is related to the energy spectrum of the neutrons streaming into the diode region and to the angle at which the neutrons stream.

The comparison between the dose levels for the 1 cm and 10 cm radius penetrations is shown in Fig. 2.22. The 30 cm thick graphite moderator results are used for the 10 cm radius penetration case. The difference between the results varies by a factor of 2.5-6 depending on the time after shutdown. This again is related to the estimated factor of ~ 6 larger neutron flux streaming into the diode for the 10 cm radius penetration.

References for Chapter 2

1. D.L. Henderson, R.R. Peterson and G.A. Moses, "Radioactivity in the Light Ion Fusion Target Development Facility," Fusion Tech. 8, 1396 (1985).

2. D.L. Henderson, G.A. Moses and R.R. Peterson, "Activation Studies of the Light Ion Beam Target Development Facility," submitted for publication in the Journal of Nuclear Materials.

3. D.L. Henderson, M.E. Sawan and G.A. Moses, "Radiological Dose Calculations for the Diode Region of the Light Ion Fusion Target Development Facility," University of Wisconsin Fusion Technology Institute Report UWFDM-707, October 1986.

4. D.L. Henderson, "DKR-ICF: A Radioactivity and Dose Rate Calculation Code Package," University of Wisconsin Fusion Technology Institute Report UWFDM-714 (November 1986).

3. CHAMBER MECHANICAL DESIGN AND ANALYSIS

3.1 Mechanical Pulse and Strength Considerations for Graphite Shields

The mechanical response of the reaction chamber structural wall to the internal gas shock is generally characterized as a dynamic stretching and bending motion. However, the first surface is a nonstructural heat shield which also develops mechanical stresses directly from the pulse, i.e. radial compressive stress equal to the instantaneous pressure. The surface stress will generally propagate into the material as a compressive pulse and reflect from an outer free boundary as a tensile pulse of the same shape and magnitude (Fig. 3.1). A strong pulse in a material with very low radial tensile strength could cause failure at the first weak interface from the back. In the case of TDF, the strength requirements in this regard are moderate since the radial tensile and compressive stresses will not exceed the magnitude of the applied dynamic pressure. (The various pressure histories shown in this report include reflective magnification with enhancement greater than classic acoustic doubling because of strong shock effects.)

It should also be noted that the surface of the heat shield will be subjected to high velocity debris. This could generate intense local stresses, delamination of conventional layered composites, surface damage and thus potential crack initiation sites. Also, at higher impact velocities, the shield may not be able to respond quickly enough in flexure, possibly resulting in penetration and perforation. Critical velocity estimates have been made by comparing the local kinetic energy density with the maximum available strain energy density. It appears that millimeter size particles with kinetic energies of a few joules are capable of penetrating conventional composites with thicknesses of a few millimeters.

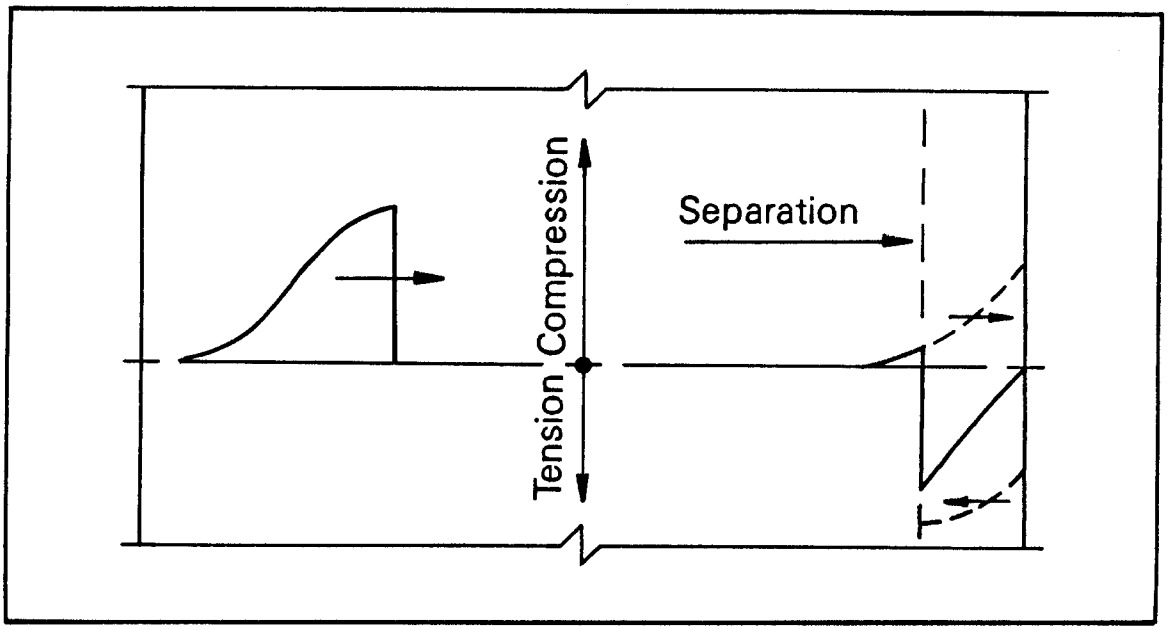

Fig. 3.1. Dynamics of spall generation.

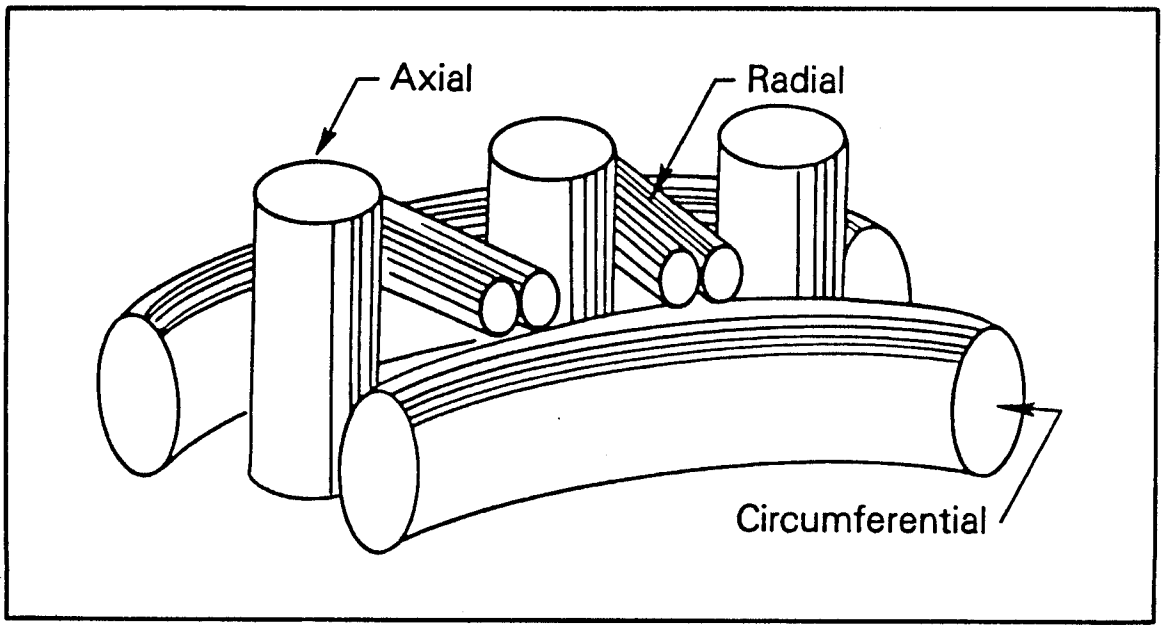

Fig. 3.2. Three-dimensional weave of graphite yarn.

Graphite has been generally identified as the first surface heat shield material. More specifically, it should also have superior mechanical properties, i.e. be relatively "tough", and have good three-dimensional strength. Carbon-carbon composites are now available with 3-D orthogonal and cylindrical weaves (Fig. 3.2).[1] The three-dimensional characteristics are important because of the delamination problem. Planar fiber reinforcement is important (compared with, for example, polycrystalline graphite) for crack arrest at the surface. A variety of geometries, fiber types, strengths and stiffnesses are possible. Representatives of Fiber Materials, Inc.,* a major industrial fabricator of high temperature materials, have recommended that the heat shield be constructed from carbon-carbon composites in the form of large panel/shell components for all surfaces (vertical, top and bottom). Some typical properties are listed in Table 3.1.[1] Strength, modulus values and conductivity are higher than polycrystalline graphites. The thermal expansion coefficient is also lower. (Carbon fibers are available with negative thermal expansion coefficients.)

Between the heat shield and the 3 m radius structural wall of the cylindrical chamber is a relatively thick (50 cm) graphite moderator. Many forms of nonwoven graphite which have been developed as insulation may be applicable. Uses include, for example, high purity vacuum and inert gas furnaces for semiconductor industries.* This graphite can be manufactured in specific configurations and can be easily shaped by drilling, machining, etc. If nuclear quality requirements can also be satisfied, it appears that an appropriate moderator can be designed from such materials. Attachment details of

---

*FMI, Biddeford, ME 04005.

Table 3.1. Representative Properties of 3-D Orthogonal Carbon-Carbon Composites

PRINCIPAL DIRECTIONS	Z	X-Y
Tensile Strength (MPa)		
R.T.	310	103
1900°K	400	124
Tensile Modulus (GPa)		
R.T.	152	62
1900°K	159	83
Compressive Strength (MPa)		
R.T.	159	117
1900°K	196	166
Compressive Modulus (GPa)		
R.T.	131	69
1900°K	110	62
Thermal Conductivity (W/mK)		
R.T.	246	149
1900°K	60	44
Thermal Expansion (10^{-6}/K)		
R.T.	0	0
1900°K	3	4
3000°K	8	11

both the heat shield and moderator would depend, to some degree, on the final size and configuration of the chamber.

3.2 Base Case 3 m Cylindrical Chamber

The base case TDF chamber has been a 3 m radius cylindrical vessel of steel or aluminum. It now includes a 50 cm graphite moderator. A considerable amount of parametric mechanical data for frequencies, stress, strain and fatigue life has been developed.[2] To briefly summarize key features of the analysis, it should be noted that the mechanical response is axisymmetric and also symmetric with respect to the midspan position. Theoretically all vibration modes of this type constitute the response, but as a practical consequence, only a small number of low frequency harmonics need to be considered since the relative contributions diminish quickly with increasing frequencies. For a spatially uniform pressure pulse, the maximum stress occurs at the ends of the cylinder. However, the effect is localized and can be controlled by thickness increases at these locations. The governing design variable then becomes the circumferential normal stress at midspan.

When the overpressure on the structural wall can be characterized as a simple pulse having a width much less than the periods of participating harmonics, its effect is that of an impulsive pressure. This is a widely accepted result and has been the particular situation for 200 MJ yields in 3 m radius vessels of various practical thicknesses.

The 50 cm thick graphite moderator is considered to be a nonstructural assembly. More specifically, if it is composed of a number of individual units there will be no circumferential strength to counteract the radial pressure. It is assumed then, that the moderator acts essentially as a load transfer device. Since the geometric dilution of the loading is linear, the

equivalent radial force reduction is less than 17% from 2.5 to 3 m. Thus for practical purposes, the pressure pulse used for loading the 3 m structural wall is just taken as the value determined at the 2.5 m surface. More specifically, the impulsive pressure is 100 Pa-s for a yield of 200 MJ in nitrogen at 14 torr.

Calculations have been made for chambers of 2.25 Cr-1 Mo steel and welded 6061-T6 aluminum. Maximum stresses are nearly the same because modulus/density ratios are almost coincident but aluminum strains are approximately three times larger than values for steel. The history for a 5 cm wall is shown in Fig. 3.3. The peak stress is 15 MPa (2.2 ksi) and the corresponding doubled strain range for aluminum is 7.8×10^{-4}. Since the endurance limit is 8.3×10^{-4} for welded Al 6061-T6,[2] the design objective of 15,000 shots can be reached for this case and with a greater margin of safety with a slightly thicker wall or by using steel.

3.3 Replaceable 1 m Spherical Chamber

In an effort to develop a more compact facility, the design of a spherical reaction chamber with a one meter radius has been initiated.[3] Theoretically this is also the best shape to carry completely symmetric dynamic pressures. A heat shield is necessary to protect the structural wall but a neutron moderator is not used.

One of the consequences of chamber size reduction is a change in the shape of the pressure pulse at the wall. The usual impulsive spike is followed by a relatively constant pressure. Using the area under such a curve as an equivalent impulse will not result in an accurate representation of the response. The pressure history could be fitted with analytic functions. However, the procedure adopted consists of numerically integrating the equations

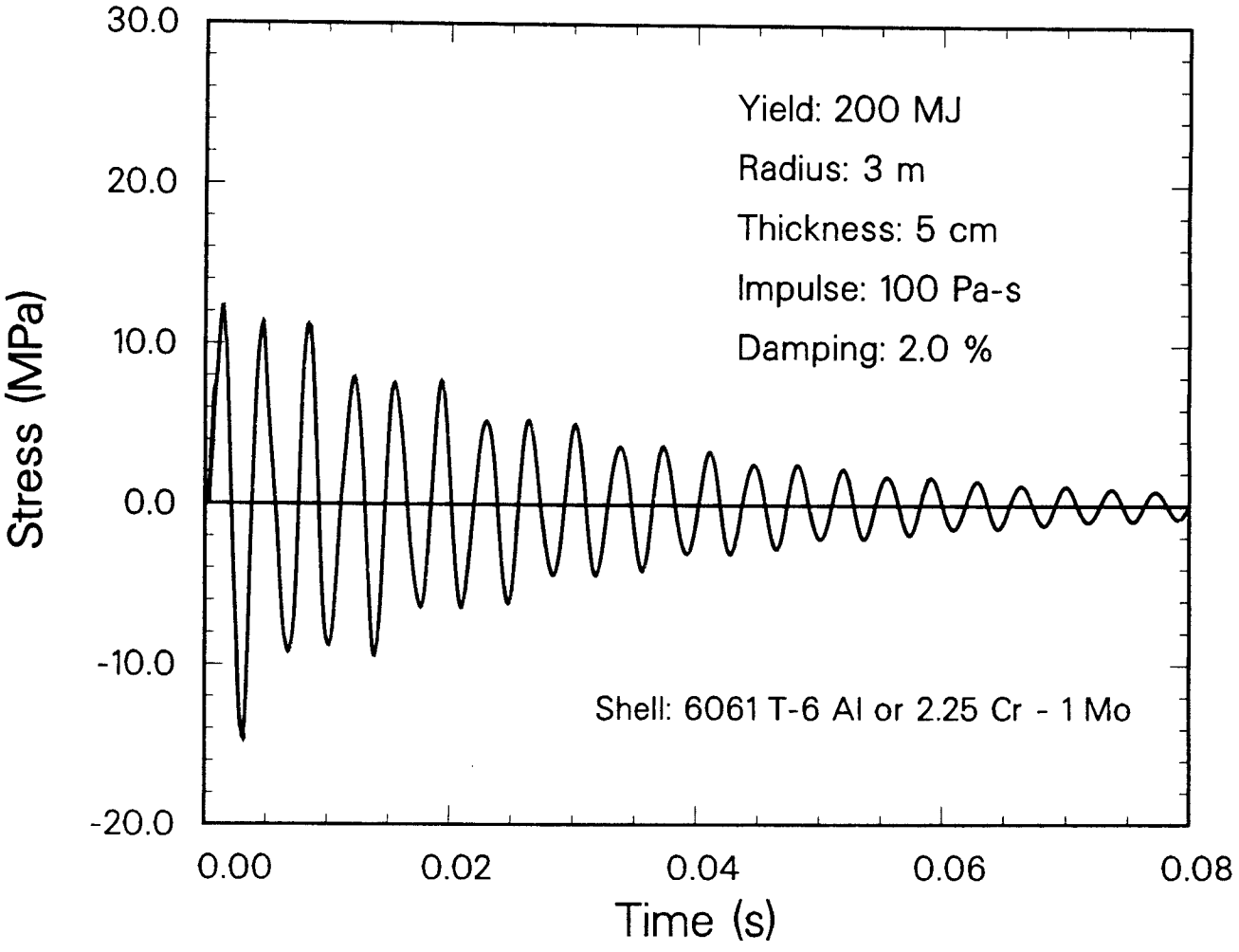

Fig. 3.3. Cylindrical chamber circumferential mechanical stress history.

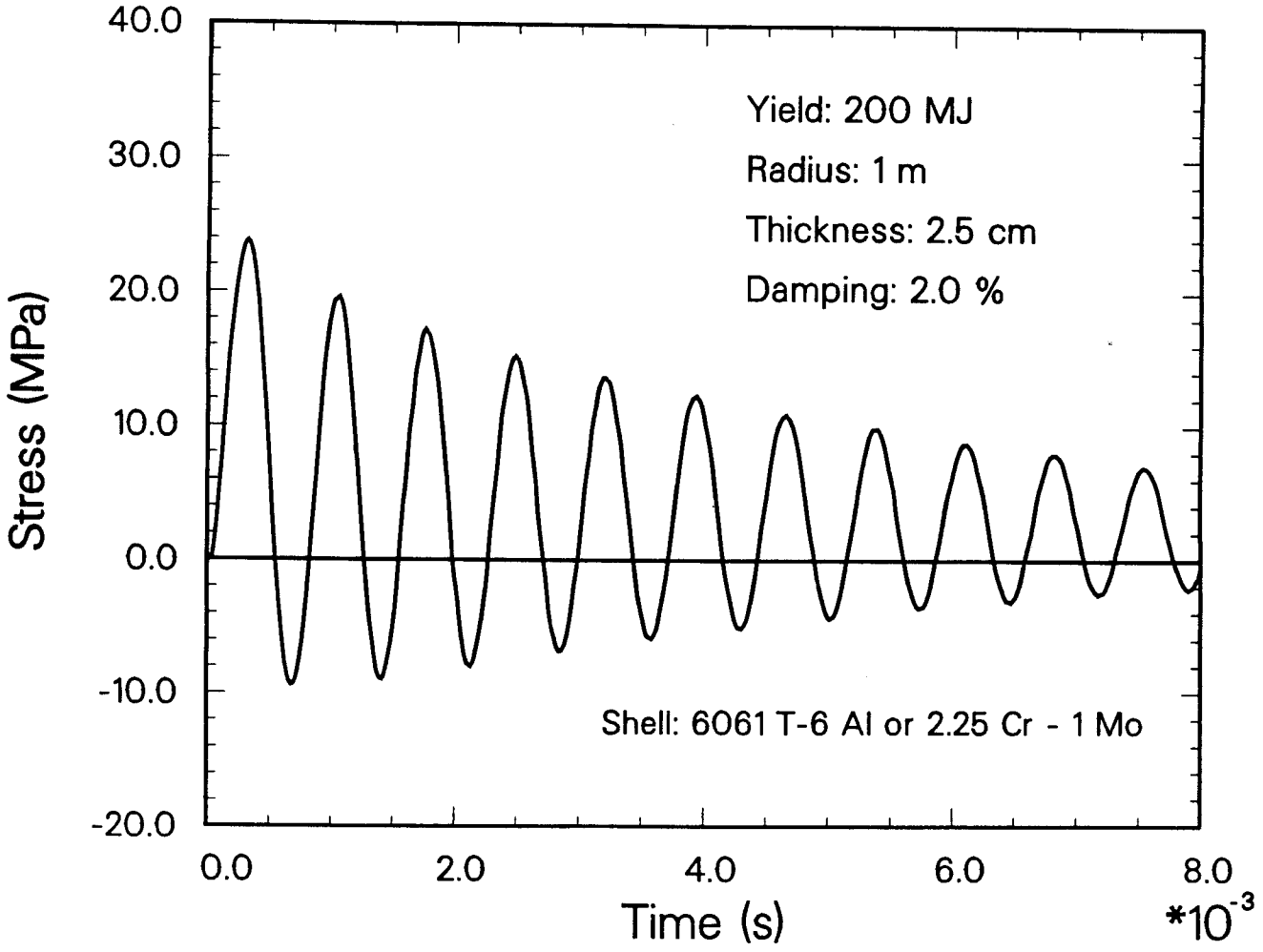

Fig. 3.4. Spherical chamber mechanical stress history.

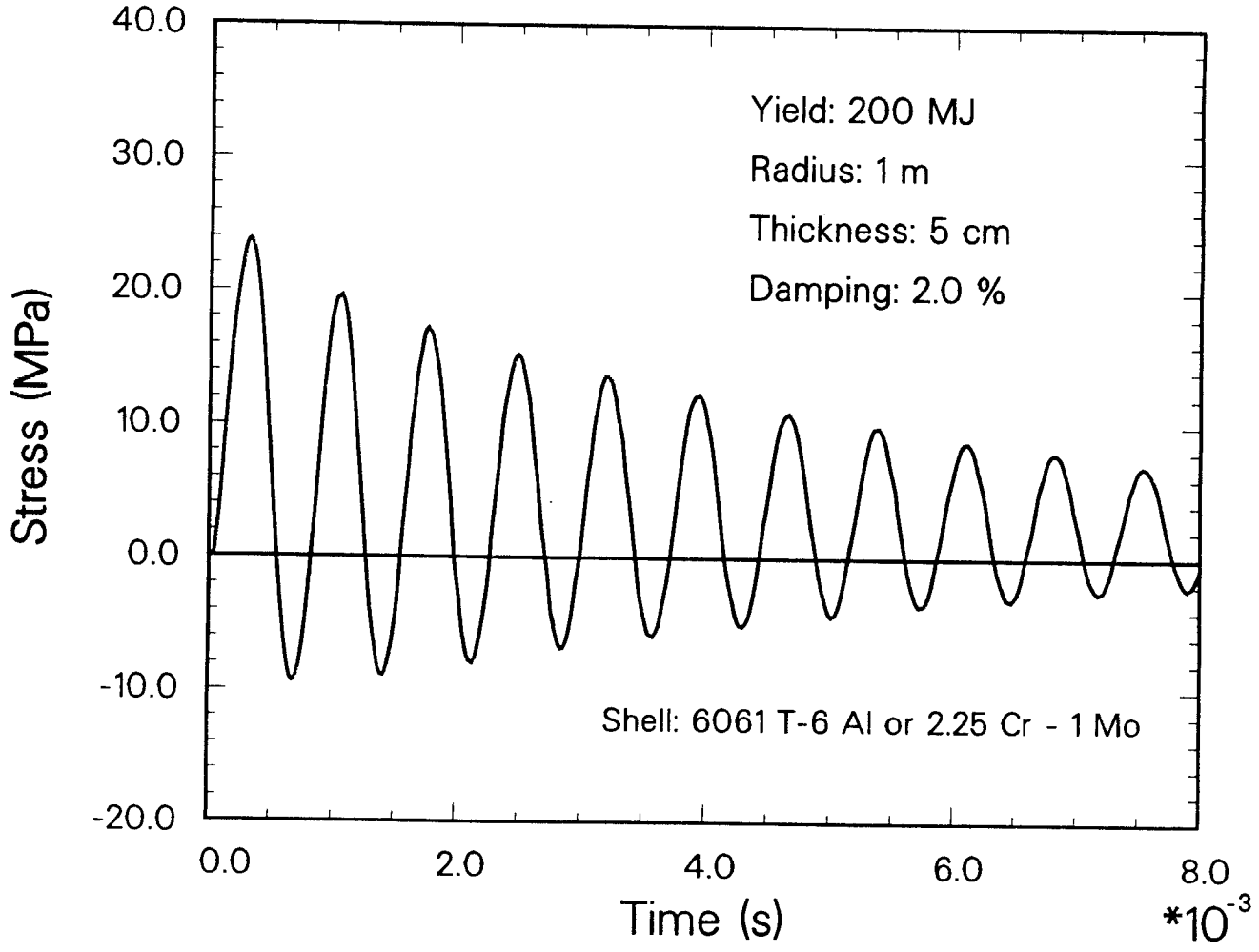

Fig. 3.5. Spherical chamber mechanical stress history.

4. PLASMA CHANNEL MODELING

4.1 WINDOW Code Improvements

The WINDOW computer code[1] has been used for the past few years to study the limits on the ion beam power than can be propagated down a plasma channel. This code is based on the limits derived by Ottinger, Goldstein and Mosher[2] several years ago, which included several assumptions about the nature of the channels. We have endeavored to rederive these power limits where these assumptions have been relaxed.

The assumptions made in the earlier work allowed the derivation of power limits that are relatively simple to use, but are not strictly valid for the plasma channels under consideration for TDF. The background gas was assumed to be deuterium, while in TDF the gas is nitrogen. The spread in the energy of the beam ions as they enter the channel was taken to be 10%, while in TDF the spread is variable because it depends on the channel length and bunching factor. The temperature of the channel electrons and ions before they are heated by the beam was assumed to be 10 eV, while we are not sure what it is in TDF but it depends on the details of the laser heating and the initiation phase of the channel discharge. The channel was calculated to heat as an ideal gas with no radiative cooling, while in simulations of plasma channel behavior we have noticed that radiative heat transfer can be an important effect and it is clear that higher Z gases have heat capacities much greater than that predicted by the ideal gas law.

A new set of beam power limits has been derived, where all of the assumptions in the preceding paragraph have been relaxed. The temperature in the channel at the tail of the ion beam is determined by the standard equation of energy conservation with radiation,

$$\frac{\partial}{\partial t} C_p \rho T = S_{ohmic} - \sigma_B \sigma_{channel} T^4 \quad (1)$$

where C_p is the heat capacity, ρ is the mass density, $\sigma_{channel}$ is the opacity, S_{ohmic} is the heating rate, and T is the temperature of the channel. A solution of Eq. (1) is adopted where either the radiation is not important or the ohmic heating rate is balanced by the radiative losses. The temperature calculated for these two cases is plotted for TDF parameters as a function of the beam power in Fig. 4.1. It is clear from this plot that for TDF radiation cooling of the channel is not important because the radiation limit is so far above the temperature to which ohmic heating would raise the channel. The new version of WINDOW (hereafter called WINDOW-2) chooses the lower of these two temperatures. There have been new equations for the power limits due to two-stream instabilities, beam filamentation due to Weibel and Whistler modes, and filamentation of the channel return current derived from Eqs. 1 through 5 of Reference 2. These are rather long and complicated and will not be presented in this report. A more detailed report will be written on WINDOW-2 that will include these equations.

We will, however, demonstrate the effects of using the new formalism by comparing the window of propagation in beam power versus injection angle space for TDF for the old and new versions of WINDOW. The window of propagation is shown in Fig. 4.2 for WINDOW-1 (the old version) and in Fig. 4.3 for WINDOW-2. In these figures, the beam power limits demanded by considerations of two-stream instability (ES), beam filamentation (BFIL), channel return current filamentation (CFIL), MHD channel expansion (MHD), and beam ion energy loss (ELOSS) are plotted against the diode outer anode radius divided by the diode focal length (R/F). The window of propagation is that region under all of the

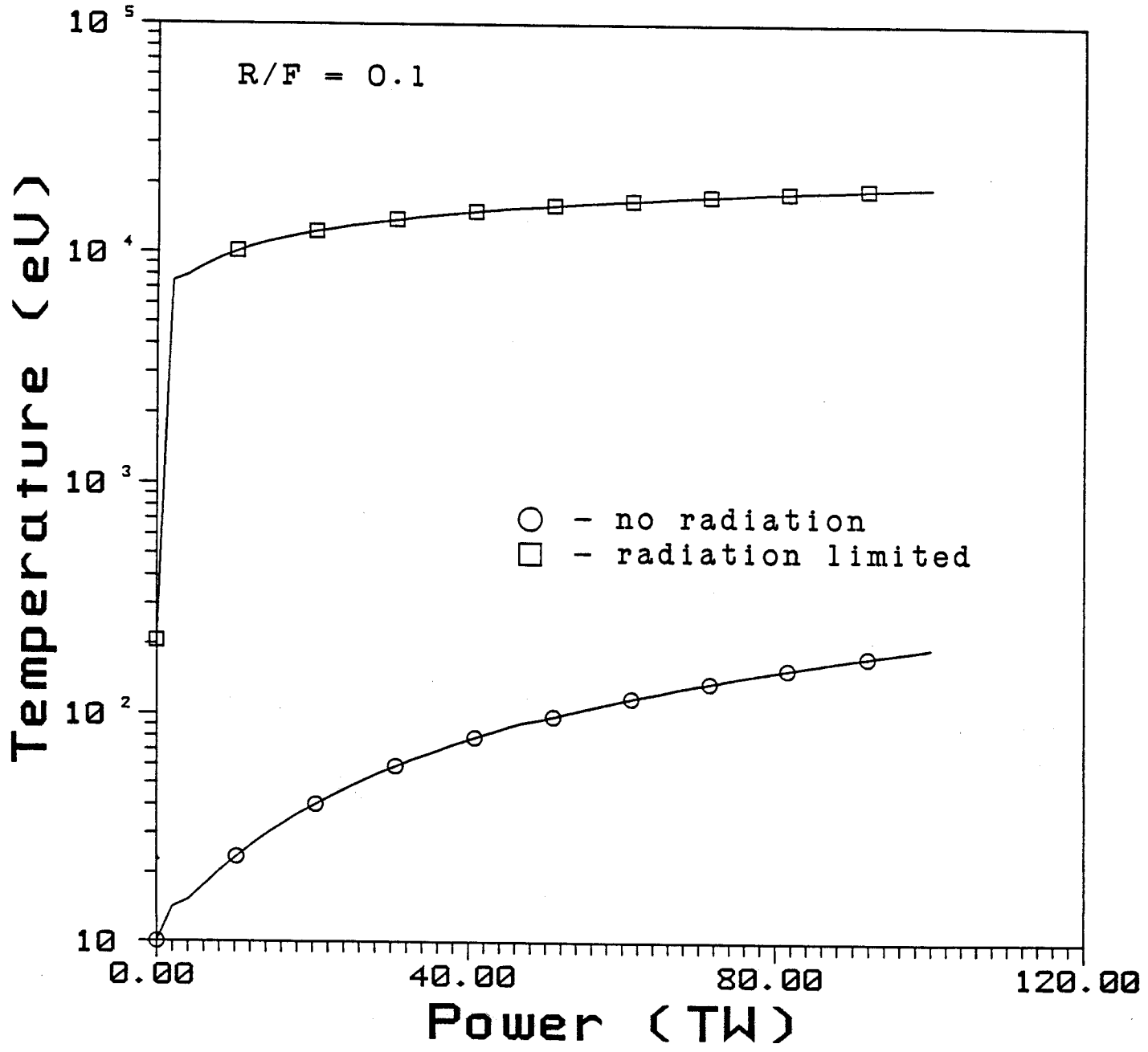

Fig. 4.1. Channel Temperatures for TDF versus Beam Power. R/F is 0.1.

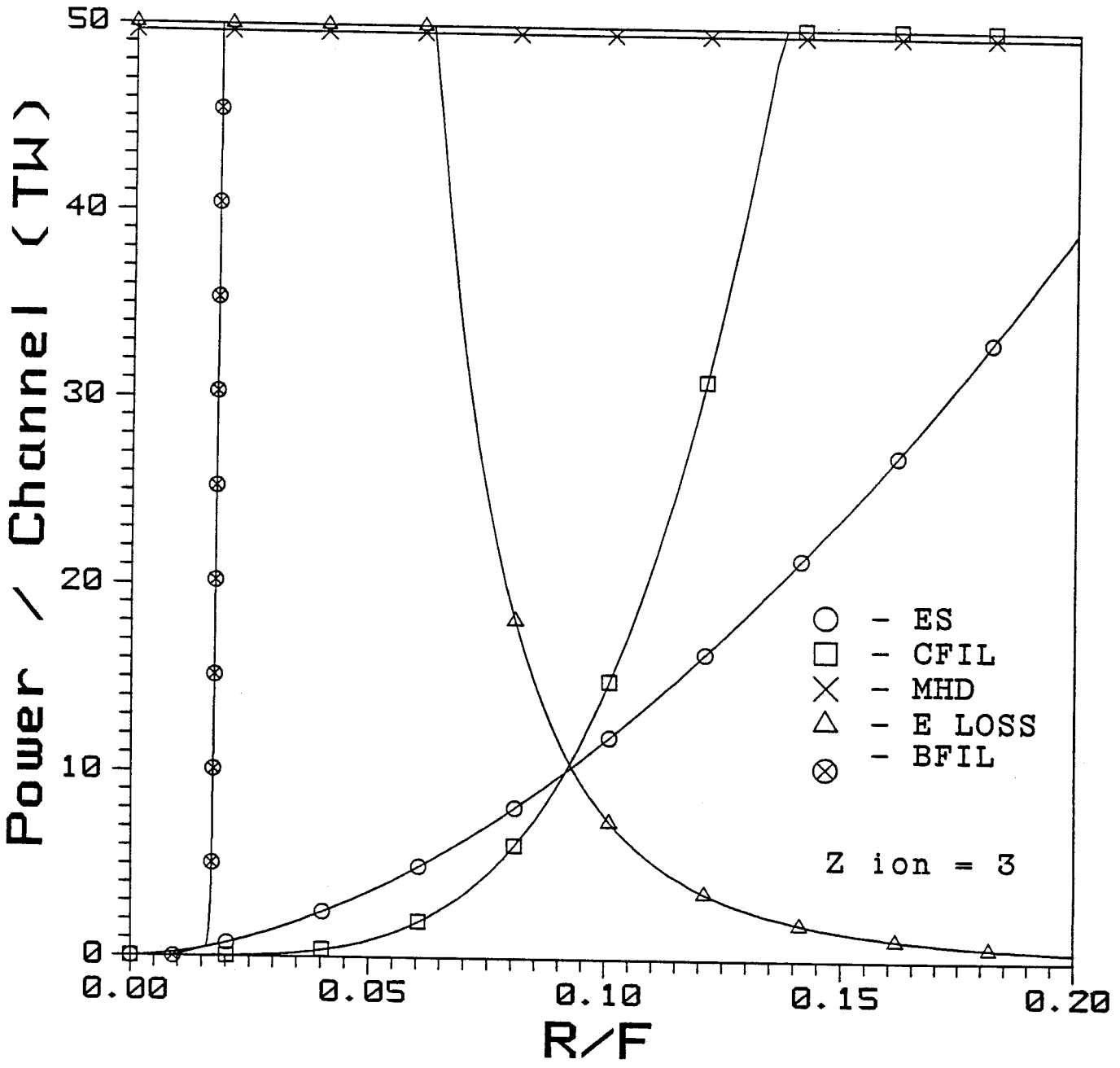

Fig. 4.2. Beam Propagation Window for TDF as Calculated by WINDOW-1.

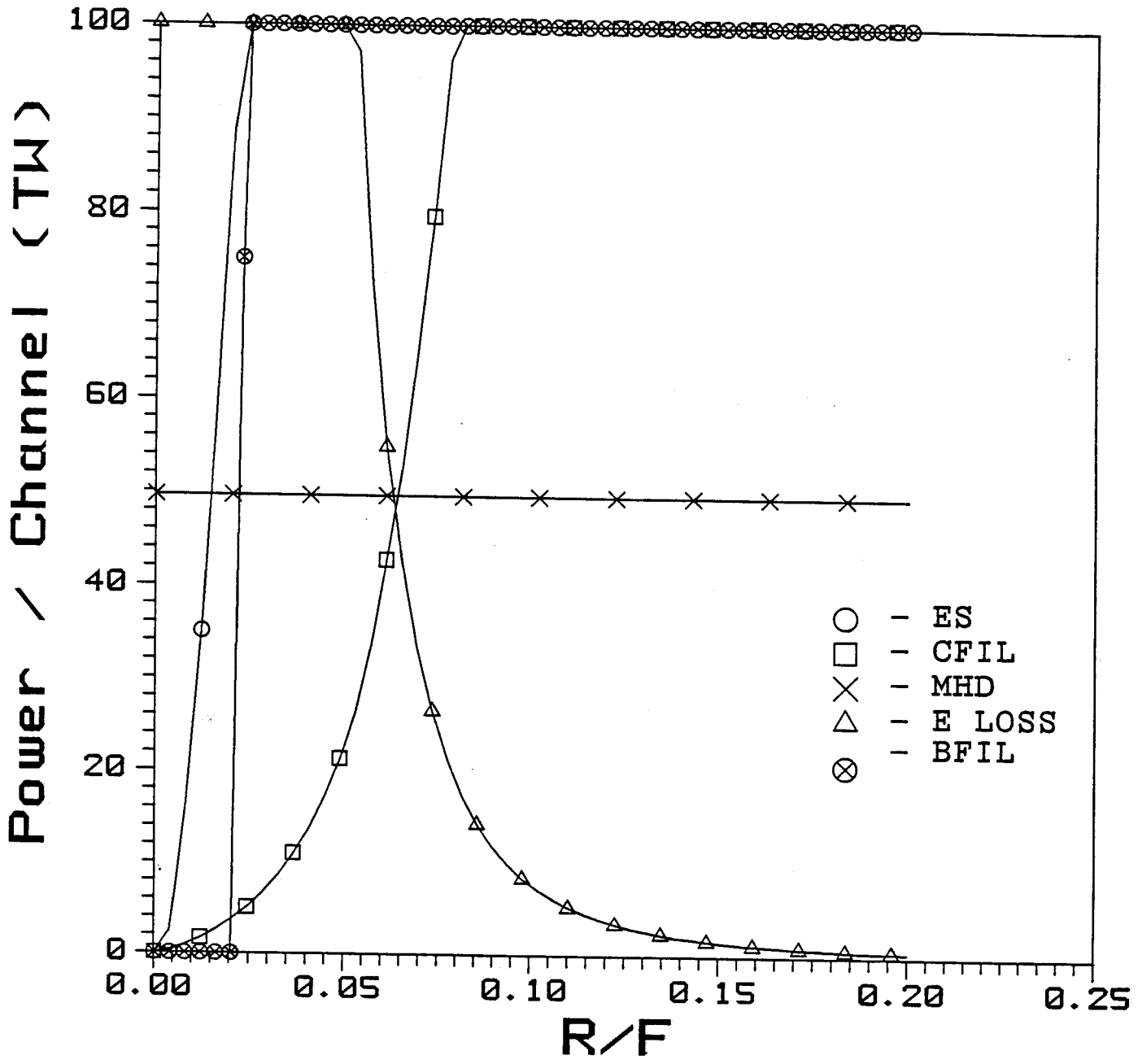

Fig. 4.3. Beam Propagation Window for TDF as Calculated by WINDOW-2.

curves, which occurs in both figures in a region centered roughly around R/F = 0.1. The channel parameters we have assumed for TDF are listed in Table 4.1.

One can see by comparing Figs. 4.2 and 4.3 that the ES, BFIL, and CFIL curves have changed for the improved version of the code (WINDOW-1 and WINDOW-2 use the same formalism for MHD and ELOSS). ES and CFIL are greatly relaxed but BFIL, which demands a minimum value for R/F, has become more severe by moving to larger R/F. The maximum allowable beam power has increased to about 50 TW per channel but the R/F required to reach this power is reduced to 0.06. Recent estimates of the achievable R/F have a minimum value of 0.1, which implies a power per channel of about 10 TW.

The beam ion energy loss constraint is clearly the most troublesome because it is worse at high R/F. Improvements to the formalism for this constraint have not been made. The existing formalism is based partially on computer simulations that were done for deuterium. We must do more simulations of the plasma channels for TDF before we can improve the way WINDOW treats ion energy loss.

4.2 ION Code Improvements

The ION code is a simple program that computes the trajectories of individual ions as they propagate through a plasma channel. This is done by solving the equations of motion for a charged particle in a magnetic field. Assuming azimuthal symmetry, axial uniformity, radially uniform current, and ions with zero angular momentum the equations are given as

Table 4.1. Parameters for WINDOW Calculations

r_b	channel radius	0.5 cm
A_b	beam ion atomic mass	7 amu
Z_b	beam ion charge state	3
τ_b	beam pulse width at channel entrance	30 ns
E	average beam ion energy	30 MeV
α	beam bunching factor	2
L	channel length	300 cm
f_{el}	fractional beam ion energy loss	25%
A_p	channel gas atomic mass	14 amu
σ_p	opacity (Planck) of channel gas	10^3 cm^2/g
T_o	channel gas temperature before ion beam injection	10 eV
Z_p	channel gas charge state	4
X	ratio of mass density to optimum	1

$$\ddot{r} = -\omega_{cb}\dot{z}\, r/r_c$$

$$\ddot{z} = \omega_{cb}\dot{r}\, r/r_c$$

where the cyclotron frequency is

$$\omega_{cb} = \frac{Q_e B_o}{m_i c} .$$

and B_o is the field at the edge of the channel. An approximate solution to these equations can be obtained[3] analytically. If a nonuniform current profile as well as axial nonuniformity are allowed then the equations of motion are

$$\ddot{r} = -\frac{Qe}{m_i c} B_\theta(r,z)\, \dot{z}$$

$$\ddot{z} = \frac{Qe}{m_i c} B_\theta(r,z)\, \dot{r} .$$

These are converted into four first order O.D.E.'s and are easily solved using a standard fifth order predictor-corrector algorithm. In this case of zero angular-momentum, all ions pass through the z-axis and their entrance to the channel can be described by the radial position (r_o), initial speed (V_o) and entrance angle (α_o), as shown in Fig. 4.4.

These calculations have now been further generalized to allow ions with nonzero angular momentum and to allow the magnetic field to have three-dimensional variations. The equations of motion are then

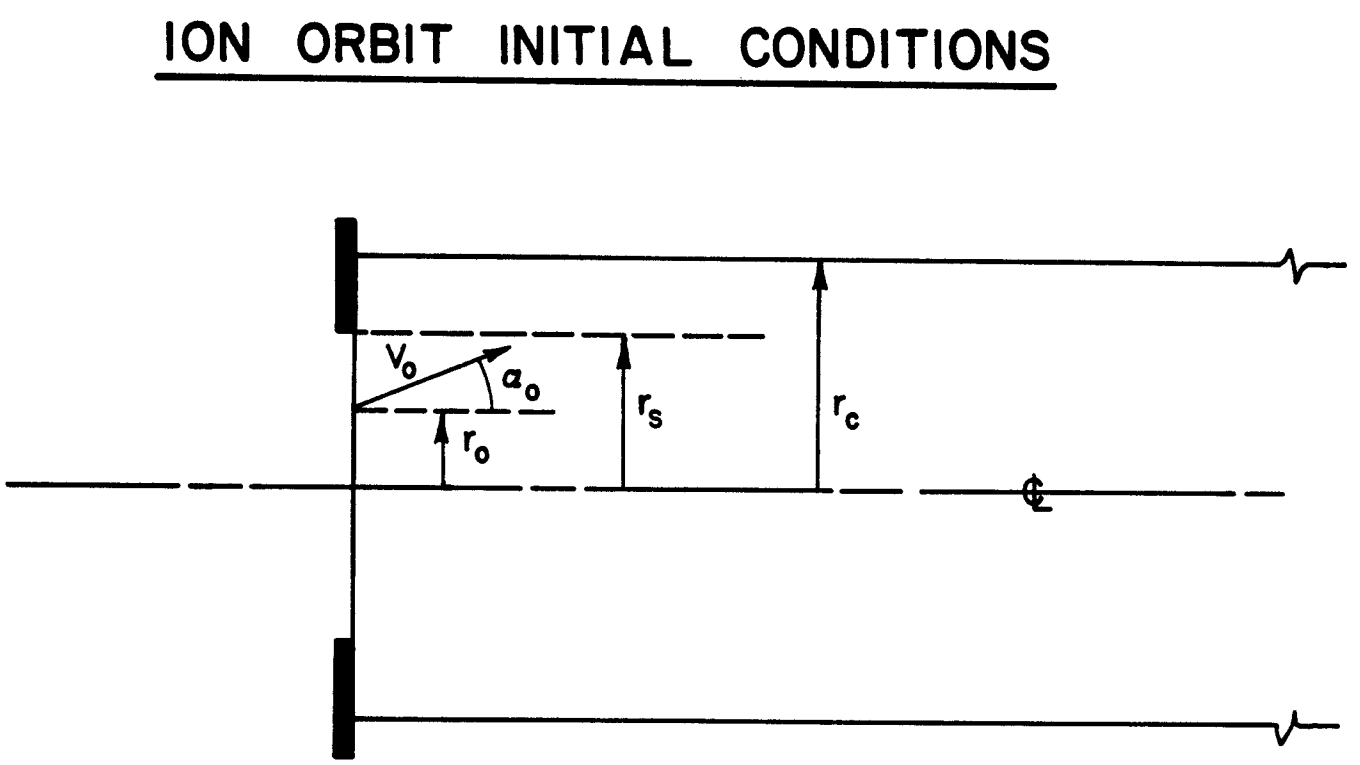

Fig. 4.4. Initial Conditions for Zero Angular Momentum Ions.

$$\ddot{x} = \frac{Qe}{m_i c} (\dot{y}B_z - \dot{z}B_y)$$

$$\ddot{y} = \frac{Qe}{m_i c} (\dot{x}B_z - \dot{z}B_x)$$

$$\ddot{z} = \frac{Qe}{m_i c} (\dot{x}B_y - \dot{y}B_x)$$

with $x(0) = r_o$ $\quad \dot{x}(0) = V_o \sin \alpha_o$

$y(0) = 0$ $\quad \dot{y}(0) = V_o \cos \beta_o$

$z(0) = 0$ $\quad \dot{z}(0) = V_o \cos \alpha_o$.

This is shown schematically in Fig. 4.5. The ions are injected randomly according to the following distributions:

$r_o = f_{r_o}(x/r_s)$ Gaussian distribution

$\alpha_o = f_{\alpha_m}$ Uniform distribution $[-\alpha_m, \alpha_m]$

$\beta_o = f_{\beta_m}$ Uniform distribution $[-\beta_m, \beta_m]$.

These are shown in Fig. 4.6. These equations are posed as six first order O.D.E.'s

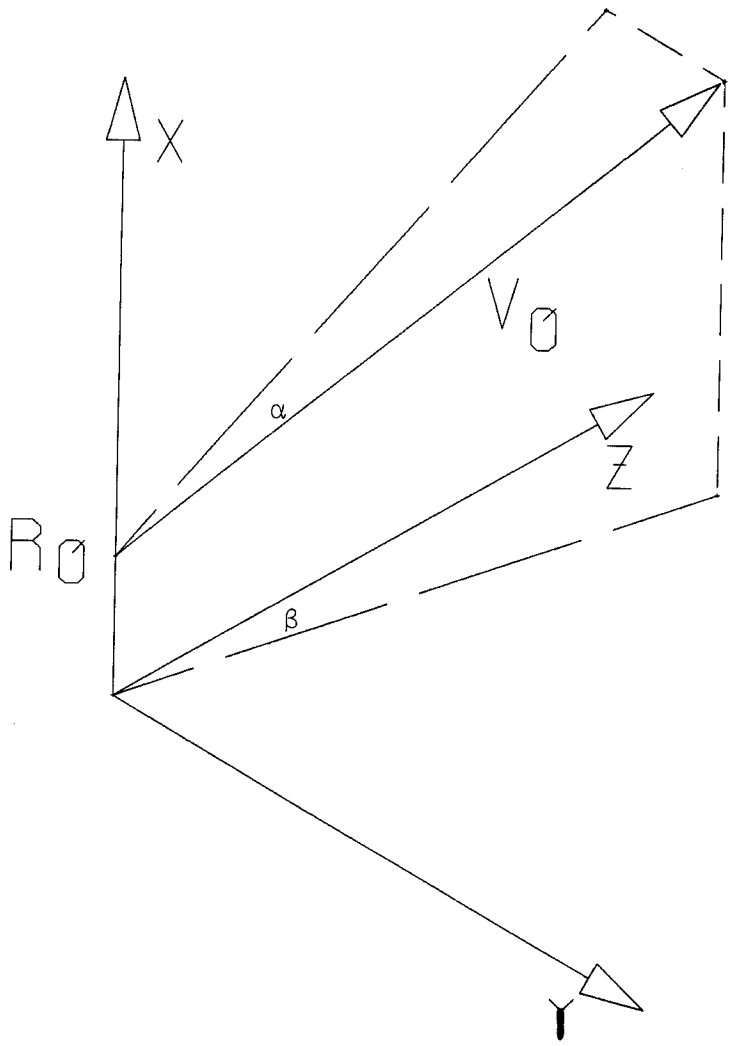

Fig. 4.5. Initial Conditions for Ions with Angular Momentum.

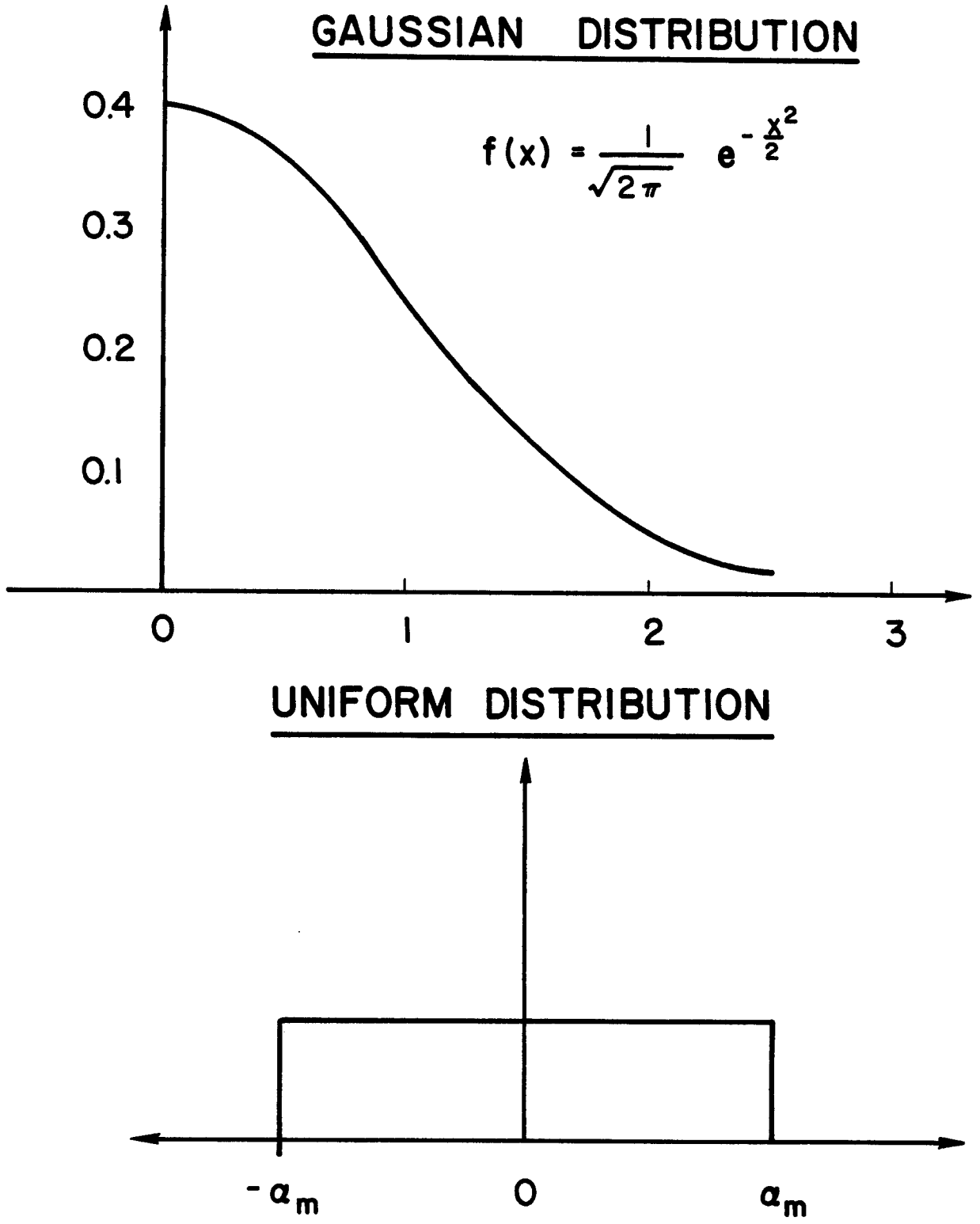

Fig. 4.6. Distribution Functions for Ion Radial and Angular Dependence.

$$\dot{x}_1 = x_2 \qquad \dot{x}_2 = \frac{Qe}{mc}(x_4 B_z - x_6 B_y)$$

$$\dot{x}_3 = x_4 \qquad \dot{x}_4 = \frac{Qe}{mc}(x_2 B_z - x_6 B_x)$$

$$\dot{x}_5 = x_6 \qquad \dot{x}_6 = \frac{Qe}{mc}(x_2 B_y - x_4 B_x)$$

and solved using a standard fifth order predictor-corrector solver. For $\beta_m = 0$ these equations default to the zero angular momentum equations. The subroutine BXYZ can be modified by the user to give arbitrary magnetic fields. For

$$b_\theta(r) = B_o(r/r_c)^n$$

the expressions for B_x and B_y are given below:

$$B_x/B_\theta = \sin\theta \qquad b_x = B_\theta \sin\theta$$

$$B_y/B_\theta = \cos\theta \qquad B_y = B_\theta \cos\theta$$

$$B_x = B_\theta y/r \qquad r = \sqrt{x^2 + y^2}$$

$$B_y = B_\theta x/r \qquad B_\theta = B_o\left(\frac{x^2 + y^2}{x_c^2}\right)^{n/2}$$

hence $$B_x = B_o\left(\frac{x^2 + y^2}{x_c^2}\right)^{n/2} \frac{y}{\sqrt{x^2 + y^2}} = B_o(x^2 + y^2)^{(n-1)/2}\frac{y}{x_c^n}$$

$$B_y = B_o\left(\frac{x^2 + y^2}{x_c^2}\right)^{n/2} \frac{x}{(x^2 + y^2)^{1/2}} = B_o\frac{(x^2 + y^2)^{(n-1)/2}}{x_c^n}x\ .$$

For the case of uniform current (hence linear B_θ) we get

$$B_x = B_o y/x_c \ ,$$

$$B_y = B_o x/x_c \ .$$

This is the default in the program.

4.3 TDF Channel Formation and Ion Propagation Analysis

The current parameters for the TDF diode, drift region and plasma channels are given in Table 4.2. There are eight channels, each carrying a maximum ion power of 31.25 TW. This is achieved by ramping the voltage in the diode and gaining a factor of two in power by time of flight compression of the pulse. The anode geometry is angular as shown in Fig. 4.7 and the anode current density is 1 kA/cm^2. The drift region length is 75 cm and is assumed to be field-free. The channel diameter is nominally 1.0 cm to correspond to the target diameter. The focal spot diameter is presumed to be 0.6 cm leading to a microdivergence half-angle requirement of 4 mrad. This configuration leads to a maximum channel entrance angle of 0.3 rad. With this maximum entrance angle a magnetic field of 185 kG is required to trap a nominal 30 MeV Li^{+3} ion.

Channel formation calculations have been done using the ZPINCH code to determine whether these channel conditions can be created. Table 4.3 gives the parameters for the two runs shown next. Figure 4.8 shows a schematic of the ZPINCH computer model of the channel and external circuit. Figure 4.9 shows the magnetic field profiles at different times for case 1. The current vs. time is plotted in Fig. 4.10. We see from Fig. 4.9 that at a radius of

Table 4.2. Diode-Drift Region-Plasma Channel Parameters

Ion type	lithium
Ion power at the target	500 TW
Time of flight bunching factor	2
Nominal ion energy	30 MeV
Ion energy range	27-33.5 MeV
Number of channels	8
Ion power per channel (entrance)	31.25 TW
(exit)	62.5 TW
Ion electrical current per channel (entrance)	3.12 MA
(exit)	6.24 MA
Ion pulse width (entrance)	30 ns
(exit)	15 ns
Diode type	applied B
Anode geometry	annular
Anode area	1000 cm^2
Inner radius	14 cm
Outer radius	23 cm
Anode current density	1 kA/cm^2
Drift region length	75 cm
Channel length	300 cm
Channel diameter	1.0 cm
Focal spot diameter	0.6 cm
Maximum entrance angle	0.3 rad
Microdivergence half angle	4.0 mrad
Necessary confining magnetic field (E_i = 30 MeV)	185 kG @ r = 0.5 cm
Necessary channel current	464 kA
Best estimate magnetic field	27 kG @ r = 0.5 cm
Channel current	67 kA

Table 4.3. Channel and External Circuit Parameters for ZPINCH Calculations

	Case 1	Case 2
Gas type	nitrogen	nitrogen
Gas pressure	14 torr	14 torr
Full width half max. of initial temperature profile created by laser	0.86 cm	0.86 cm
Maximum initial temperature	0.78 eV	0.78 eV
Channel length	3 m	3 m
Energy in external circuit	481 kJ	481 kJ
External capacitance	0.54 μF	0.54 μF
External inductance	0.5 μH	0.5 μH
External resistance	7 ohm	1 ohm
Number of spatial zones	50	50

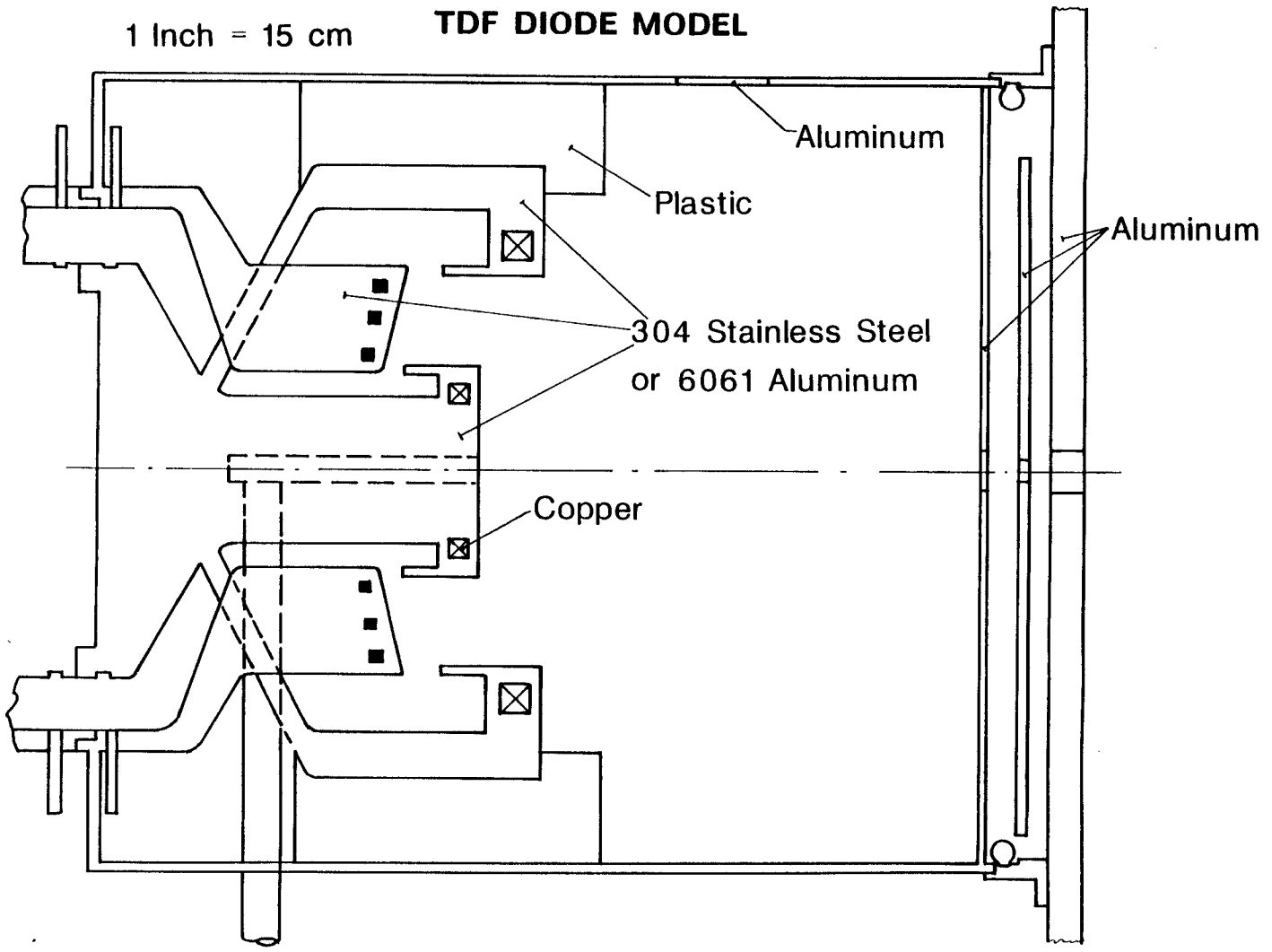

Fig. 4.7. Ion Diode Geometry.

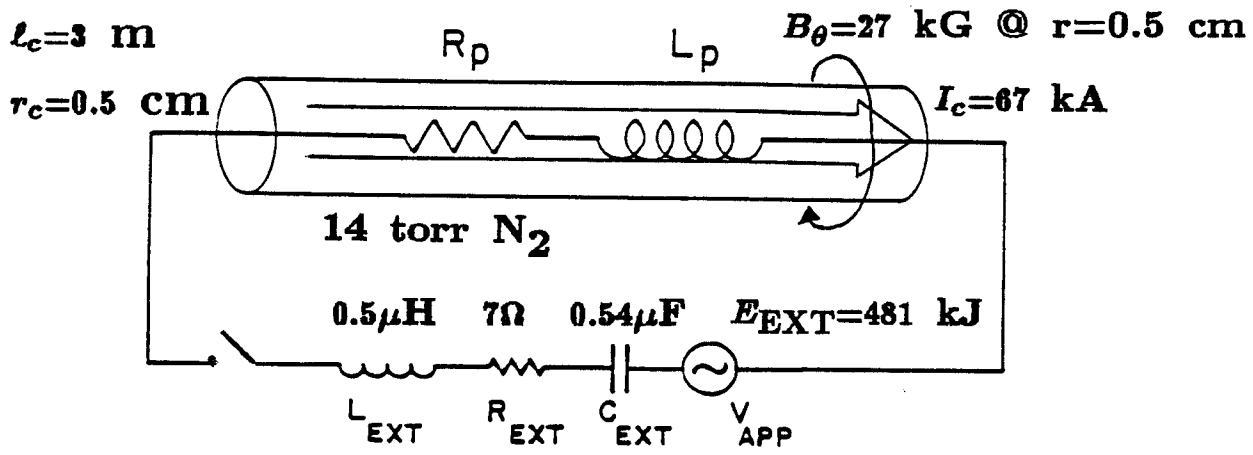

Fig. 4.8. Schematic of ZPINCH Channel and Circuit Model.

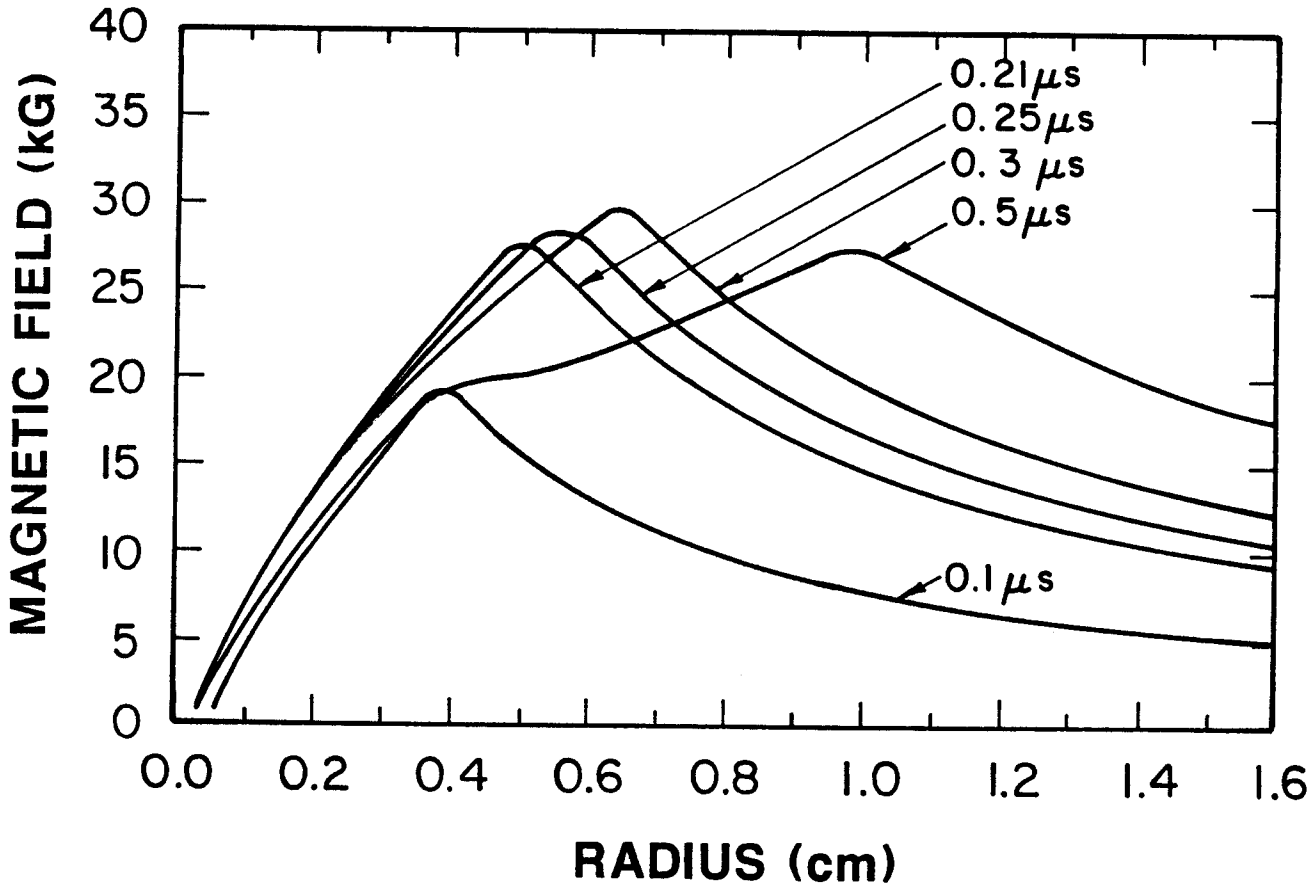

Fig. 4.9. Magnetic Field Profiles (case 1).

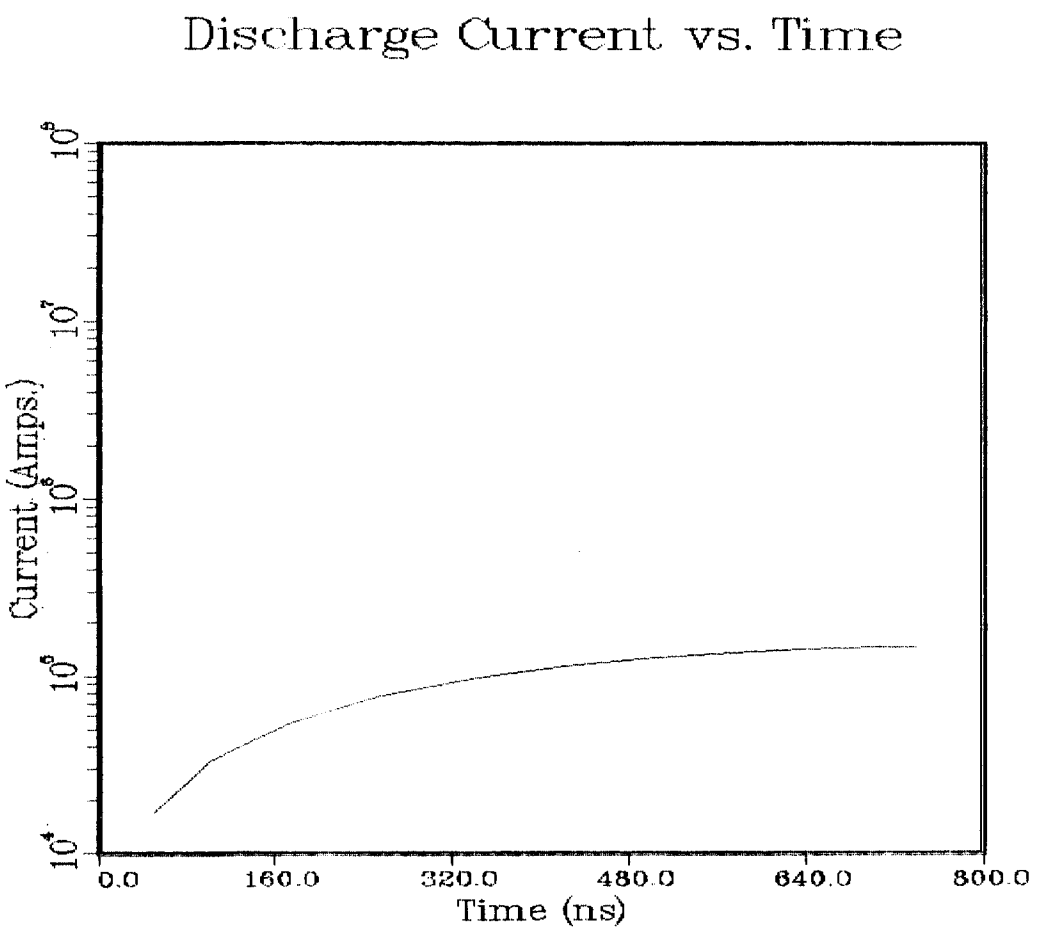

Fig. 4.10. Current vs. Time (case 1).

0.5 cm the magnetic field peaks at about 0.21 μs. The peak magnetic field is drifting outward due to channel heating and radiative transfer that spreads the temperature profile. This is plotted in Fig. 4.11. If the external resistance is reduced to 1 ohm then more current can flow through the channel, Fig. 4.12, yet the magnetic field profiles are essentially the same, Fig. 4.13. We believe that this is due to the radial radiative heat transfer. Thus, based upon these results, we predict that a 185 kG magnetic field will be very difficult to achieve in a nitrogen plasma channel. This situation may be corrected in several ways. These are discussed next.

The radial radiative heat transfer modeling in ZPINCH is clearly responsible for the aforementioned conclusions. The radiative transfer model that is used is multifrequency, flux limited diffusion. We are implementing a multifrequency discrete ordinates (S_N) photon transport model in ZPINCH to improve the radiative heat transfer description. The discrete ordinates method solves the photon transport equation from which the diffusion equation is derived via an angular moments expansion. Comparing this with the diffusion treatment will allow us to test the credibility of these results. As part of other code verification work we are also comparing the nitrogen opacities computed by MIXERG with opacities from the SESAME library. Again, such comparisons will help to determine the credibility of our conclusions.

Should radial radiative diffusion be a problem we could investigate the use of a low-Z gas such as hydrogen or helium. These gases will not be such strong radiators and may allow larger magnetic fields at r = 0.5 cm. One further possibility is a redesigned diode to reduce the maximum entrance angle to ~ 0.1 radians. At this value the necessary confining magnetic field is ~ 30 kG, a value achieved in our computer simulations.

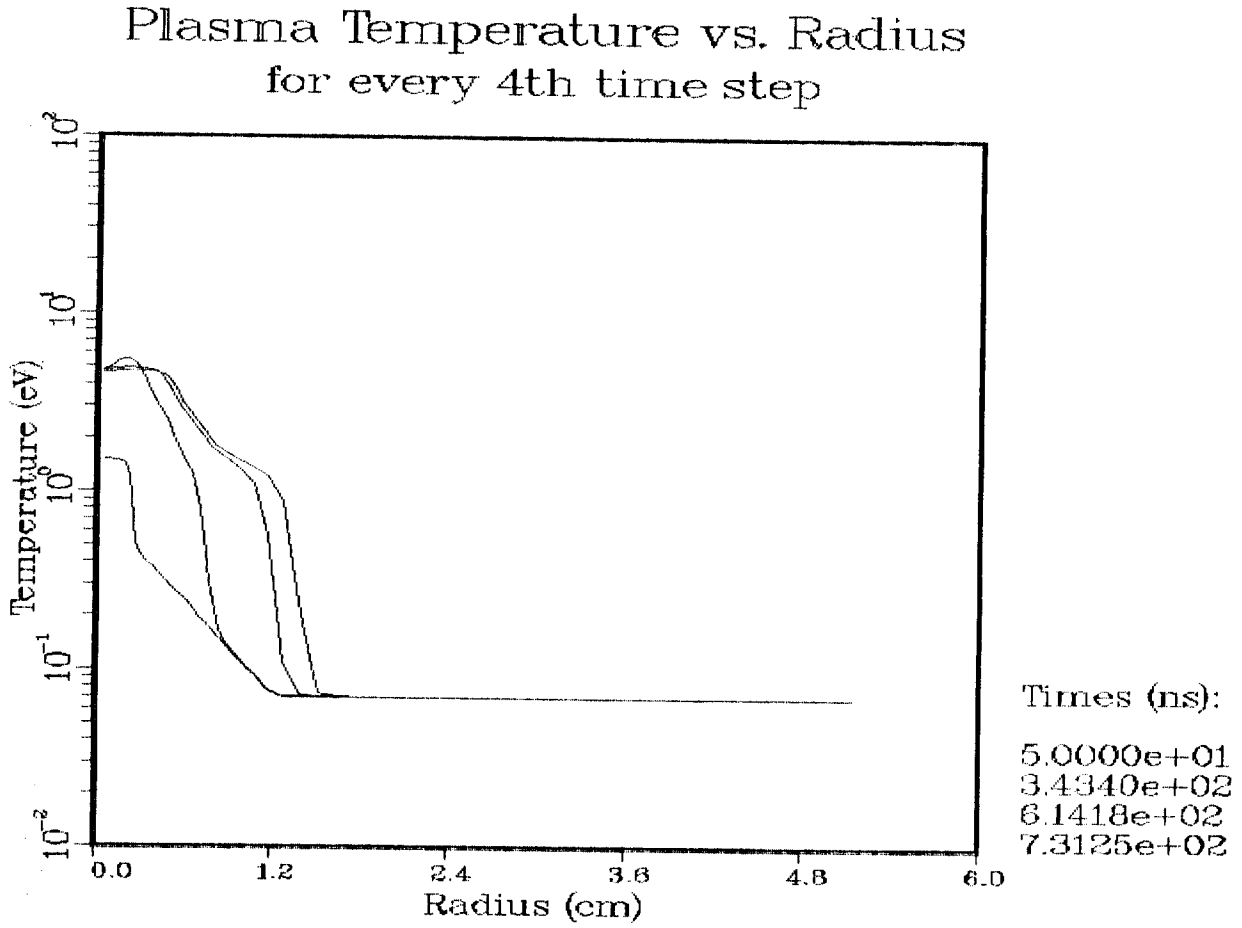

Fig. 4.11. Temperature Profiles (case 1).

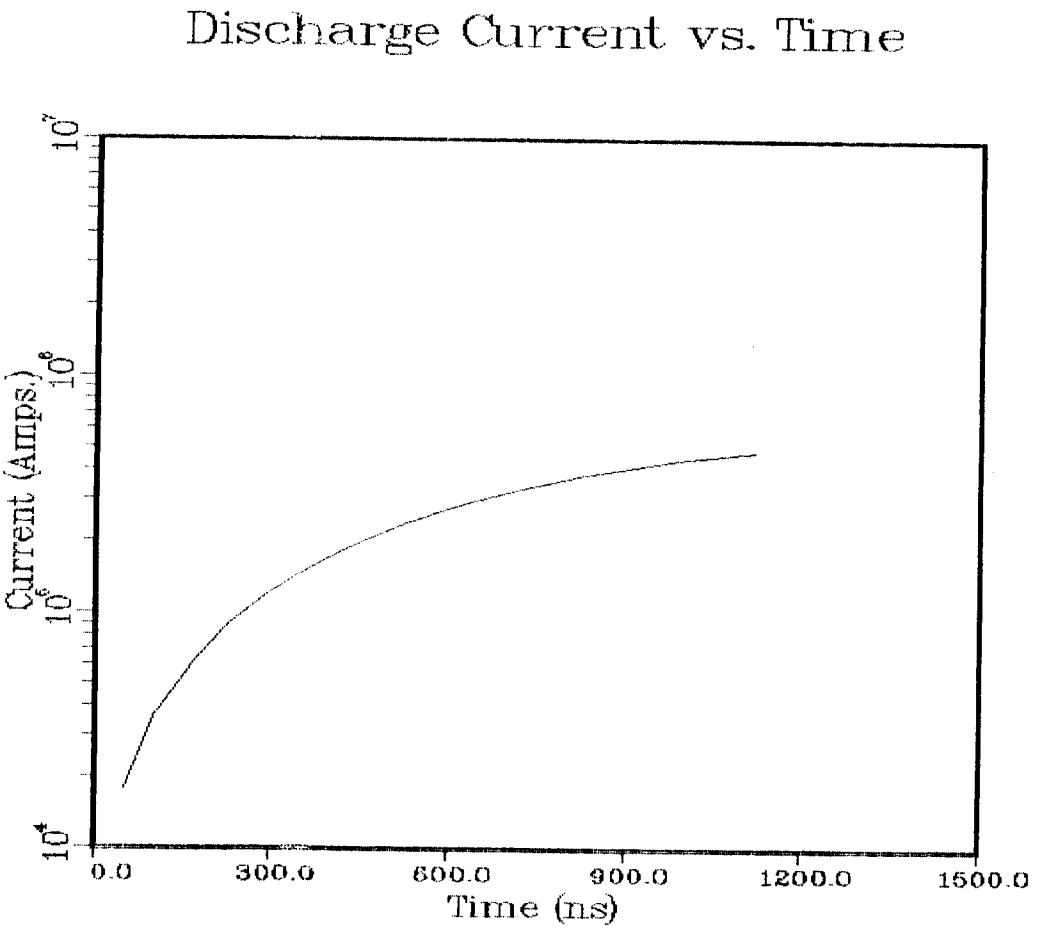

Fig. 4.12. Current vs. Time (case 2).

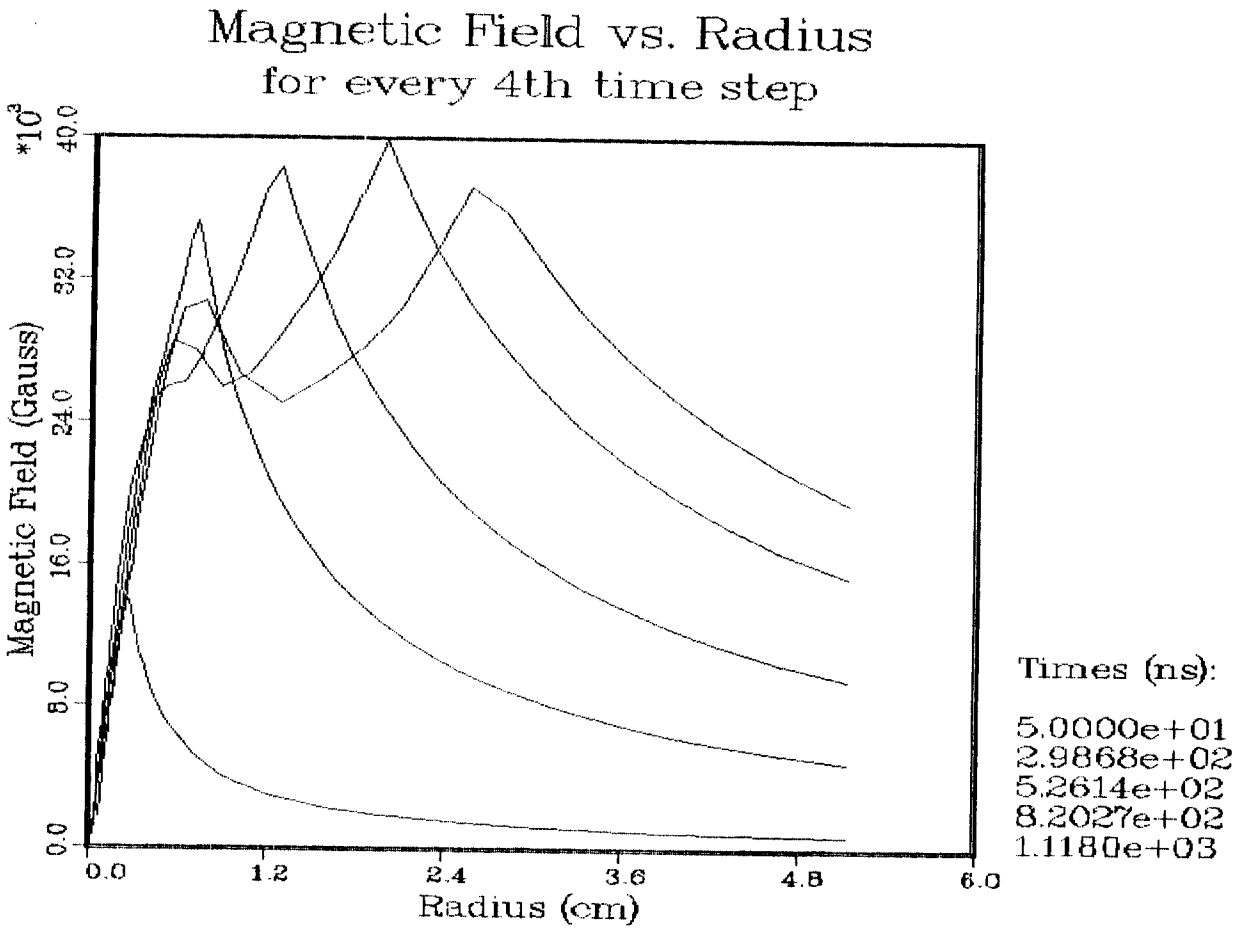

Fig. 4.13. Magnetic Field Profiles (case 2).

Using the best ZPINCH results to date as the initial channel configuration we have done ION particle trajectory simulations to determine the transport efficiency. These results are summarized in Table 4.4 and Fig. 4.14. The channel was assumed to be 1.0 cm in diameter with a linear magnetic field profile at the head of the beam and a $(r/r_c)^5$ profile at the tail of the beam and a maximum value of 30 kG at r_c = 0.5 cm. Ions were stochastically injected into the channel with a Gaussian radial profile with a full width at half maximum of 0.6 cm. The angular divergence was $\pm$0.3 radian (the microdivergence was ignored). The transport efficiency at the head of the beam was 78% and at the tail of the beam was 65%. In this model, once an ion is trapped in the channel it remains trapped. Hence we are getting a 67% trapping efficiency for this mismatch between maximum entrance angle and peak channel magnetic field. This value should approach 100% for properly matched conditions.

References for Chapter 4

1. R.R. Peterson, "WINDOW - A Code to Compute Ion Beam Power Constraints," Fusion Power Associates Report FPA-84-6 (1984).

2. P.F. Ottinger, S.A. Goldstein and D. Mosher, "Constraints on Transportable Ion Beam Power," Naval Research Laboratory Memorandum Report 4948 (1982).

3. P. Ottinger, D. Mosher and S. Goldstein, "Propagation of Intense Ion Beams in Straight and Tapered Z-Discharge Plasma Channels," Phys. Fluids 23, 909 (1980).

Table 4.4. ION Particle Trajectory Calculations

	Head	Tail
Ion type	Li	Li
Ion charge	+3	+3
Ion mass	7	7
Ion energy	27 MeV	33.48 MeV
Channel radius	0.5 cm	0.5 cm
Channel length	300 cm	300 cm
Channel current	30 kA	30 kA
Number of ions in source	5000	5000
Focal spot radius	0.3 cm	0.3 cm
Max. divergence angle (in plane)	0.3 rad	0.3 rad
(out of plane)	0.	0.
Fraction of ions propagated	0.67	0.65

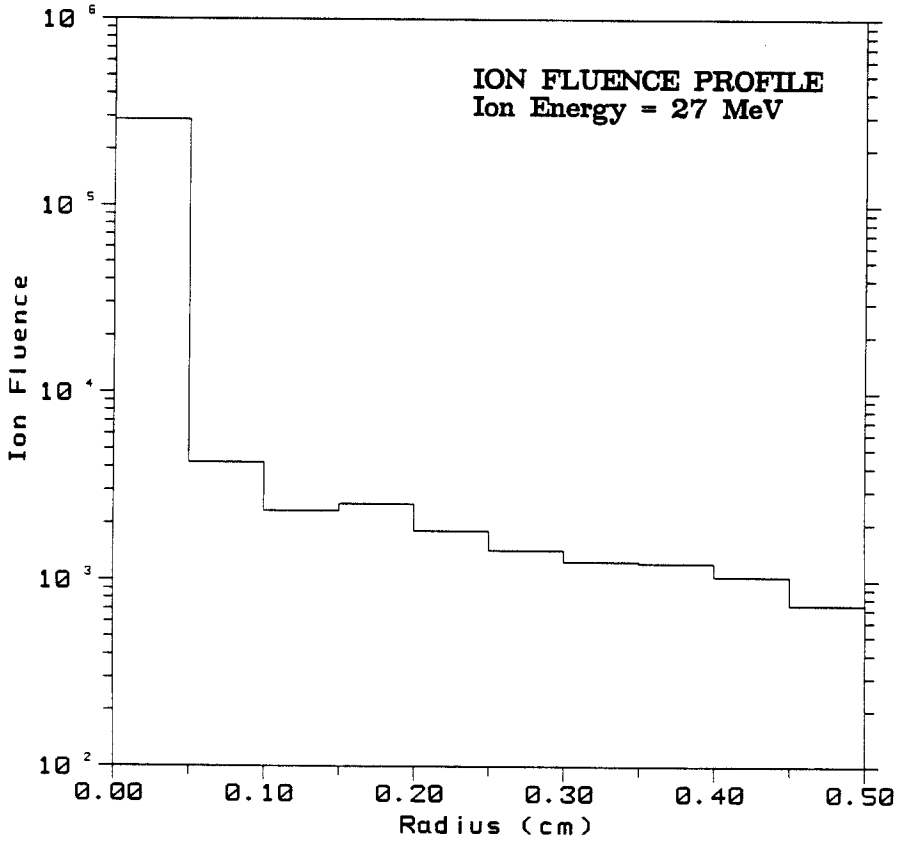

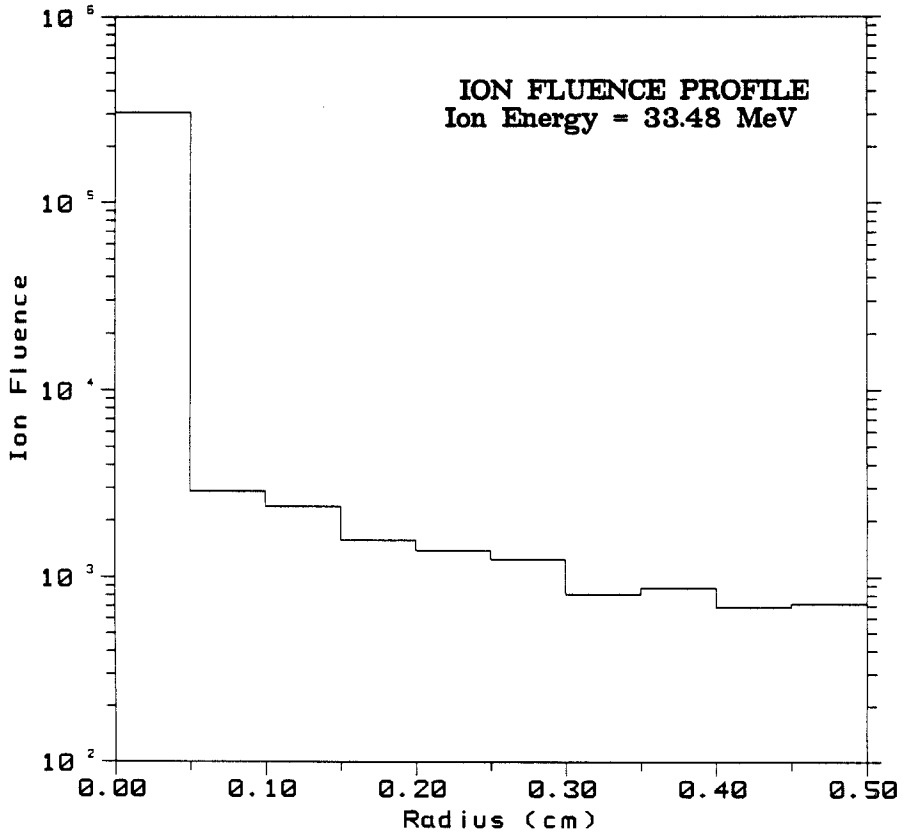

Fig. 4.14. Ion Fluence Profiles at the Target.

5. TARGET DEVELOPMENT FACILITY DESIGN OPTIONS

During the past year we have continued the design of the cylindrical TDF target chamber with a radius of 3 meters. We have also begun the design of a smaller, spherical chamber with a radius of 1 meter. These are pictured in Figs. 5.1 and 5.2. The baseline 3 meter design incorporates a 0.5 meter thick graphite neutron moderator within the target chamber. This softens the neutron flux to the extent that hands on maintenance at the first wall is allowable at 1 week following the last shot. The smaller chamber does not include a neutron moderator and consequently becomes quite activated. In this case, we presume that the chamber will be periodically removed and replaced. A parameter list for the large and small chambers is given in Table 5.1. The ion diode and drift region for both cases is shown in Fig. 5.3.

The heat flux and overpressure at the first surface in both designs is given in Fig. 5.4. The mechanical response of both designs is given in Fig. 5.5. The dose rate behind the first wall following shutdown for both designs is given in Fig. 5.6.

The tradeoffs between the two designs are currently seen as the following:

(1) The "3-meter" design is permanent while the "1-meter" design is often replaced. Each of these has advantages with regard to maintenance. In the 3-meter case we try to control activation while in the 1-meter case we simply remove the highly activated chamber.

(2) The diodes remain in the same position (~ 4 meters from the target) in both cases because this plasma channel length is required for beam bunching. Activation of the diodes is a serious concern and calculations have been done for the geometry of the "3-meter" design where the diodes are

Table 5.1. Parameters for TDF Conceptual Design

General			
Timeframe for operation			1990's
Target yield range			50-800 MJ
Nominal target yield			200 MJ
Number of nominal shots			15,000
Facility lifetime			5 years
Shot rate			10/day
Energy on target			7-8 MJ
Power on target			> 500 TW
Number of ion beams			8
Ion type			Li^{+1}
Ion energy			30 MeV
Target			
Target yield range			50-800 MJ
Nominal yield			200 MJ
UW model target materials			
DT			1 mg
Low-Z (BeO or CH_2)			16 mg
High-Z (Au or W)			72 mg
Model target yield			100 MJ
Neutrons			72 MJ
X-rays			22 MJ
Ions			6 MJ
Model target activation		($Au-CH_2$)	(W-BeO)
Time following shot	0	700 curies	> 10,000
	1 minute	2	160
	1 hour	2	0.1
	1 day	1.5	0.08
	1 week	0.6	0.05
	1 month	0.05	0.04
	1 year	~ 0	0.005

Parameter List for TDF Conceptual Design (10/2/86)

	1 m Chamber	3 m Chamber
Chamber gas	nitrogen	nitrogen
Gas pressure	14 torr	14 torr
Max. blast wave overpressure	13 MPa	0.85 MPa @ 2.5 m
Heat loading	330 J/cm^2	22 J/cm^2 @ 2.5 m
Time of arrival of shock	0.036 ms	0.32 ms @ 2.5 m
Chamber material	welded Al 6061-T6	welded Al 6061-T6
Chamber shape	spherical	cylindrical
Chamber radius	1 m	3 m
Wall thickness	5 cm	5 cm
Chamber mass		
Fundamental frequency (period)	1400 Hz (0.71 ms)	510 Hz (2.0 ms)
Max. stress	12 MPa	15 MPa
Max. strain range (x2)	3.2×10^{-4}	7.8×10^{-4}
Endurance limit	8.3×10^{-4}	8.3×10^{-4}
Lifetime	15,000	15,000
Heat shield material	graphite	graphite
Heat shield thickness	1 cm	1 cm
Heat shield mass		
Neutron moderator material	none	graphite
Moderator thickness	---	0.5 m
Moderator mass		
Activity of target @ 1 wk after shot for Au (W)	0.5 Ci (0.04)	0.5 Ci (0.04)
Dose behind bare Al wall @ 1 week	15,000 mr/hr	1500 mr/hr
Dose behind protected Al wall @ 1 week	---	13 mr/hr
Dose at vacuum casing of SS diode @ 1 week		~ 100 mr/hr
Dose at vacuum casing of Al diode @ 1 week		~ 10 mr/hr
Shield material	borated water	borated water
Shield thickness	5 m	3 m

Diode-Drift Region-Plasma Channel

Ion type	Li^{+1}
Ion power at the target	500 TW
Time of flight bunching factor	2
Nominal ion energy	30 MeV
Ion energy range	27-33.5 MeV
Number of channels	8
Ion power per channel (entrance)	31.25 TW
(exit)	62.5 TW
Ion electrical current per channel (entrance)	3.12 MA
(exit)	6.24 MA
Ion pulse width (entrance)	30 ns
(exit)	15 ns
Diode type	applied B
Anode geometry	annular
Anode area	1000 cm^2
Inner radius	14 cm
Outer radius	23 cm
Anode current density	1 kA/cm^2
Drift region length	75 cm
Channel length	300 cm
Channel diameter	1.0 cm
Focal spot diameter	0.6 cm
Maximum entrance angle	0.3 rad
Microdivergence half angle	4.0 mrad
Necessary confining magnetic field (E_i = 30 MeV)	185 kG @ r = 0.5 cm
Necessary channel current	464 kA
Best estimate magnetic field	27 kG @ r = 0.5 cm
Channel current	67 kA

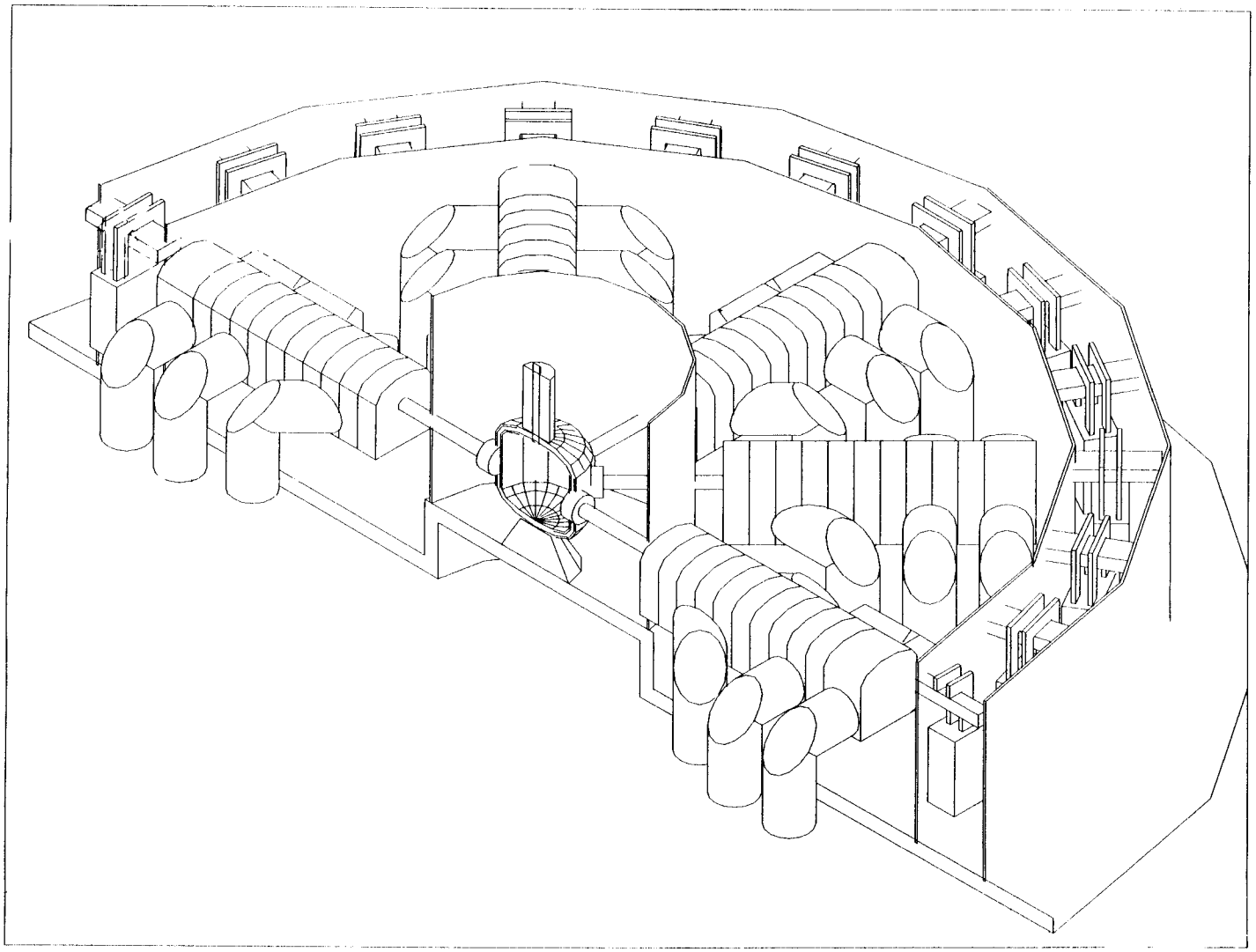

Fig. 5.1. Cylindrical TDF chamber with 3 m radius.

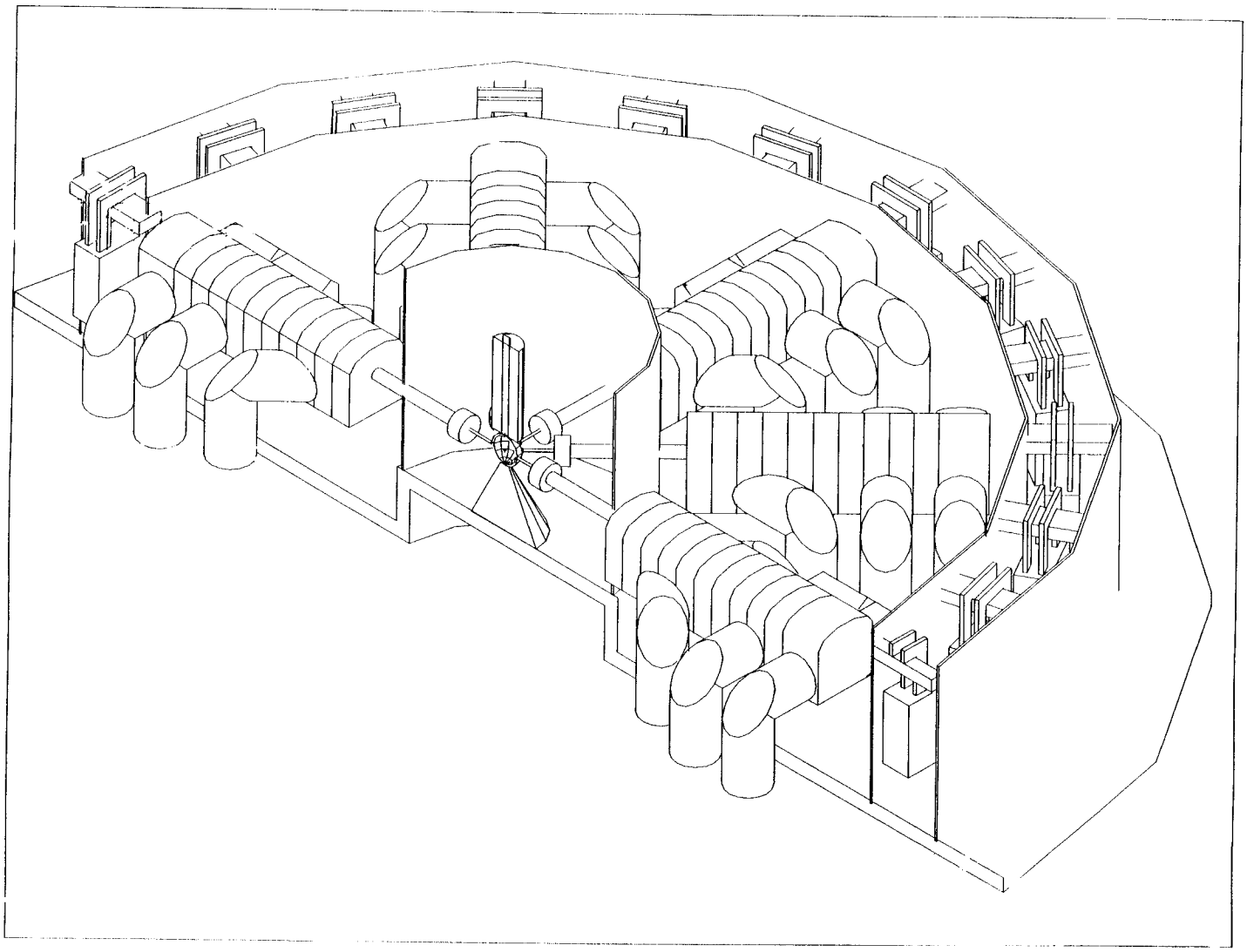

Fig. 5.2. Spherical TDF chamber with 1 m radius.

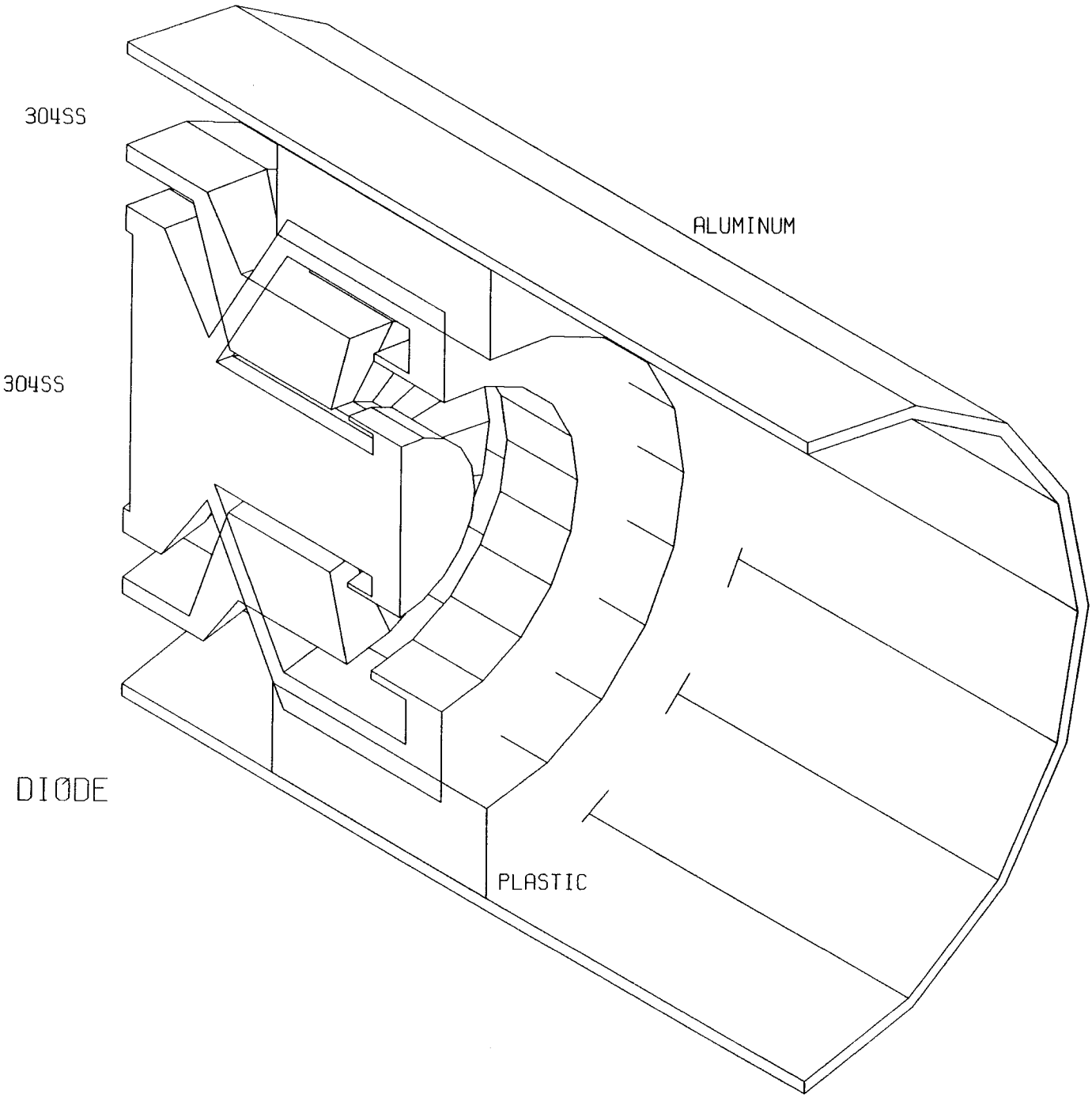

Fig. 5.3. Ion diode and drift region.

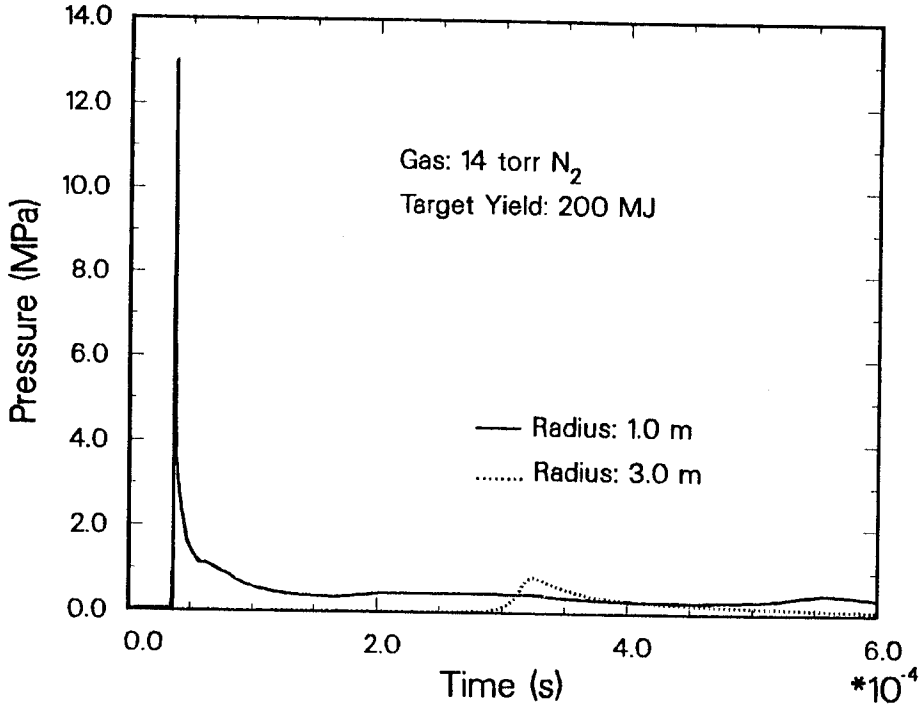

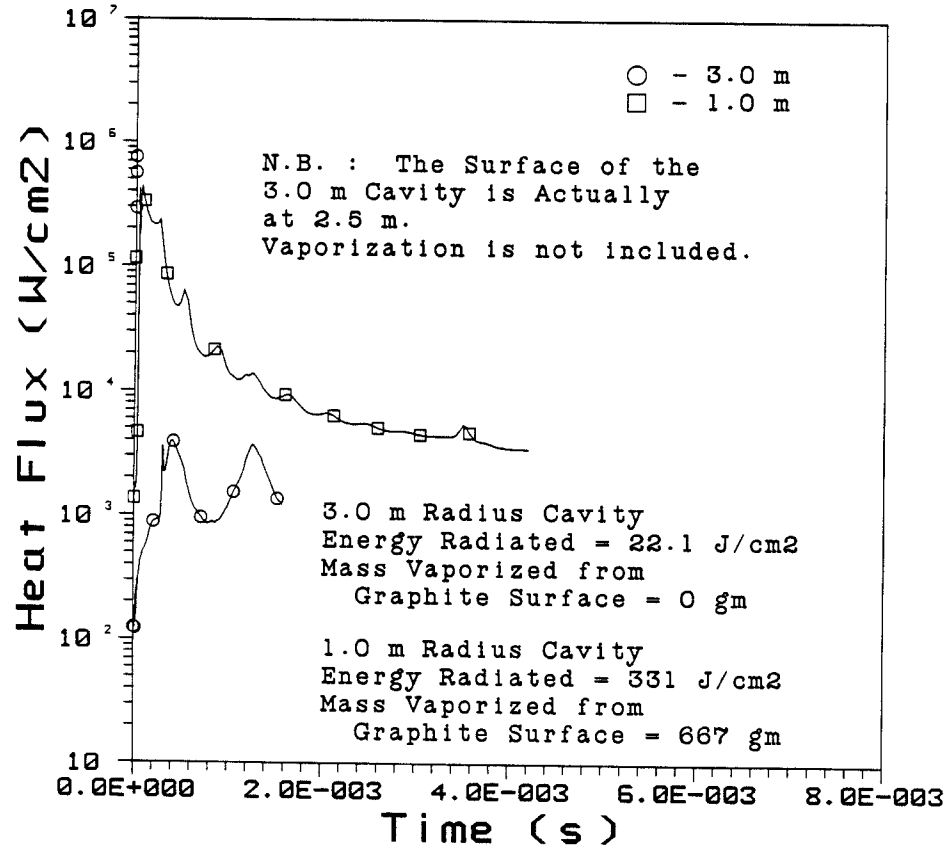

Fig. 5.4. Heat flux and overpressure at the first surface.

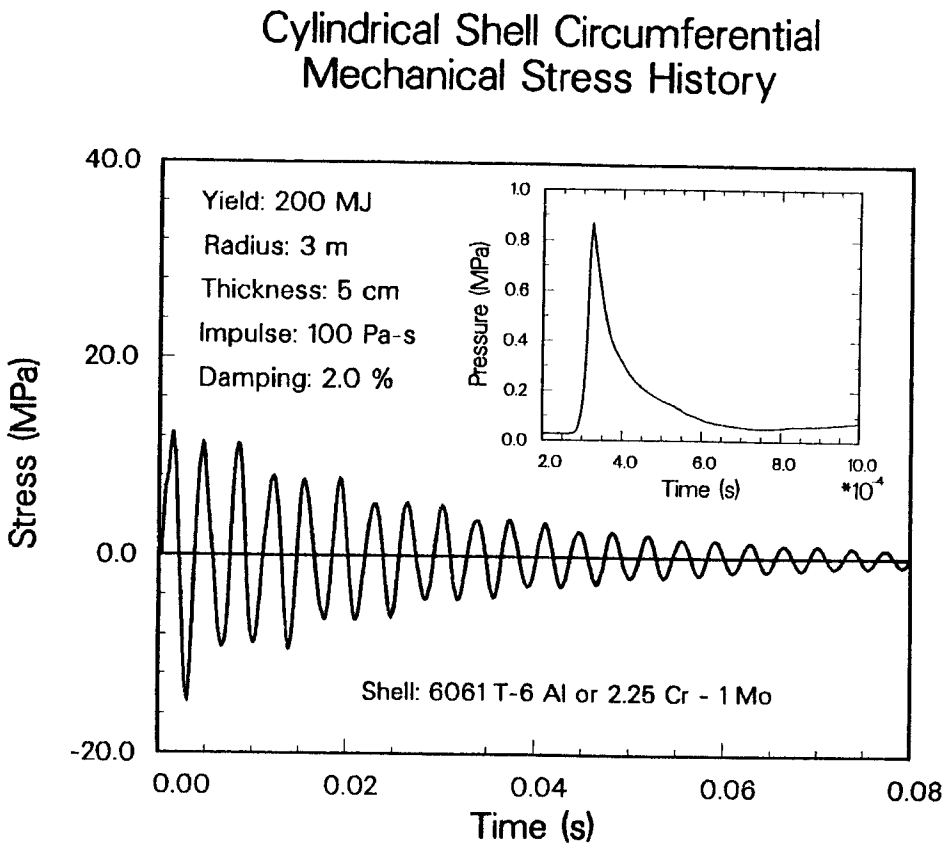

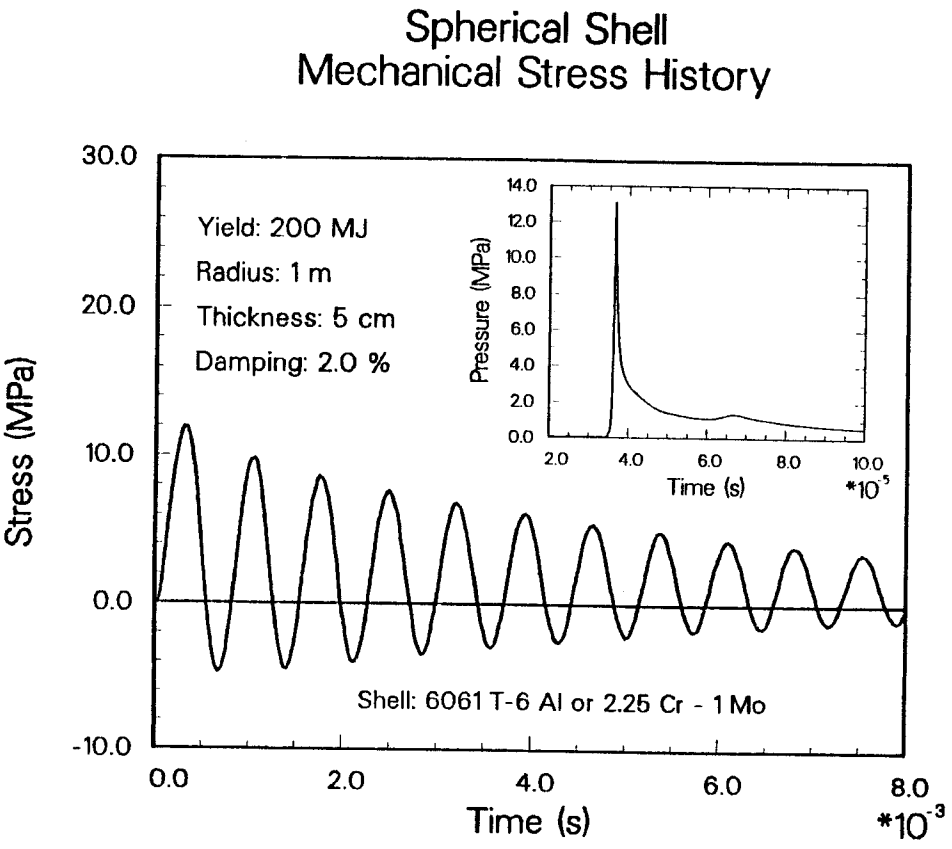

Fig. 5.5. Design curves for fatigue life.

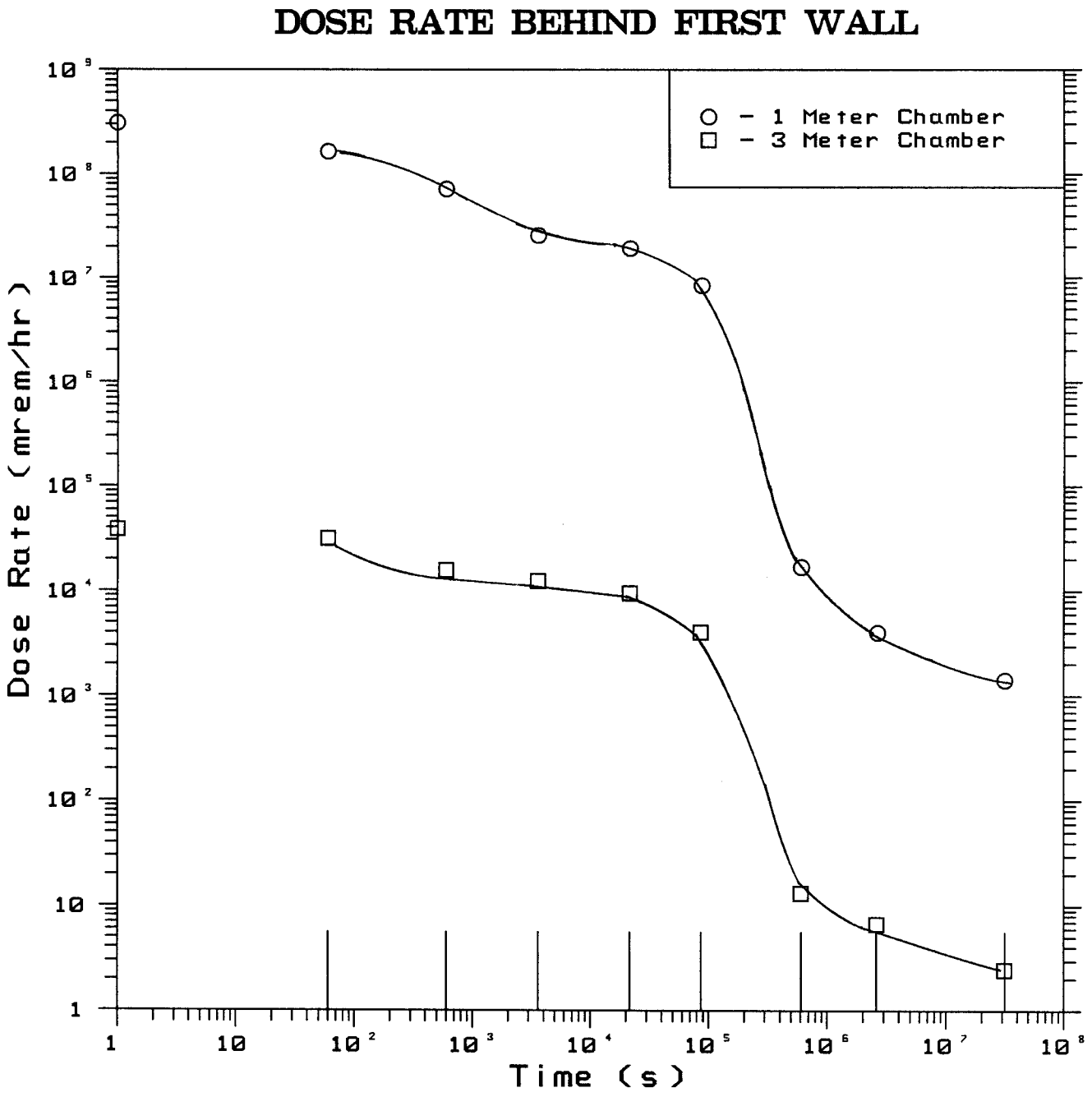

Fig. 5.6. Dose rate behind the first wall.

immediately behind the first wall. The activation appears to be tolerable. However, many neutrons enter the diode region after penetrating the graphite moderator. This is because the graphite moderator thickness is chosen to soften the neutron spectrum but not to totally thermalize the neutrons. In the "1-meter" design the diodes are 2 meters behind the first wall. A high efficiency neutron shield could be placed in this region to significantly reduce the neutron flux in the diode region. The calculations have not yet been done to substantiate this.

(3) The plasma channels in the two cases are 4 meters long. In the "3-meter" design the "free standing" channel length is at least 2.5 meters while in the "1-meter" design it is 1 meter. Depending on the radius of the beam tube between the diode and first surface in each design the remainder of the channel could be either free standing or wall confined. The advantages and disadvantages of these two configurations have not yet been investigated.

(4) The diode and drift regions in both cases are currently inconsistent with plasma channel parameters. The maximum entrance angle to the channel is 0.3 radians while the channel current and consequent B-field can only support an entrance angle of 0.1 radians. This inconsistency results in a computed ion trapping efficiency of $\sim$ 65%. This should be improved to nearly 100%.

(5) Plasma channel formation calculations indicate that there is a minimum B-field limit in nitrogen gas due to the radiatively driven expansion of the current carrying channel. The maximum field is 30 kG. Were this true, then a lower mass gas such as helium or hydrogen might be preferable. The radiative transport modeling in the ZPINCH code should first be validated before this design change is made.

(6) Ion power limit calculations indicate that the power per channel exceeds the limit by about a factor of three, 31.25 TW as compared to 10 TW for a maximum entrance angle of 0.1 radians. This requires either more channels and/or larger channel diameters. The larger diameter would then require some form of final focusing at the target.

ACKNOWLEDGMENT

This work was supported by Sandia National Laboratory under contract number 32-9915. Computer time was supported by the National Science Foundation through the San Diego Supercomputer Center.